

Andreas Niemeyer

On Cloaking for Diffuse Light and its Limits

2021
Dissertation

ON CLOAKING FOR DIFFUSE LIGHT AND ITS LIMITS

Zur Erlangung des akademischen Grades eines
DOKTORS DER NATURWISSENSCHAFTEN
von der KIT-Fakultät für Physik des
Karlsruher Instituts für Technologie (KIT)

genehmigte

DISSERTATION

von

M.Sc. Andreas Falko Niemeyer
geboren in Horb am Neckar

Tag der mündlichen Prüfung: 12.02.2021
Referent: Prof. Dr. Martin Wegener
Korreferent: Prof. Dr. Carsten Rockstuhl

CONTENTS

PUBLICATIONS	1
1 INTRODUCTION	3
2 FUNDAMENTALS	7
2.1 Light Scattering	7
2.1.1 Ballistic and Diffuse Light Propagation	7
2.1.2 Absorption and Scattering	8
2.1.3 Scattering Coefficient	10
2.1.4 Beer-Lambert-Law	11
2.1.5 Reduced Scattering Mean Free Path Length	11
2.1.6 Radiometric Quantities	12
2.2 Laminates in Diffuse Light	18
2.3 Core-Shell Cloaking	20
2.3.1 Invisibility Cloaking and its Limits	20
2.3.2 Realization of a Core-Shell Cloak	21
2.3.3 Transformation Optics	24
2.4 Monte Carlo Raytracing	27
2.4.1 Working Principle of the Monte Carlo Method	27
2.4.2 Implementation of the Algorithm	28
2.5 Probability Theory	30
2.5.1 Probability Density Functions	30
2.5.2 Estimators	31
2.5.3 Gaussian Distribution	32
2.5.4 Confidence Intervals	32
2.5.5 Lorentz Distribution	33
2.5.6 Measure for Gaussian and Lorentzian Distributions	33
2.6 Laser Speckles	35
2.6.1 Origin of Speckles	35
2.6.2 Speckle Contrast	36

2.7	Measuring Complex Fields	41
3	LIMITS OF LAMINATES IN DIFFUSE-LIGHT	47
3.1	Introduction	48
3.2	Experimental Setup	49
3.3	Monte Carlo Simulations	52
3.4	Simulation Results	53
3.4.1	Measuring the Ellipticity	56
3.4.2	Results for Realistically Manufacturable Laminate Contrast	59
3.4.3	Results for Increased Laminate Contrast	64
3.4.4	Results for Decreased Laminate Contrast	66
3.4.5	Results for Anisotropic Scattering	67
3.4.6	Results for Realistic Refractive Index	68
3.5	Discussion	70
3.6	Conclusion	71
4	SPECKLE ANALYSIS OF DIFFUSE-LIGHT CLOAKS	73
4.1	Experimental Setup and First Results	74
4.1.1	Reference, Obstacle and Cloak Samples	74
4.1.2	First Experiments	75
4.1.3	Improved Setup and Statistical Analysis	77
4.2	Speckle Contrast for Semi-Coherent Light	79
4.2.1	Illumination with Shorter Coherence Lengths	80
4.2.2	Measurements on Multiple Coherence Lengths	82
4.2.3	Theoretical Analysis	83
4.3	Conclusion	86
5	EIGENCHANNEL ANALYSIS	87
5.1	Sample Preparation	88
5.1.1	Sample Characterization and Optimization	91
5.2	Interferometric Setup	93
5.2.1	Sample Illumination	95
5.3	Coherent Analysis	98
5.4	Transmission Matrix and Eigenchannels	100
5.4.1	Singular Value Decomposition	100
5.4.2	Singular Vectors	103
5.4.3	Singular Value Distributions	104
5.5	Conclusion	110

6 CONCLUSIONS AND OUTLOOK 111

BIBLIOGRAPHY 113

ACKNOWLEDGMENTS 121

PUBLICATIONS

PARTS OF THIS THESIS HAVE ALREADY BEEN PUBLISHED ...

... in scientific journals:

- S. Mannherz¹, A. Niemeyer¹, F. Mayer, C. Kern, and M. Wegener, "On the limits of laminates in diffusive optics", *Opt. Express* **26**, 34274-34287 (2018).
- A. Niemeyer, F. Mayer, A. Naber, M. Koirala, A. Yamilov, and M. Wegener, "Uncloaking diffusive-light invisibility cloaks by speckle analysis", *Opt. Lett.* **42**, 1998-2001 (2017).
- R. Schittny¹, A. Niemeyer¹, M. Kadic, T. Bückmann, A. Naber, and M. Wegener, "Transient behavior of invisibility cloaks for diffusive light propagation", *Optica* **2**, 84-87 (2015).
- R. Schittny, A. Niemeyer, F. Mayer, A. Naber, M. Kadic, and M. Wegener, "Invisibility cloaking in light-scattering media", *Laser Photonics Rev.* **10**, 382-408 (2016).
- R. Schittny, A. Niemeyer, M. Kadic, T. Bückmann, A. Naber, and M. Wegener, "Diffuse-light all-solid-state invisibility cloak", *Opt. Lett.* **40**, 4202-4205 (2015).
- F. Mayer, R. Schittny, A. Egel, A. Niemeyer, J. Preinfalk, U. Lemmer, and M. Wegener, "Cloaking Contacts on Large-Area Organic Light-Emitting Diodes", *Adv. Optic. Mater.* **4**, 740-745 (2016).

... at scientific conferences (only own presentations):

- A. Niemeyer, S. Mannherz, F. Mayer, and M. Wegener, "Limits of laminates in diffusive optics", Metamaterials Conference, Espoo, Finland, August 2018.
- A. Niemeyer, F. Mayer, A. Naber, M. Koirala, A. Yamilov, and M. Wegener, "Partial Coherence Uncloaks Diffusive Optical Invisibility Cloaks", Metamaterials Conference, Marseille, France, August 2017.

¹ equally contributing first authors

1 INTRODUCTION

Light is not only a basic necessity for all life on earth but also one's most important tool for getting information about our environment. Our eyesight might be our most important sense and losing it has the most severe implications in everyday life. It is no surprise, that optics is one of the oldest disciplines in physics, driven by the urge to understand our universe on all scales. Light microscopy has allowed us to investigate cells and explore the workings of our body, while telescopes have been used to grasp knowledge about our solar system and beyond. Trusting in what one sees is crucial for decision making and orientation. A prime example are x-ray-based diagnostics that have allowed doctors for more than a century to make non-invasive assessments.

However, detecting something might not always be the main goal. Certain applications require to guide light around objects – in certain fields even hide them. But what would be the implications if one cannot tell the difference between an object and its surrounding? For a long time, invisibility cloaks were only the content of tales and science fiction stories. But with new advances in research, one has to start questioning the trustworthiness of what one sees, as the foundation for modern real life invisibility cloaks is already reality.

A pioneering paper was published in 2006 by J. Pendry et al., in which the authors introduced the concept of what was later termed “transformation optics” [1]. Here, starting from a virtual coordinate transformation, the physical properties of a material are derived. In this fashion, the behavior of a physical system can be purposefully tailored to obtain a desired functionality. As an example, this allows for guiding the propagation of light at will – even around objects, enabling, within certain limits, the realization of real invisibility cloaks.

With this tool at hand, not only the research on cloaking devices for free space optics [2–10] but also research in other fields of physics was triggered. The beauty of transformation optics in general is, that it is not limited in its approach to the field of free-space optics, but can be applied as transformation physics to many other fields with small modifications. Transformation physics has therefore enabled research in many other fields like acoustics [11–13], elastomechanics [14–20], electric conduction [21–23], magnetostatics [24–26], and heat conduction

[27–29].

A particularly impressive kind of invisibility cloak was published in the field of diffuse-light propagation [30]. More importantly, the diffuse-light regime is by no means an academic paper exercise but has real-world applications as can be seen in diffuse optical mammography [31–33].

Although transformation optics enables bending the flow of light to will, all cloaking devices have their limits. Most prominently, broad band free space invisibility cloaks are limited by special relativity: The group velocity of light cannot be accelerated beyond the vacuum speed of light to make up for the detour around a cloaked object [34]. In the diffuse-light regime, however, we are no longer bound by this fundamental limit for free-space propagation, as the effective speed of propagation is significantly slowed down due to multiple scattering in diffusive media.

Furthermore, for most free-space cloaking approaches the transition from a theoretical design to a real-world device is often limited by a very complicated or impossible fabrication of constituent materials.

In the field of diffuse optics, however, much simpler designs can achieve enormous effects. The simple concept of the core-shell cloak published in 2014 by R. Schittny et al. [30] shows precisely this. The authors used the concept of neutral inclusion which has been known long before transformation optics [35–38]. These cloaks are relatively easy to fabricate and work perfectly for homogeneous illumination for all visible wavelengths, all directions, and all polarization.

But even these cloaking designs have their Achilles' heel. During my master's thesis, I performed transient experiments on a core-shell cloak and within this study, we discovered that all diffuse-light cloaks lack proper transient cloaking [39]. While this effect can be exploited in time-domain measurements in diffuse optical mammography for better diagnostics, it poses a fundamental challenge in the field of cloaking.

Besides this limit, there is little known about the limitations of this kind of invisibility cloak. Still an open question is whether it is possible to improve the core-shell cloak by using a more advanced design from transformation optics. The revised cloak would benefit from an improved performance under inhomogeneous illumination. And while the cloak is working fine under white light illumination still no research had been done on the performance of diffuse-light cloaks illuminated by just one wavelength, hence, coherent light.

To change the core-shell cloak to a more advanced design, one would have to use a higher number of laminate layers in order to gain anisotropic material properties typically demanded by transformation optics. Thus, a general study on laminates in diffusive optics has been carried out in this work. Furthermore, the core-shell cloak is not designed for illumination with coherent light, as diffusion theory does not account for any wave phenomena. To investigate the impact of coherent light, experiments on a core-shell cloak with coherent light and partially

coherent light have been realized.

In addition to that, a complex coherent transmission matrix of the cloak is measured in order to obtain more information from the sample imperceptible by other means.

Insights into the behavior of light in scattering media do not only lead to designs of more advanced invisibility cloaks for special purposes as for example for cloaking contact grids on OLEDs [40], but also to a deeper understanding of optics in the unexplored light regime in between ballistic and diffusive light propagation.

Finding possible flaws and general limitations of cloaking helps to not only improve the design of such cloaks but foster also improved diagnostics. For instance, using short light pulses in a time-of-flight measurement to get an insight into human tissue therefore ensures, that nothing can be perfectly hidden from a doctor's diagnosis.

Ultimately, the proof that there is no perfect cloaking device might be good for everyone's good night sleep.

OUTLINE OF THIS THESIS

In the following Chapter 2, an introduction is given into the most important basics necessary to understand the work that has been done in the subsequent chapters. Textbook knowledge is condensed to the scope that is needed, important variables are introduced, and some simulation as well as measurement techniques are presented.

Bending the flow of light in diffusive optics is usually based on one simple idea: The light will always follow the path of minimal "resistance". Laminates are using this idea and are a wonderful tool for many physics applications. But in diffusive light, there are some special limitations on how laminates may be used. These limits are simulated by a Monte Carlo ray-tracing software and discussed in Chapter 3.

To examine the performance of the core-shell cloak under coherent illumination, in Chapter 4, the statistics of the transmission under coherent illumination are investigated by experiments and corresponding simulations as well as theoretical work. With partially coherent light, one exploits a limitation already utilized to reveal the cloak by transient illumination to uncloak the cloak once again.

Going one step further in Chapter 5, extracting information out of the scattering device is realized by recording a complex transmission matrix of the cloak sample in an interferometric experimental setup. By scanning the cloak with multiple illumination angles, a look at the statistical behavior of the transmission eigenchannels is possible.

At the end of this thesis, all findings are summarized and discussed in Chapter 6.

2 FUNDAMENTALS

Within this chapter, theoretical knowledge is refreshed to ease the transition into the following chapters. Additionally, several variables used in those chapters are introduced.

The basis for all projects within this work is a solid knowledge on light scattering in diffuse media and an understanding of invisibility cloaking in this regime, which are given in Sections 2.1 and 2.3. In addition to these general topics, project specific fundamentals as the Monte Carlo method for photon transport (Section 2.4), laminate theory (Section 2.2), coherent light scattering (Section 2.6), and complex field measurement methods (Section 2.7) are outlined as well.

Parts of the projects in this thesis were joint works with my colleagues R. Schittny and S. Mannherz. As we were working together on the theoretical fundamentals, their theses [41, 42] provide similar fundamental chapters on light scattering, core-shell cloaking, and laminates.

2.1 LIGHT SCATTERING

In this thesis light is the most important tool to examine the manufactured samples. Therefore an introduction into light scattering and the boundaries in which diffusive light transport is present, is given. The introduction starts from ray optics, and therefore without any interference effects, as this will be discussed later (see Sections 2.6 and 2.7).

2.1.1 *Ballistic and Diffuse Light Propagation*

Light propagation in a medium with randomly distributed scattering particles can be divided into three regimes, as shown in Figure 2.1. The first one is the so called “ballistic regime”. In this regime, most of the light will propagate through the sample without any interaction with the scattering particles. In everyday life, we see this kind of light transport in air, transparent windows, or clear water.

If the distance between two (isotropic) scattering events is in the length scale of

the wavelength, “localization” might occur [43–45], which is the second regime. In between these two extremes, there is the “diffusive regime”. Most of the transmitted light is scattered several times inside the medium. Everyday examples are dense fog, clouds, a glass of milk, or a piece of paper. In this work, the transition between the diffusive regime and the ballistic regime will be observed by simulations and in experiments.

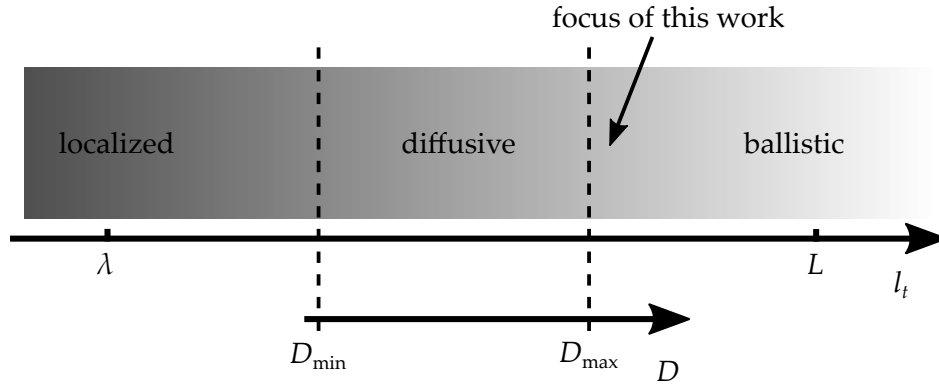


Figure 2.1: Regimes of light propagation. With increasing transport mean free path length l_t , transition from the localized regime, where the transport mean free path length is in the order of the wavelength ($l_t \approx \lambda$), to the ballistic regime, where the transport mean free path length is in the order of the dimensions of the medium ($l_t \approx L$), is shown. In between these two extremes light travels according to the diffusion equation and a diffusivity D can be introduced. The focus of this work lays on the transition between the diffusive and the ballistic regime.

2.1.2 Absorption and Scattering

In the following section, the mathematical and physical fundamentals of light propagation in scattering media are explained briefly as they are necessary to understand the central formula in diffusive light propagation, the diffusion equation for light. However, for a complete introduction, reading the references is inevitable. This section is based on the book "Light propagation through biological tissue and other diffusive media" [46].

Hereafter, a dielectric, transparent medium with refractive index n is given, in which dielectric scattering centers with a different refractive index are embedded randomly. The only two possible interactions between light and this medium are either elastic scattering at the scattering centers or absorption within the background medium. This simple model for light-matter interaction is a very crude simplification that has the advantage to avoid getting into more complex phenomena of light-matter interaction and will lead to relatively simple analytical

solutions.

In this work, absorption and scattering are the main phenomena of light-matter interaction [46]. Light propagation is described as the propagation of single photons in a direction \vec{s} . A scattering event will change the initial direction \vec{s} to a new direction \vec{s}' . The angular dependence of this scattering event is given by the scattering phase function (also called scattering function) $p(\vec{s}, \vec{s}')$. By considering polarized light and spherical particles, the scattering function only depends on the scattering angle θ between \vec{s} and \vec{s}' :

$$p(\vec{s}, \vec{s}') = p(\theta). \quad (2.1)$$

As everything is rotational symmetric around the propagation direction of light, the scattering function is independent of the azimuthal angle ϕ . Thus ϕ is uniformly distributed and the probability function f_ϕ , is given by

$$f_\phi = \frac{1}{2\pi}. \quad (2.2)$$

Its normalization becomes

$$\int_0^{2\pi} f_\phi d\phi = 1. \quad (2.3)$$

The same holds true for the normalization f_θ

$$\int_0^\pi f_\theta d\theta = 1, \quad (2.4)$$

resulting in the probability function

$$f_\theta = 2\pi p(\theta) \sin(\theta), \quad (2.5)$$

where $p(\theta)$ is given by the Henyey-Greenstein phase function [47]

$$p(\theta) = \frac{1}{4\pi} \frac{1 - g^2}{(1 + g^2 - 2g \cos \theta)^{3/2}}. \quad (2.6)$$

This equation can be deduced from Mie theory [48]. Here, $g = \langle \cos \theta \rangle$ is the scattering asymmetry factor.

As the number of photons will stay the same and all photons will scatter in arbitrary directions, the scattering function can be normalized by integrating over the solid angle $d\Omega$:

$$\int_{4\pi} p(\theta) d\Omega = 2\pi \int_0^\pi p(\theta) \sin \theta d\theta = 1. \quad (2.7)$$

For multiple scattering processes, calculating the exact scattering phase function is not necessary. Calculating one parameter, the asymmetry factor (or anisotropy factor) g , is sufficient [49]:

$$g = \langle \cos \theta \rangle = 2\pi \int_0^\pi \cos \theta p(\theta) \sin \theta d\theta. \quad (2.8)$$

This asymmetry factor is an easy measure for the kind of scattering event that is happening inside of the medium. Its value reaches from -1 to 1 and is mainly dependent on the ratio between wavelength λ and the diameter of the scattering particle d . A material with $g = -1$ has only scattering events where the direction of light is redirected by 180° , also called backscattering. If the material is dominated by Rayleigh scattering, the average angle is $\theta = \pi/2$, which corresponds to isotropic scattering [50]. Rayleigh scattering is prominent when the diameter of the scattering particles is smaller than the wavelength ($d \ll \lambda$). A medium with large scattering particles ($d \gg \lambda$) results in geometric forward scattering with g close to 1 . The regime in between these two extremes with $d \approx \lambda$ and $0 < g < 1$ is best described by Mie theory [48, 51].

2.1.3 Scattering Coefficient

Describing a scattering medium in an intuitive way leads to the question "How strongly does the medium scatter the light?" or in a negative way "How far does light travel before it is scattered in this medium?". To answer the second question, the scattering mean free path length l_s is introduced. Its inverse is the scattering coefficient μ_s that might give an answer to the first question.

$$l_s = \frac{1}{\mu_s}, \quad [l_s] = \text{mm}. \quad (2.9)$$

The scattering coefficient μ_s describes the mean number of scattering events per length element and is connected to the number of scattering particles per unit volume N_p and their scattering cross section $C_{s,p}$ by:

$$\mu_s = N_p C_{s,p}, \quad [\mu_s] = \text{mm}^{-1}. \quad (2.10)$$

Just as the scattering coefficient, the absorption coefficient μ_a can be defined. It is the ratio of light power absorbed per unit volume divided by the incident power per unit area and is given in the unit of mm^{-1} . In the same manner, the absorption length l_a is defined as the inverse of the absorption coefficient $l_a = \frac{1}{\mu_a}$, which describes the average path length a photon travels before it is absorbed.

Added up, the scattering coefficient and the absorption coefficient will give the extinction coefficient μ_{ex} :

$$\mu_{\text{ex}} = \mu_{\text{s}} + \mu_{\text{a}}. \quad (2.11)$$

This coefficient describes the decrease of intensity of unscattered light in the initial direction.

2.1.4 Beer-Lambert-Law

If a beam of light with the incident power P_0 is propagating in the direction of z , the remaining power $P(z)$ of the light beam at the position z is given by the Beer-Lambert law:

$$P(z) = P_0 \exp \left(- \int_0^z \mu_{\text{ex}}(z') dz' \right). \quad (2.12)$$

For homogeneously allocated scattering particles ($\mu_{\text{ex}}(z) = \text{const.}$), Equation 2.12 simplifies to

$$P(z) = P_0 \exp [-\mu_{\text{ex}}z]. \quad (2.13)$$

With Equation 2.12, the probability distribution f_z along z can be derived. The probability that a photon with a starting point at $z_0 = 0$ is scattered or absorbed between 0 and z is given by

$$f_z = \mu_{\text{ex}} \exp \left(- \int_0^z \mu_{\text{ex}}(z') dz' \right), \quad (2.14)$$

or once again in a homogeneous medium, with $\mu_{\text{ex}} = \text{const.}$, it may be simplified to

$$f_z = \mu_{\text{ex}} \exp [-\mu_{\text{ex}}z]. \quad (2.15)$$

Out of these considerations, the mean free path length l_{ex} a photon is moving in average before it is scattered or absorbed can be derived. For an infinitely extended, homogeneous medium the mean free path length is

$$l_{\text{ex}} = \int_0^{\infty} z f_z dz = \frac{1}{\mu_{\text{ex}}}. \quad (2.16)$$

2.1.5 Reduced Scattering Mean Free Path Length

As mentioned in Section 2.1.3, the most intuitive variable to describe the scattering of light in a medium is the scattering mean free path length l_{s} . To describe

the overall behavior of light in a scattering medium, the transport mean free path length l_t was used in Section 2.1.2. The transport mean free path length l_t is a measure for the distance in a medium until the propagation direction is randomized. The connection between these two quantities is the anisotropy factor that is the average of the cosine of the scattering angle $g = \langle \cos(\theta) \rangle$

$$l_t = \frac{l_s}{1 - g}. \quad (2.17)$$

For a better understanding of l_t , let's take a look at the extreme cases of g : In the case of isotropic scattering, the anisotropy factor will be zero, thus, the transport and the scattering mean free path length will be just the same, $l_t = l_s$. If a medium has solely forward scattering, the path of light will not be changed due to scattering events, although the scattering mean free path length l_s might be very small and a lot of scattering events may happen. In this case, l_t accounts for the forward scattering and as stated in Equation 2.17, l_t will become infinite. In Chapter 3, the transport mean free path length will be the main measure for scattering media.

Just like the scattering mean free path length, the scattering coefficient has its counterpart as well:

$$l_t = \frac{1}{\mu_t} \quad (2.18)$$

and thus:

$$\mu_t = \mu_s(1 - g). \quad (2.19)$$

2.1.6 Radiometric Quantities

To have all tools in hand to follow the derivation of energy transport on the next couple of pages, some radiometric quantities have to be introduced. First, the main radiometric quantity to describe energy propagation by light in transport theory is the radiance L :

$$L(\vec{r}, \hat{s}, t), \quad [L] = \text{W m}^{-2} \text{ sr}^{-1}. \quad (2.20)$$

The radiance L is defined as the average power that flows through a unit area facing the direction of \vec{s} at position \vec{r} and at time t .

Integration over the entire solid angle leads to the irradiance or fluence rate Φ :

$$\Phi(\vec{r}, t) = \int_{4\pi} L(\vec{r}, \hat{s}, t) d\Omega, \quad [\Phi] = \text{W m}^{-2}. \quad (2.21)$$

The irradiance Φ is a measure for the power that flows through a unit area at position \vec{r} and at time t from any possible direction. Division by the speed of

light in the medium $v = c_0/n$ (where n is the refractive index of the background medium) or the photon energy $h\nu$ gives us the density u and the photon density n_p respectively:

$$u(\vec{r}, t) = \frac{\Phi(\vec{r}, t)}{v}, \quad [u] = \text{J m}^{-3} \quad (2.22)$$

and

$$n_p(\vec{r}, t) = \frac{u(\vec{r}, t)}{h\nu}, \quad [n_p] = \text{m}^{-3}. \quad (2.23)$$

The direction and the amount of net flux of power is given by the energy flux vector:

$$\vec{J}_e(\vec{r}, t) = \int_{4\pi} L(\vec{r}, \hat{s}, t) \hat{s} d\Omega, \quad [\vec{J}_e] = \text{W m}^{-2}. \quad (2.24)$$

2.1.6.1 Radiative Transfer Equation

The radiative transfer equation (RTE) describes the transport of radiative energy in a turbid medium in a phenomenological way. It lacks a complete formulation accounting for all effects involved in light propagation. Effects like interference, polarization, or wavelength dependencies are neglected. Nevertheless, it is a useful model for many practical problems. The RTE is an integro-differential equation that can be understood as a formula that gives insight into the simple scattering and absorption processes, that might change the radiance in a certain region. The time-dependent RTE reads as

$$\begin{aligned} & \underbrace{\frac{1}{v} \frac{\partial}{\partial t} L(\vec{r}, \vec{s}, t)}_{1.} + \underbrace{\nabla \cdot (\vec{s} L(\vec{r}, \vec{s}, t))}_{2.} + \underbrace{(\mu_a + \mu_s) L(\vec{r}, \vec{s}, t)}_{3.} \\ & = \underbrace{\mu_s \int_{4\pi} p(\vec{s}, \vec{s}') L(\vec{r}, \vec{s}', t) d\Omega'}_{4.} + \underbrace{q(\vec{r}, \vec{s}, t)}_{5.}, \end{aligned} \quad (2.25)$$

with the source term $q(\vec{r}, \vec{s}, t)$.

- Term (1.) describes the total temporal change of energy in the volume element dV , solid angle $d\Omega$ and time interval dt along the propagation direction \vec{s} . The origins of the change in energy are described by the following terms. In case of a stationary source term (1.) disappears.
- Term (2.) accounts for the energy propagating away from \vec{r} in the direction of \vec{s} .

- Term (3.) represents the photon loss due to absorption and scattering in $dV d\Omega dt$. μ_a and μ_s are the time-independent and direction-independent absorption and scattering coefficients, respectively.
- Term (4.) accounts for the energy which comes from an arbitrary direction \vec{s}' and is scattered in dV into the direction \vec{s} .
- And lastly, term (5.) is the source term which considers sources in the volume element dV that generate light along the propagation direction \vec{s} .

Unfortunately, solving the RTE is not an easy task. But there are two possible paths: Either this equation can be solved numerically or some approximations can be applied to find an analytical solution. Solving this equation numerically will be discussed in Section 2.4. There, a Monte Carlo algorithm will be introduced which is quite efficient but still lacks the benefits of an analytical solution. The other path will be discussed on the next couple of pages. With some approximations, the RTE can be transformed into the Light Diffusion Equation, which opens a lot of opportunities for designing devices that control the flow of light in scattering media.

2.1.6.2 Dependency on Absorption of the RTE

Changing the modeling of absorption is the first simplification of the RTE. If it is possible to find a solution for Equation 2.25 without absorption ($L(\vec{r}, \vec{s}, t, \mu_a = 0)$), it is also possible to change this solution to one that accounts for absorption as long as it is homogeneous ($\mu_a(\vec{r}) = \text{const.}$). As photons do not interact with each other, we can set the source term $q(\vec{r}, \vec{s}, t)$ to be a Dirac delta function. Solutions for other source terms can be added up [52]. Therefore, the solution with absorption is

$$L(\vec{r}, \vec{s}, t, \mu_a) = L(\vec{r}, \vec{s}, t, \mu_a = 0) \exp(-\mu_a vt), \quad (2.26)$$

with μ_a as the absorption coefficient of the medium and v as the speed of light in the medium. Like this, the lifetime $\tau = -\frac{1}{\mu_a vt}$ can be introduced. As mentioned before, this kind of absorption results from the assumption, that scattering does not influence the absorption. Only the overall path length in the background medium determines the absorption. As long as the refractive index is homogeneous in the background medium, all photons released at the same time $t = 0$ by the source will travel the same distance $l = vt$ within a certain time $t > 0$. As it is used later, we can already define the diffusion length that is a measure for the distance photons travel before they are absorbed:

$$l_D = \sqrt{D\tau} \quad (2.27)$$

Without absorption ($\tau \rightarrow \infty$ and $l_D \rightarrow \infty$), both measures, the lifetime τ and the diffusion length l_D that mimic the influence of absorption become infinite.

2.1.6.3 Static and Time-Dependent Light Diffusion Equation

The diffusion approximation [53] is one approach to simplify the integro-differential RTE as it cannot be solved analytically. This diffusion approximation mainly consists out of two individual approximations that have to be applied to the RTE to obtain the diffusion equation. These two simplifications and the conversion of the RTE to the diffusion equation will be shown in the following.

The first assumption is about the radiance L . If the radiance is almost isotropic, one can stop a series expansion after two orders in spherical harmonics:

$$L(\vec{r}, \vec{s}, t) = \frac{1}{4\pi} \Phi(\vec{r}, t) + \frac{3}{4\pi} \vec{J}_e(\vec{r}, t) \cdot \vec{s}. \quad (2.28)$$

This holds true for multiple scattering, as for a randomized propagation, the radiance becomes almost isotropic. This simplification is not applicable if either the medium is too small or the absorption is too high as in these cases, there is no chance photons being scattered multiple times.

The second assumption is about the time variation of the energy flux vector \vec{J}_e . If the time variance is small compared to the vector itself, one can write:

$$\frac{l_t}{v} \left| \frac{\partial \vec{J}_e(\vec{r}, t)}{\partial t} \right| \ll \left| \vec{J}_e(\vec{r}, t) \right|. \quad (2.29)$$

This restriction is fulfilled as well if scattering is the dominant process in light transport. As a summary, a simple checklist in terms of sample properties, will be provided here [46]:

- Scattering has to dominate over absorption: $\frac{\mu_t}{\mu_a} > 10$.
- The smallest dimension of the medium L_{\min} has to be at least 10 times larger than the transport mean free path length l_t : $L_{\min} \geq 10l_t$.
- Every photon has to have a path length of at least $4l_t$ inside the medium and therefore, undergo $\gtrsim 4/(1-g)$ scattering events before detection.

If one or more points are not accomplished, light transport can not be described by the diffusion equation. Designing a device for diffusive light that obeys these rules will always lead to a low transmission, as there will always be a lot of back reflection. The goal in Chapter 3 is to investigate how fast the behavior of light changes when these rules are broken.

With these assumptions, the RTE can be rewritten as the diffusion equation. First, we get the continuity equation by integrating the RTE without absorption over the complete solid angle:

$$\frac{1}{v} \frac{\partial}{\partial t} \Phi(\vec{r}, t) + \vec{\nabla} \cdot \vec{J}_e(\vec{r}, t) = \int_{4\pi} q(\vec{r}, \vec{s}, t) d\Omega. \quad (2.30)$$

By using the two diffusion approximations mentioned above and integrating over the whole solid angle, Fick's first law is deduced from the RTE (see Equations 2.28 and 2.29). As a result, Fick's first law is obtained as

$$\vec{J}_e(\vec{r}, t) = -\frac{l_t}{3} \left(\vec{\nabla} \Phi(\vec{r}, t) - 3 \int_{4\pi} q(\vec{r}, \vec{s}, t) \vec{s} d\Omega \right), \quad (2.31)$$

which connects the energy flux to the gradient of the fluence rate. Next, we introduce the photon flux vector

$$\vec{J}(\vec{r}, t) = \frac{\vec{J}_e(\vec{r}, t)}{h\nu}, \quad [J] = \text{m}^{-2} \text{s}^{-1}, \quad (2.32)$$

which is a measure for the amount of photons traveling in a certain direction at a given time and position.

Now, Fick's law can be expressed in terms of the photon density

$$\vec{J}(\vec{r}, t) = -D \left(\vec{\nabla} n_p(\vec{r}, t) - \frac{3}{h\nu} \int_{4\pi} q(\vec{r}, \vec{s}, t) \vec{s} d\Omega \right). \quad (2.33)$$

D is called the photon diffusivity which is something like a "photon-conductivity" of the material. It is only dependent on the refractive index and the transport mean free path length of the medium:

$$D = \frac{1}{3} \frac{c_0}{n} l_t, \quad [D] = \text{m}^2 \text{s}^{-1}. \quad (2.34)$$

By plugging Equation 2.33 into Equation 2.30, the diffusion equation for the photon density is obtained as

$$\vec{\nabla} \cdot (D \vec{\nabla} n_p(\vec{r}, t)) - \frac{\partial n_p(\vec{r}, t)}{\partial t} = q_0(\vec{r}, \vec{s}, t), \quad (2.35)$$

with $q_0 = \frac{1}{v \cdot h\nu} (3 \vec{\nabla} \cdot [D \int_{4\pi} q \vec{s} d\Omega] - \int_{4\pi} q d\Omega)$ being the new source term. As mentioned above, it is easy to introduce absorption once again (as long as it is much smaller than the scattering counterpart). As we see in Equation 2.26, an exponential factor is used to simulate absorption. This results in the additional term $\mu_a v n_p(\vec{r}, t)$ for the diffusion equation:

$$\vec{\nabla} \cdot (D \vec{\nabla} n_p(\vec{r}, t)) - \frac{\partial n_p(\vec{r}, t)}{\partial t} = \mu_a v n_p(\vec{r}, t) + q_0(\vec{r}, \vec{s}, t). \quad (2.36)$$

Looking closely at the time-dependent light-diffusion equation without a source term:

$$\vec{\nabla} \cdot (D\vec{\nabla}n_p(\vec{r}, t)) - \frac{\partial n_p(\vec{r}, t)}{\partial t} = 0, \quad (2.37)$$

similarities to other equations, as for example the equation for heat conduction

$$\vec{\nabla} \cdot (\kappa\vec{\nabla}T(\vec{r}, t)) - c\rho\frac{\partial T(\vec{r}, t)}{\partial t} = 0, \quad (2.38)$$

are obvious. This can be neat when thinking of designs and applications for devices of diffuse-light transport. With some translation of temperature to photon density etc. one can transfer ideas from one topic to the other.

2.2 LAMINATES IN DIFFUSE LIGHT

One of the basic ideas to control the flow of light in a scattering medium are laminates. The simplest laminate structure is formed by a repetitive stack of two layers A and B with different material properties. Laminates are a simple way to generate anisotropy in an effective material, as the directions in plane of the layers has different effective material properties than the direction out of plane. Laminate structures are known from many other fields of physics. If heat conduction should be low in one specific direction, one can use a stack of different materials to prevent for example heat loss [54]. In mechanics, aviation is using laminate structures to achieve anisotropic material parameter [55]. In the following, I will give a short introduction to the usage of simple laminates in diffuse optics. A more detailed description of laminate properties can be found in the textbook of G. Milton [56].

In Figure 2.2 a structure out of two different isotropic materials A and B is shown. A laminate period a consists of two layers and the layer thickness of both media is equal, $a/2 = L_A = L_B$. The diffusivity of those layers are D_A and D_B , respectively. As it might be easier to imagine what is happening in a laminate structure in electrostatics, the diffusivity can be seen as the electric conductivity σ and the photon density n_p as the electrostatic potential $\Phi(\vec{r})$. Simplifying this problem further, one of the two diffusivities in the laminate is equal to zero, for instance $D_A = 0$. In electron transport this means that the material is an isolator. Translating this to light diffusion, Laminate A would be a diffuse reflector and any photon current normal to the layers would be zero. The current parallel to the layers, however, is finite. In this extreme case it is obvious, that with very simple means, we created a structure with anisotropic material properties. For thin laminates, the effective diffusivity can be written as a tensor.

By aligning the layers parallel to the coordinate system, the diffusivity tensor is given by [56, 57]

$$\vec{D} = \begin{pmatrix} D_{xx} & 0 & 0 \\ 0 & D_{yy} & 0 \\ 0 & 0 & D_{zz} \end{pmatrix}. \quad (2.39)$$

The effective diffusivities in y and z -direction, which are parallel to the laminates, are given by

$$D_{yy} = D_{zz} = \frac{D_A + D_B}{2} \quad (2.40)$$

and in x -direction perpendicular to the layers by

$$\frac{1}{D_{xx}} = \frac{1}{2} \left(\frac{1}{D_A} + \frac{1}{D_B} \right). \quad (2.41)$$

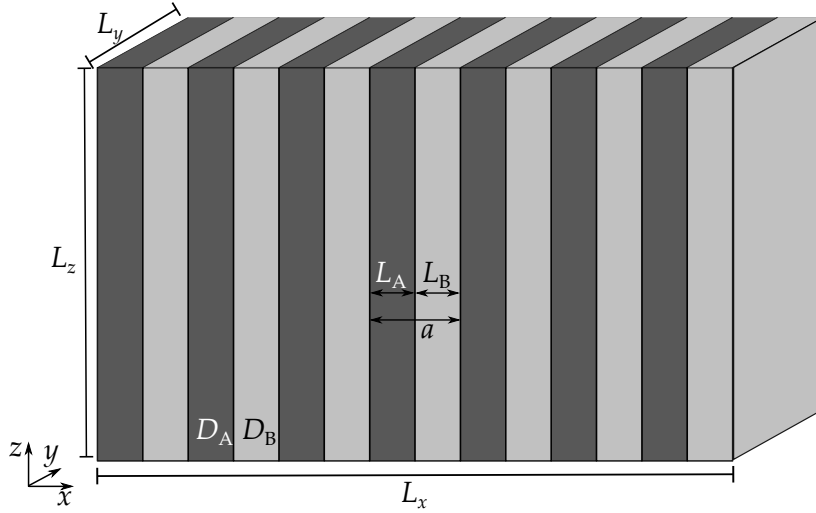


Figure 2.2: Schematic illustration of a laminate. The structure consists of two equidistant layers, A and B, with layer widths L_A and L_B and diffusivities D_A and D_B . The dimensions of the structure are L_x , L_y and L_z . Figure adapted from [42].

These formulas have the same form as the formulas to calculate the resistance or the electric conductivity of resistors that are connected in parallel or in series. The ratio of diffusivity in y -direction to diffusivity in x -direction is given as

$$\frac{D_{yy}}{D_{xx}} = \frac{(1+s)^2}{4s}, \quad (2.42)$$

with $s = D_B/D_A$. With this basic knowledge on laminates in diffusive media, the transition from diffuse to ballistic light transport in such devices will be investigated in Chapter 3.

2.3 CORE-SHELL CLOAKING

In this section, an invisibility cloak design will be introduced, allowing the cloaking in diffusive media. The design of the cloak can be explained by two approaches: The more simple approach is the theory of neutral inclusions developed by E. Kerner [35, 36] in his two papers about elastic and electrical properties of composite media. The other more general approach is using transformation optics introduced in 2006 by J. Pendry [1] and U. Leonhard [58].

First, however, invisibility cloaking and some of its limits are explained.

2.3.1 Invisibility Cloaking and its Limits

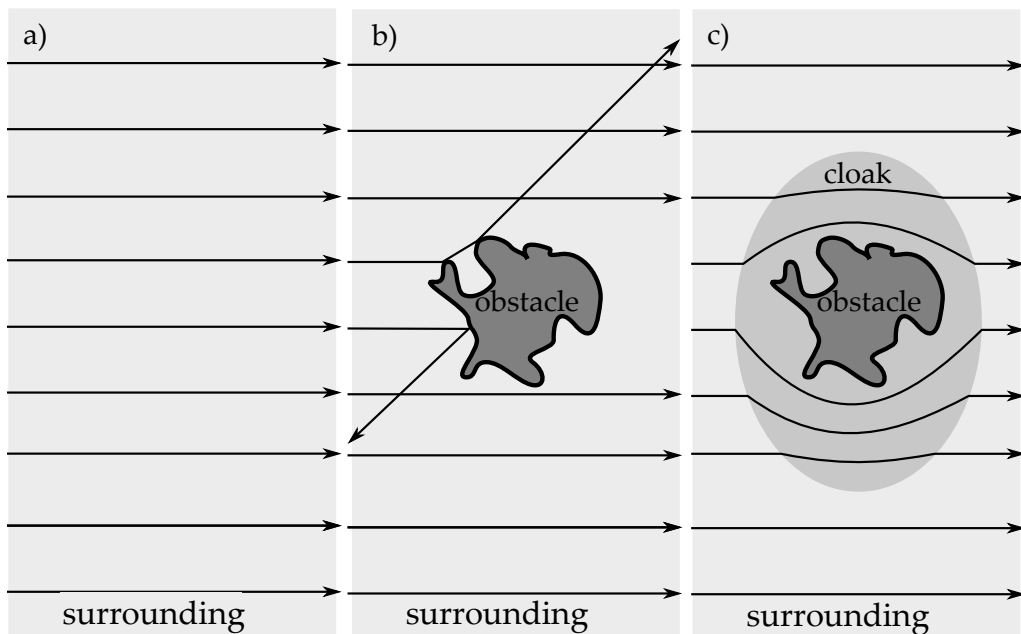


Figure 2.3: Concept of invisibility cloaking. a) Without any object, light travels from the light source, left, to the observer in the right. b) If there is an obstacle, the light rays are diverted and the observer sees a difference, as the density of light rays on the right side of the sample is altered by the obstacle. c) If there is a cloak around the obstacle, that guides the light around it, the observer would notice no difference to a).

In principle, an optical invisibility cloak is a device which hides an object in a way that the observer is unable to see it. In Figure 2.3 a schematic illustration of such a device is shown. Here, the black arrows show the bent path of light around the obstacle, if hidden by a cloak.

Without the obstacle and cloak (see left panel of Figure 2.3) the light rays go straight through the sample area. Here, the very first limitation of free space cloaking is obvious: If light is guided around an object (see right panel of Figure 2.3), the detour around the object always adds up to the light path it would have without the cloaking device [34]. The only way to hide this detour and the corresponding time delay is to speed up the light in the cloak area. In free space, light is already traveling with c_0 and cannot be accelerated. There are exceptions, if we only look at a small frequency band in resonant structures [2], but in general, designing time accurate invisibility cloaking devices for a broad frequency spectrum in vacuum is impossible [34].

The general limitation by the special relativity theory is not present in other areas of physics, for instance in heat transport [28] or mechanics [59]. However, a solution to circumvent this limitation is to decrease the light velocity in the surrounding medium. In diffusive media, there is no fixed speed for the overall light propagation, as light propagation is not ballistic due to multi-scattering. The time a photon stays in the medium is higher, because the path length of the individual photons in the sample is dependent on the number of scattering events. Therefore, the upper limit of the speed of light c_0 is not a problem for cloaks in the regime of diffuse-light transport. Still there are limitation concerning the transient cloaking in diffuse-light [39].

2.3.2 Realization of a Core-Shell Cloak

In 1956, E. Kerner had a closer look at the behavior of the effective electric conductivity of different materials [35, 36]. He came up with a material, that consists solely out of so-called neutral inclusions. He defined these neutral inclusions as a circular shaped area¹ with conductivity σ_1 surrounded by a ring-shaped area with conductivity σ_2 . Filling a sample area with these neutral inclusions by scaling them to fill the whole area, one gets the desired material (see Figure 2.4).

For this material, he showed that it behaves the same as a homogeneous material with a conductivity σ_0 . Following this line of reasoning, one does not change the behavior of the sample area by replacing most of the constituent material with a homogeneous material with conductivity σ_0 . Having only one neutral inclusion left (see Figure 2.5), one ends up with a local variation in the conductivity in the sample area that is “invisible” as the overall conductivity does not change.

As the static basic equations for light diffusion and electric conductivity are quite similar, one can translate this phenomena from electric conductivity to

¹ For simplicity we have a look at the 2D case only. When translating to the 3D case, the findings are valid for cylindrical shapes instead of circular shapes in 2D.

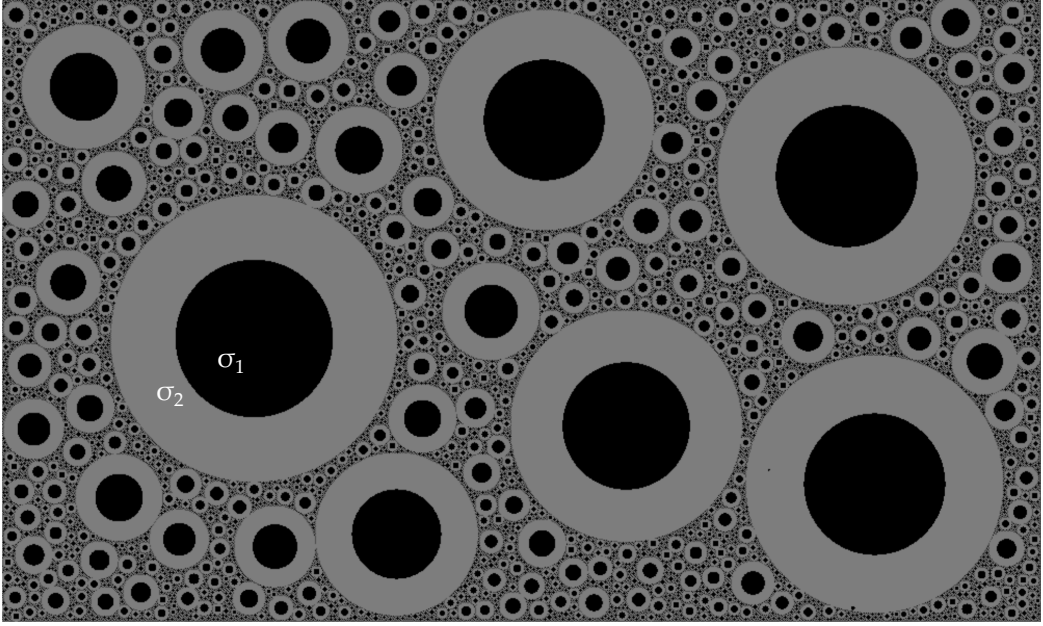


Figure 2.4: Area randomly filled with neutral inclusions. Different colors correspond to different conductivities σ_1 and σ_2 . An area filled like this behaves just the same as an area with a homogeneous distribution of a single conductivity σ_0 .

diffusive light transport again.

The equation for electric conductivity reads:

$$\vec{\nabla} \cdot (\sigma \vec{\nabla} \Phi(\vec{r})) = 0, \quad (2.43)$$

where σ is the electric conductivity and $\Phi(\vec{r})$ the electrostatic potential. The static diffusion equation looks very much alike:

$$\vec{\nabla} \cdot (D \vec{\nabla} n(\vec{r})) = 0. \quad (2.44)$$

Therefore, it is possible to translate the line of reasoning E. Kerner presented in 1956 to diffusive light transport. All conductivities have to be replaced by diffusivities resulting in a neutral inclusion in diffuse-light with diffusivities D_1 in the core of the inclusion, D_2 in the shell of the neutral inclusion and D_0 in the surrounding area (see Figure 2.6).

Using the Hashin-Shtrikman formula [37, 56], it is possible to find an analytical formula connecting the diffusivities and the radii. The only additional prerequisite is a constant gradient of the photon density ($\vec{\nabla}_p = \text{const.}$). This translates to a homogeneous illumination in our case. Under these circumstances one finds:

$$\frac{R_2}{R_1} = \sqrt{\frac{(D_2 + D_0)(D_2 - D_1)}{(D_2 - D_0)(D_2 + D_1)}}. \quad (2.45)$$

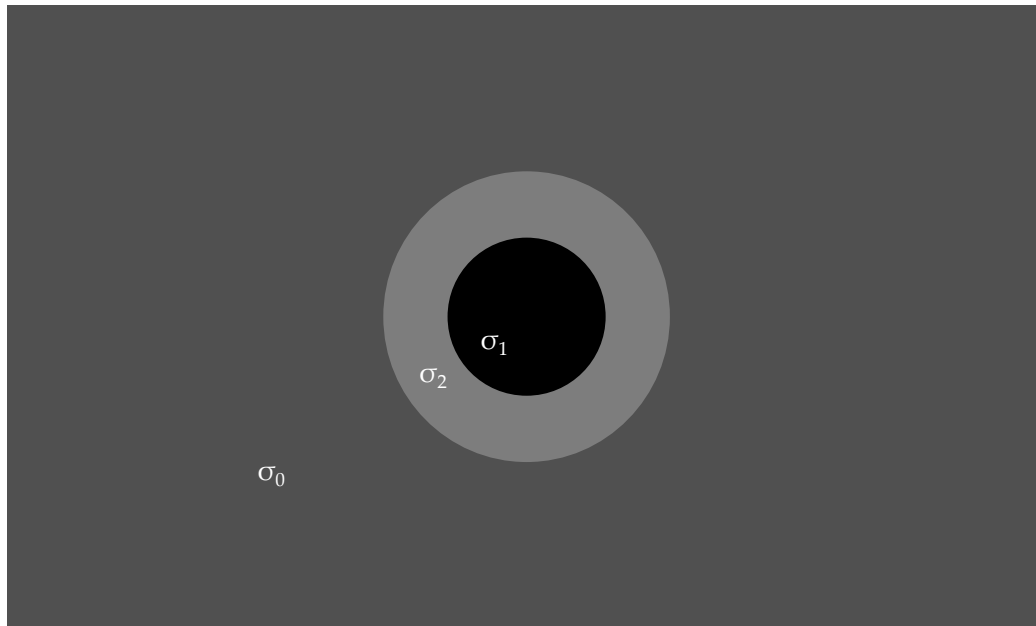


Figure 2.5: One neutral inclusion in electric conductivity. The rest of the area is filled with a material of homogeneous conductivity σ_0 . The electrical behavior of this device is the very same as the one shown in Figure 2.4.

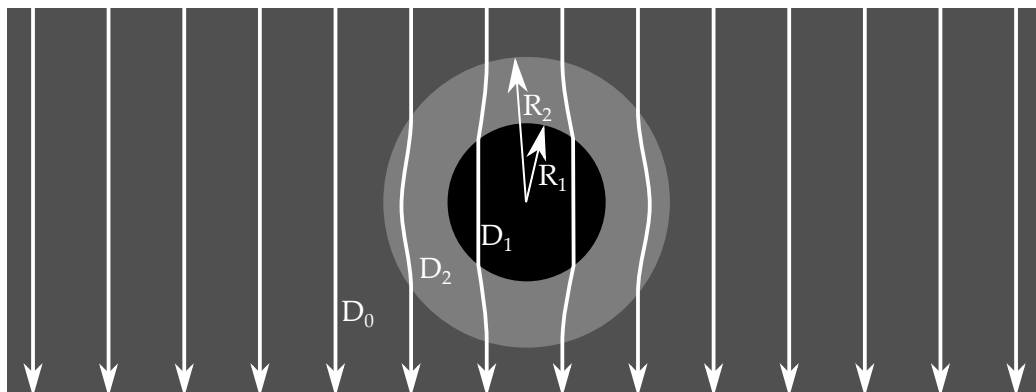


Figure 2.6: One invisible neutral inclusion in diffuse-light. The streamlines of light are bent due to higher or lower diffusivity. After crossing the neutral inclusion, the streamlines are evenly spaced and parallel. Hence, the inclusion does not affect the flow of light outside of the inclusion itself.

As in electric conductivity, the translated neutral inclusion in diffuse-light is invisible to the observer. In diffuse-light optics, that means, that the photon flux outside of the neutral inclusion is not affected by the inclusion. Invisibility is only the first step towards a successful design of an invisibility cloak. An invisibility cloak has to be able to hide things that are not invisible itself. To achieve that,

one can use the fact, that until now, there are three free variables and only one equation to fulfill (Equation 2.45). If one sets $D_1 = 0$, the inner core of the neutral inclusion will have a transport mean free path length of $l_t = 0$ and thus the light will not penetrate the area as the core will act as a diffuse reflector. If the light does not penetrate the core, one can cut out a circular hole in the middle of the inclusion where objects can be hidden. As there is no light in the core, this does not change the photon flux of the overall sample area (see Figure 2.7).

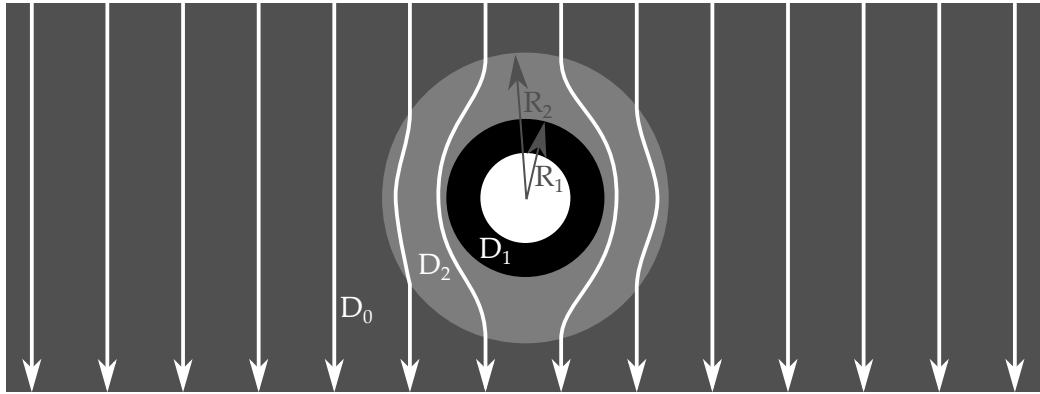


Figure 2.7: Diffuse-light invisibility cloak. With diffusivity $D_1 = 0$, there is no light flow at all in the core of the neutral inclusion. Hence a hole can be cut out of this core area. By providing an area to hide things, the invisible neutral inclusion becomes an invisibility cloak.

Fixing D_1 to zero changes Formula 2.45 to

$$\frac{R_2}{R_1} = \sqrt{\frac{D_2 + D_0}{D_2 - D_0}}. \quad (2.46)$$

Equation 2.46 can be used as a recipe to design diffuse-light cloaks. For fixed radii and surrounding diffusivity D_0 the shell diffusivity D_2 can be calculated. Please note, that for a very thin shell ($R_1 \approx R_2$) Equation 2.46 results in $D_2 \gg D_0$. As mentioned in Section 2.1 that might harm the diffusion approximation. Hence, one has to be careful when designing a diffuse-light cloak as not only Equation 2.46 but also the diffusion approximations have to be met.

2.3.3 Transformation Optics

As stated earlier, a more general approach to invisibility cloaks or bending the light in general is transformation optics. The concept of neutral inclusions introduced in Section 2.3.2 can be interpreted as an extremely simplified version of a cloak

originating from transformation optics. In this section a small introduction into transformation optics in the context of diffuse-light is given, to lay the foundation for some general conclusions about all diffuse-light cloaks.

Transformation physics enabled the design of many cloaking devices, for example for electro-magnetic waves [2–10], acoustic waves [11–13], elasto-mechanical waves [14–20], static electrical currents [21–23], magnetostatics [24–26], and in heat transport [24–26].

In this section, we will have a look at the mathematical basis for transformation optics in diffuse-light. We will not deduct a specific cloaking device with the core-shell cloak introduced in Section 2.3.2, there already is a capable, relatively easy to fabricate candidate. Cloaks deducted from transformation optics with less tradeoffs would need more shells around the core. The flaws connected to this design will be discussed in Chapter 3.

Invisibility cloaks based on transformation optics are designed in two steps. First, a set of new material parameters is calculated based on a virtual spatial coordinate transformation. This is feasible as long as the underlying physical equations are form-invariant under transformation. As these newly obtained parameters are in general anisotropic, the second step of finding the right materials to realize an invisibility cloak is a challenging one as well. Here the first step and the mathematical consequences for cloaks in diffuse-light are outlined.

To start, the stationary ($\partial/\partial t = 0$), source-free ($q_0 = 0$), and absorption-free ($\mu_a = 0$) diffusion equation (see Equation 2.36) for the photon density n_p is:

$$\vec{\nabla} \cdot (D_0 \vec{\nabla} n_p) = 0. \quad (2.47)$$

If one performs a spatial transformation that maps the coordinates (x, y, z) onto (x', y', z') , we get

$$\vec{\nabla}' \cdot (\vec{D} \vec{\nabla}' n_p) = 0. \quad (2.48)$$

Here, the diffusivity is a tensor given by

$$\vec{D} = D_0 \overset{\leftrightarrow}{J} \overset{\leftrightarrow}{J}^T \frac{1}{\det \overset{\leftrightarrow}{J}}. \quad (2.49)$$

The Jacobian matrix $\overset{\leftrightarrow}{J}$ consists of the first-order partial derivatives:

$$\overset{\leftrightarrow}{J} = \begin{bmatrix} \frac{\partial x'}{\partial x} & \frac{\partial x'}{\partial y} & \frac{\partial x'}{\partial z} \\ \frac{\partial y'}{\partial x} & \frac{\partial y'}{\partial y} & \frac{\partial y'}{\partial z} \\ \frac{\partial z'}{\partial x} & \frac{\partial z'}{\partial y} & \frac{\partial z'}{\partial z} \end{bmatrix}. \quad (2.50)$$

In general, the diffusivity is a tensor and its anisotropy material parameters are calculated by this transformation. Usually, these anisotropic material parameters

can only be met by composite media, for example laminates. Some basics on laminates and their features in diffuse-light can be found in Section 2.2 and in Chapter 3.

If we have a closer look at the time-dependent, absorption-free and source-free diffusion equation, the procedure is almost the same [60]. In the diffusion equation (Equation 2.47), there is an additional time-dependent term

$$\vec{\nabla} \cdot (D_0 \vec{\nabla} n_p) - \frac{\partial n_p}{\partial t} = 0. \quad (2.51)$$

Performing once again a coordinate transformation from $(x, y, z) \rightarrow (x', y', z')$, we get:

$$\vec{\nabla}' \cdot \left(D_0 \overset{\leftrightarrow}{J} \overset{\leftrightarrow}{J}^T \frac{1}{\det \overset{\leftrightarrow}{J}} \vec{\nabla}' n_p \right) - \frac{1}{\det \overset{\leftrightarrow}{J}} \frac{\partial n_p}{\partial t} = 0. \quad (2.52)$$

Just as before, we can map the new variables behind D_0 into a new diffusivity tensor. Though, there is no variable in front of the second, time dependent term. The change of $\frac{1}{\det \overset{\leftrightarrow}{J}}$ cannot be hidden by changing a material parameter. Therefore, perfect time dependent cloaking in diffuse-light can only be achieved with $\frac{1}{\det \overset{\leftrightarrow}{J}} = 1$, and thus, $\det \overset{\leftrightarrow}{J} = 1$. This, however, is only the case when the Jacobian is unimodular under spatial transformations, which means that the transformation does not stretch or compress space.

Nevertheless, an invisibility cloak always needs to have an area that is hidden. This area can only be created by compressing space somewhere else. Attempts to circumvent this fact have also been published [60] but in the end these cloaks work only for a very small illumination window, as the authors shifted the compression far away from the center of the cloak.

As a consequence, in general, all cloaks designed for diffuse-light can be revealed by transient illumination and detection [39].

2.4 MONTE CARLO RAYTRACING

In Section 2.1.6.1, approximations had to be applied to find analytical solutions for the RTE (see Equation 2.25). As mentioned at that point, there is another possibility to solve this problem. Due to the amount of scattering events and particles as well as the large span between the smallest and largest length scale that have to be considered in the problem, most common numerical approaches fail due to the huge amount of data that is necessary to define the media one is looking at. A nice way to circumvent this problem is, to avoid defining the scattering structure in a classical way. Usually, one rolls the dice for the position of each scattering particle in the observed medium. The Monte Carlo method takes another approach: There are no fixed scattering particles. There is only a scattering coefficient defined for each medium. Therefore, the dice is rolled for every scattering event and not for every scattering particle.

In this section, an overview of the working principle of the Monte Carlo method of raytracing will be given in Section 2.4.1. Afterwards, an implementation programmed by R. Schittny and F. Mayer [40] will be briefly introduced in Section 2.4.2.

2.4.1 Working Principle of the Monte Carlo Method

We consider a point source (see Section 2.1.6.1) that emits photons in one specific direction and is described by the probability functions f_ϕ , f_θ and f_z that were introduced in Sections 2.1.2 and 2.1.3. With this assumption the Monte Carlo method consists of five steps repeated for every photon simulated:

- (i) The starting position \vec{r}_p and direction \vec{v}_p are chosen according to the characteristics of the defined light source.
- (ii) A random step length l is derived from f_z as defined in Equation 2.14.
- (iii) The photon propagates from position \vec{r}_p to $\vec{r}'_p = \vec{r}_p + l \cdot \vec{v}_p$.
- (iv) The scattering angles θ and ϕ are chosen randomly by using f_θ and f_ϕ (Equations 2.2 and 2.5). The direction of the photon after the scattering event \vec{v}_p is updated.
- (v) Steps (ii)-(iv) are iterated until either the photon leaves the medium or is absorbed. Afterwards, the exit position, the overall path length and the number of scattering events is saved and another photon is initiated (step (i)).

Repeating this for millions of photons and storing their exit positions leads to a solution resembling the radiative transfer equation, although, said equation is not

directly implemented in the algorithm itself. Using the overall path length of the photons, one can even derive time-resolved information by exploiting the fact that the speed of light in the scattering medium is only dependent on the refractive index of the host material.

Light sources emitting light over a finite solid angle or within a finite area can be constructed by adding up the results derived for multiple tilted or shifted point sources.

A crucial point in implementing the algorithm into a code that can be run on a computer is the generation and conversion of random variables to their specific probability distribution. For every loop in the Monte Carlo method mentioned above, one needs three random numbers denoted as ξ_1 , ξ_2 and ξ_3 . Computers usually give you a random number in the interval of $[0, 1)$ with an equal distribution. These random numbers then have to be scaled to fit the wanted parameters. For the step length l and the scattering angle ϕ this is not a problem. The step length l_s from one scattering position to the next one is calculated by

$$l(\xi_1) = -l_s \ln(1 - \xi_1). \quad (2.53)$$

The azimuth angle ϕ can be found through

$$\phi(\xi_2) = 2\pi\xi_2. \quad (2.54)$$

The scattering polar angle θ is a little bit more complicated as there exist only numerical solutions to the defining equation. The best way to quickly generate random values for θ is by using an approximation of the phase function allowing for a minimization of the calculations expenses. Therefore, the scattering angle $\theta(\xi_3)$ is determined by inverting the Henyey-Greenstein phase function (Equation 2.6) and reads

$$(\cos \theta)(\xi_3) = \begin{cases} \frac{1}{2g} \left[1 + g^2 - \left(\frac{1-g^2}{1-g+2g\xi_3} \right)^2 \right] & \text{for } g \neq 0 \\ 1 - 2\xi_3 & \text{for } g = 0 \end{cases} \quad (2.55)$$

here $g = \langle \cos(\theta) \rangle$ is the anisotropy factor, that influences the scattering angle θ (see Section 2.1.5).

2.4.2 Implementation of the Algorithm

In the context of my master thesis, R. Schittny and I were facing the challenge to reproduce experimental data with simulations based on the diffusion equations. It turned out that a ray optics approach help to understand the findings. Due to the lack of software packages suitable for our purpose, we decided to program our own software. In 2015, R. Schittny and F. Mayer started from scratch and designed

FRODO (Fast Raytracing fOr Diffusive Optics) [40]. This piece of software uses the programming language C++ and the programming interface CUDA to simulate the path of photons through random media. The most important feature is the possibility to parallelize the calculation. As the photons do not interact with each other, one can start the calculation for multiple photons at the same time and combine the results. This huge amount of parallel computations is done way faster on a GPU than on a CPU and the CUDA package enables the use of the GPU in a graphics card for computations like this.

The goal of the new software was to implement a fast algorithm that is able to simulate light propagation in diffuse-light devices as well as in devices where the diffusion approximation is not met. Restricting the geometry of these devices to simple geometric sections enabled a huge performance boost in comparison to mesh based Monte Carlo software [61]. The geometry is defined by boxes, cylinders, spheres and combinations of these shapes formed by Boolean operators. Every geometry section in the simulation is characterized by a refractive index n , a scattering coefficient μ_s , an anisotropy factor g and an absorption coefficient μ_a . The starting point for photons are given by a point source or an area that emits photons. The photons exit the simulation at a surface that is called the screen. This screen can be subdivided into areas where each exiting photon can be counted individually to derive spatial information.

2.5 PROBABILITY THEORY

Simulating a single photon path as explained in Section 2.4 works fine but does not reveal any relevant information about the medium or device that is simulated. Simulating a lot of photons, on the other hand, does provide a lot of information. This effect known as the “law of large numbers” [62] states, that the average of the outcome of an experiment that is repeated a large number of times will approach the expected value. Based on this effect billions of single photons are simulated in this work to reproduce the expected values observed in real world experiments.

This section, follows the lines of the “Handbook of Mathematics” by I. Bronshtein and K. Semendyayev [63] and will give a short introduction to distribution densities, expected values and variances. The goal is to lay a foundation for the discussion of Gaussian and Lorentzian distribution functions in Section 3.4.

2.5.1 Probability Density Functions

A probability density function (PDF) can be used to construct probability distributions P via integration. To calculate the probability for a value between a and b , one integrates the PDF from a to b [64]. PDFs are real, non-negative and their total integral from minus to plus ∞ is normalized to one. Given a PDF $f(x)$ the probability distribution P for a value X in the interval $[a, b]$ can be calculated as

$$P(a \leq X < b) := \int_a^b f(x) dx. \quad (2.56)$$

A cumulative distribution function of a random variable X with a PDF f_X is given by

$$F_X(x) = \int_{-\infty}^x f_X(t) dt. \quad (2.57)$$

Using this distribution function, the expected value $E[X]$ with its distribution described by the PDF f_X can be calculated by

$$E[X] = \int_{-\infty}^{\infty} x f_X(x) dx. \quad (2.58)$$

x_{med} can be calculated by exploiting the fact that the probability to find a value smaller than x_{med} is one half:

$$\int_{-\infty}^{x_{\text{med}}} f(x) dx = \frac{1}{2}. \quad (2.59)$$

Accordingly, the probability to find a value above x_{med} is also one half

$$\int_{x_{\text{med}}}^{\infty} f(x) dx = \frac{1}{2}. \quad (2.60)$$

For an existing expected value $E(X) = x_0$ of a PDF f_X , one can calculate the variance as

$$\text{Var}(X) = E(X^2) - (E(X))^2 = \int_{-\infty}^{\infty} (x - x_0)^2 f_X(x) dx. \quad (2.61)$$

The variance is a measure for the average width of the spread of the distribution around its mean. The well known standard deviation σ is the square root of the variance:

$$\sigma(X) = \sqrt{\text{Var}(X)}. \quad (2.62)$$

2.5.2 Estimators

An estimator is a rule for calculating the estimate of a quantity given by the observed data [65]. The goal is to predict characteristics of the underlying distributions even with a finite sample set. The distribution of a random sample set with variable X_i describes the probability of a certain outcome at the i -th draw. Estimator functions are dependent on their random sample set and hence are random measures themselves. For a given mathematical sample set (X_1, \dots, X_n) , the function $g_n = g(X_1, X_2, \dots, X_n)$ is called the estimator function if g is a measurable function.

To find an estimator one needs to calculate some parameters of the given population [66]:

First, the expected value of the sample set has to be calculated

$$\bar{x} = \frac{1}{n} \sum_{i=1}^n x_i. \quad (2.63)$$

Here, (x_1, \dots, x_i) is a concrete sample set. The estimator for the empirical variance $\text{Var} = \sigma^2$ of this sample set is

$$\sigma^2 = \frac{1}{n-1} \sum_{i=1}^n (x_i - \bar{x})^2. \quad (2.64)$$

Here, the factor $\frac{1}{n-1}$ is used instead of $\frac{1}{n}$ to get an unbiased estimator. Otherwise, a sample set of just one sample would have a variance of zero. This is known as Bessel's correction [67].

2.5.3 Gaussian Distribution

The Gaussian distribution is one of the most common distributions in mathematics and in nature. Hence, it is also called normal distribution and it can be found for example in the distribution of random errors. The probability density function f of the Gaussian distribution reads as

$$f(x) = \frac{1}{\sqrt{2\pi\sigma^2}} \exp\left(-\frac{(x-x_0)^2}{2\sigma^2}\right). \quad (2.65)$$

Its mean is given by $x = x_0$ and as it is a symmetrical function, its median is $x = x_0$ as well. Conveniently, the variance σ^2 can be directly found in the exponent of the function. Normalization of the function $f(x)$ sets the total integral to one. The cumulative distribution function of the Gaussian distribution is

$$F(x) = \frac{1}{2} \left[1 + \operatorname{erf}\left(\frac{x-x_0}{\sigma\sqrt{2}}\right) \right], \quad (2.66)$$

with the error function $\operatorname{erf}(x)$ which is defined as

$$\operatorname{erf}(x) = \frac{2}{\sqrt{\pi}} \int_0^x \exp(-t^2) dt. \quad (2.67)$$

The full width at half the height of the maximum (FWHM) of the Gaussian distribution is

$$FWHM = 2\sqrt{2\ln 2}\sigma \approx 2.35482\sigma. \quad (2.68)$$

The variance of the Gaussian distribution is calculated using Equation 2.61.

In case of the Gaussian distribution 68% of all values are found within an interval of $\pm\sigma$ around the mean value x_0 . Within $\pm 3\sigma$, 99.7% of all values are found. This indicated that the Gaussian distribution has very light tails in contrast to other functions like the Lorentz distribution.

2.5.4 Confidence Intervals

The confidence interval is a statistical property that gives the possibility to present the uncertainty of an estimator in an easy-to-understand way. With a certain probability (in this work $\alpha = 90\%$ are used) the confidence interval contains the real value of the unknown population parameter. Note, that the mean value does not have to lie within the confidence interval. In Chapters 3 and 5, confidence intervals are used to illustrate the errors on measured variables. For samples that originate from a Gaussian distribution, the upper limit of the confidence interval b_{\max} is given by

$$b_{\max} = x_0 + t_{(1-\alpha/2;n-1)} \frac{\sigma}{\sqrt{n}}, \quad (2.69)$$

with α the confidence level, x_0 the mean of the sample, σ the standard deviation and n the number of observations. $t_{(1-\alpha/2;n-1)}$ is the “Student’s t-distribution” with $\nu = n - 1$ being the degrees of freedom [68]. The lower border of the confidence interval b_{\min} reads as

$$b_{\min} = x_0 - t_{(1-\alpha/2;n-1)} \frac{\sigma}{\sqrt{n}}. \quad (2.70)$$

2.5.5 Lorentz Distribution

Just as the Gaussian distribution, the Lorentz distribution is a continuous probability distribution described by the PDF

$$f(x) = \frac{1}{\pi\gamma} \frac{\gamma^2}{\gamma^2 + (x - x_0)^2} = \frac{1}{\pi\gamma} \frac{1}{1 + \left(\frac{x-x_0}{\gamma}\right)^2}, \quad (2.71)$$

for $x \in (-\infty, \infty)$. The scale factor γ , with $\gamma > 0$, can be considered as an equivalent to the standard deviation σ in the Gaussian distribution. This scale factor marks half the width at half the maximum, hence, $FWHM = 2\gamma$. Just as for the Gaussian distribution $x = x_0$ marks the peak of the distribution.

Its cumulative distribution function is

$$F(x) = \frac{1}{\pi} \arctan\left(\frac{x - x_0}{\gamma}\right) + \frac{1}{2}. \quad (2.72)$$

In contrast to the light tailed Gaussian distribution, the Lorentz distribution is a so-called heavy tailed distribution. This can be expressed as

$$\int_{-\infty}^{\infty} \exp(tx) dF(x) = \infty, \quad (2.73)$$

for all $t > 0$. In other words, the tails of the Lorentz distribution drop slower than an exponential function rises [69].

Due to these heavy tails, the mean, the variance and the standard variation are not defined for the Lorentz distribution. Nevertheless, its median is well defined and is equal to the mean x_0 for symmetric boundaries.

2.5.6 Measure for Gaussian and Lorentzian Distributions

In Chapter 3, the transmission of a scattering medium is observed. Diffusive transmission leads to a spatial distribution of photons on the observed screen that follows a Gaussian distribution, whereas ballistic transmission leads to a

Lorentzian distribution of photons. In between these two extremes, the spatial distribution of exiting photons can be described as a superposition of the two distributions. As it is necessary to find a measure for the width of all respective distributions that is valid in both regimes, a new measure is introduced in this section.

To measure the width of both the Gaussian and the Lorentzian distribution, we use a measure similar to the root mean square $\sigma(x)$, but to lower the impact of the heavy tails, we use the square root of the mean denoted as $w(x)$ given by:

$$w(x) = \left(\int_{-\infty}^{\infty} \sqrt{|x|} f(x) dx \right)^2. \quad (2.74)$$

For only n samples, this distribution can be approximated by

$$w(x) \approx \left(\frac{1}{n} \sum_{i=1}^n \sqrt{|x_i - x_0|} \right)^2. \quad (2.75)$$

Here, x_0 is the mean value of all samples.

To prove the convergence of this measure for both distributions, a Gaussian distribution can be inserted into Equation 2.74:

$$\begin{aligned} w(x) &= \left(\frac{1}{\sqrt{2\pi\sigma^2}} \int_{-\infty}^{\infty} \sqrt{|x|} \exp\left(-\frac{x^2}{2\sigma^2}\right) dx \right)^2 \\ &= \frac{\sqrt{2}}{\pi} \Gamma\left(\frac{3}{4}\right)^2 \sigma \\ &\approx 0.676 \sigma, \end{aligned} \quad (2.76)$$

And the same can be shown for the Lorentzian distribution

$$\begin{aligned} w(x) &= \left(\frac{1}{\pi} \int_{-\infty}^{\infty} \sqrt{|x|} \frac{\gamma}{\gamma^2 + x^2} dx \right)^2 \\ &= 2\gamma. \end{aligned} \quad (2.77)$$

As both distributions lead to a finite value as long as σ and γ are finite, the w -measure can be used for both distributions.

2.6 LASER SPECKLES

Scattering samples will be illuminated by coherent light in Chapters 4 and 5. Due to multiple scattering events in the samples and the interference of the light, an interference phenomenon called speckles will emerge. In this section, we will have a closer look at the origin of speckle patterns and how to characterize them.

Two waves are perfectly coherent, if they match in frequency and waveform and if their phase difference is constant. [50]. The coherence length of a light source is a measure to quantify the distance in which said restrictions are still valid.

2.6.1 Origin of Speckles

In the 1960's, shortly after continuous-wave lasers became commercially available, researchers discovered something strange in their labs [70]: Whenever a laser beam was reflected on a rough surface or transmitted through a diffuse medium, the light formed a granular pattern that seemed to be quite random. The reason is the constructive and destructive interference of light on the observation screen or in the eye of the observer. Let us have a look at a very simple speckle setup.

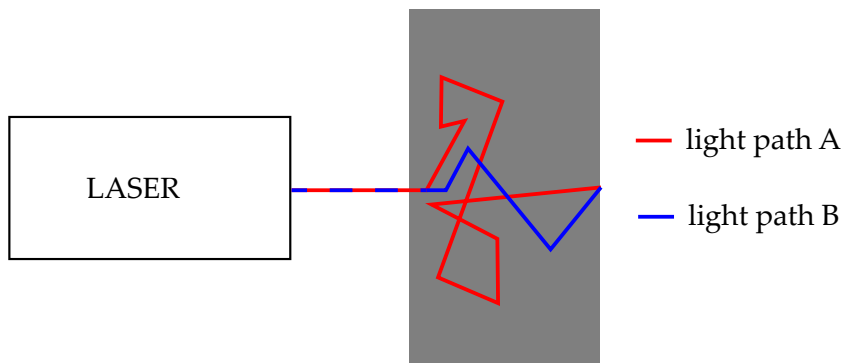


Figure 2.8: Interference in scattering media. Coherent laser light shines on a scattering medium from the left. The red light path A is scattered 9 times and exits the medium. The green light path B is scattered 3 times and exits the medium at the same position.

In Figure 2.8 the schematic origin of laser speckles is shown. Due to different path lengths l_A and l_B , light rays A and B have a path difference of $l_A - l_B = l$. This path difference can be translated into a phase difference by a Euclidean division,

$$l = k \cdot \lambda + \frac{\lambda}{2\pi} \phi, \quad (2.78)$$

where k is an integer number, λ is the wavelength of light and ϕ is the phase difference of the two light rays. For a phase difference of $\phi = 0$, we have constructive interference and with a phase difference of $\phi = \pi$ the result is destructive interference. This results in a bright respectively a dark spot in the speckle pattern. Of course, this effect doesn't only occur for two light rays, but to all scattered light that is falling onto a spot on the detection plane.

There are some reasons why detected speckle patterns are usually not 100% pure.

- There might be some incoherent stray light that creates a constant background in the data.
- There might be different polarizations that do not interfere with each other.
- There might be electrical noise on the detection camera.
- The coherence length might be shorter than the path length difference Δl of the scattering paths.

In a speckle experiment one tries to minimize the first three reasons for an imperfect speckle pattern by blocking all light sources that do not contribute to the interference with sheets and curtains by putting a polarizer in front of the camera and by subtracting a so called background image from the data that is recorded without any light on the camera. After excluding all the other reasons for an imperfect speckle pattern, the following theory may be applied to connect the speckle contrast to the path length distribution of the scattered light rays [71, 72].

2.6.2 Speckle Contrast

In Chapter 4 the speckle contrast C_1 of the transmitted light is recorded in dependence of the coherence length l_{coh} . In order to find a connection between the speckle contrast and the path length distribution $p(l)$ (that is different for the cloak and reference sample), a deviation is presented, that connects the speckle contrast to the coherence length and the path length distribution.

The reasoning below follows the lines of a paper by C. A. Thompson et al. [73] with some adaptations to fit our needs in the context of Chapter 4.

We consider a transmission experiment as shown in Figure 2.8. The incident beam is propagating along the z -axis and we want to have a closer look at a small domain at the front side of the sample ($z = z_i$) centered around x_{i0}, y_{i0} . Here, the

incident optical power spectral density $S(\lambda, x_i, y_i)$ in $\left[\frac{W}{m^3}\right]$ is

$$I_{\text{inc}}(x_i, y_i) = \int_0^{\infty} S(\lambda, x_i, y_i) d\lambda. \quad (2.79)$$

I_{inc} depends on the position (x_i, y_i) within the illumination spot on the sample and its integral over the whole area gives the total incident power.

Corresponding to the power density, we have the complex field spectral amplitude, which depends on the position and the wavelength,

$$U(x_i, y_i, \lambda) = U_r(x_i, y_i, \lambda) + iU_i(x_i, y_i, \lambda) \quad (2.80)$$

and has a real and an imaginary part. For a large number of scattering events, the real and the imaginary part are uncorrelated and their values follow a Gaussian probability density function with zero mean. When writing the complex field spectral amplitudes in polar coordinates as

$$U(x_i, y_i, \lambda) = U_m(x_i, y_i, \lambda) \exp[-i\phi(x_i, y_i, \lambda)], \quad (2.81)$$

the field magnitude parameter U_m is distributed according to a Rayleigh probability density function. The values of the random phase ϕ follow a uniform probability density as long as the path length differences are larger than the wavelength, $l \gg \lambda$. Note the connection between phase and path length difference at a given position:

$$\phi(x_i, y_i, \lambda) = \frac{2\pi}{\lambda} l(x_i, y_i). \quad (2.82)$$

Equation 2.82 only holds true as long as the coherence length is a lot larger than the wavelength $l_c \gg \lambda$.

The normalized intensity random variable I_n is the intensity at position x_i, y_i for a spectral power density of $S(\lambda) = 1$ and can be calculated from the square of the field amplitude U_m as follows:

$$U_m^2(x_i, y_i, \lambda) = S(\lambda) I_n(x_i, y_i, \lambda) = I(x_i, y_i, \lambda). \quad (2.83)$$

Assuming a weak dependence of I_n on the wavelength for small changes in λ , we find the intensity probability density function for monochromatic speckles $p(I, \lambda)$ as

$$p(I, \lambda) = \frac{\exp[-I/2\sigma_I^2]}{2\pi\sigma_I^2}. \quad (2.84)$$

Here σ_I^2 is the variance. In the case, that the observation time is large compared to the coherence time[74], the expected value of the optical power spectral density

can be written as an incoherent superposition:

$$\langle I(x_i, y_i) \rangle = \int_0^{\infty} S(\lambda) \langle I_n(x_i, y_i, \lambda) \rangle d\lambda. \quad (2.85)$$

The expected value of the normalized intensity at a given wavelength $\langle I_n(x_i, y_i, \lambda) \rangle$ can be written as

$$\langle I_n(x_i, y_i, \lambda) \rangle = \int_0^{\infty} S(\lambda) I_n(x_i, y_i, \lambda) p(I, \lambda) dI. \quad (2.86)$$

Here, the probability density function $p(I, \lambda)$ from Equation 2.84 is used. The second moment of $I(x_i, y_i,)$ is

$$\langle I^2(x_i, y_i) \rangle = \int_0^{\infty} \int_0^{\infty} S(\lambda) S(\lambda') \langle I_n(x_i, y_i, \lambda) I_n(x_i, y_i, \lambda') \rangle d\lambda d\lambda'. \quad (2.87)$$

In this equation we find the normalized first-order intensity auto-correlation

$$\Gamma_I(\lambda, \lambda') = \langle I_n(x_i, y_i, \lambda) I_n(x_i, y_i, \lambda') \rangle. \quad (2.88)$$

Therefore, Equation 2.87 can be rewritten with second order statistics:

$$\langle I(x_i, y_i) I(x'_i, y'_i) \rangle = \int_0^{\infty} \int_0^{\infty} S(\lambda) S(\lambda') \langle I_n(x_i, y_i, \lambda) I_n(x'_i, y'_i, \lambda') \rangle d\lambda d\lambda'. \quad (2.89)$$

With Equation 2.83 in mind, one can replace $I_n(x_i, y_i, \lambda) = U_n(x_i, y_i, \lambda) U_n^*(x_i, y_i, \lambda)$ and thus get the following:

$$\langle I_n(x_i, y_i, \lambda) I_n(x'_i, y'_i, \lambda') \rangle = \langle U_n(x_i, y_i, \lambda) U_n^*(x_i, y_i, \lambda) U_n(x'_i, y'_i, \lambda') U_n^*(x'_i, y'_i, \lambda') \rangle \quad (2.90)$$

for expected values of variables w_i following a Gaussian probability distribution [75],

$$\langle w_1^* w_2^* w_3 w_4 \rangle = \langle w_1^* w_3 \rangle \langle w_2^* w_4 \rangle + \langle w_2^* w_3 \rangle \langle w_1^* w_4 \rangle \quad (2.91)$$

we can rearrange Equation 2.90 to find:

$$\begin{aligned} \langle I_n(x_i, y_i, \lambda) I_n(x'_i, y'_i, \lambda') \rangle &= \langle I_n(x_i, y_i, \lambda) \rangle \langle I_n(x'_i, y'_i, \lambda') \rangle \\ &\quad + |\langle U_n(x_i, y_i, \lambda) U_n^*(x'_i, y'_i, \lambda') \rangle|^2. \end{aligned} \quad (2.92)$$

Next, to calculate the variance of the first-order intensity statistics given by

$$\sigma_I^2(x_i, y_i) = \langle I^2(x_i, y_i) \rangle - \langle I(x_i, y_i) \rangle^2, \quad (2.93)$$

we need to combine Equation 2.93 with Equations 2.85, 2.87 and 2.92. For $x_i = x'_i$ and $y_i = y'_i$ we find:

$$\sigma_I^2(x_i, y_i) = \int_0^\infty \int_0^\infty S(\lambda)S(\lambda') |\langle U_n(x_i, y_i, \lambda)U_n^*(x_i, y_i, \lambda') \rangle|^2 d\lambda d\lambda'. \quad (2.94)$$

Suitable sizes for sample areas are limited by two things: First, the sample area has to be small enough so that the speckle statistics (especially the mean intensity $\langle I \rangle = \mu_I$ and the standard deviation of the intensity σ_I) do not change in this area. Second, the sample area has to be big enough that a good amount of speckles feeds into the statistics. In general, μ_I and σ_I will be dependent on the scanning position x_i, y_i . Using Equations 2.81 and 2.94 to rearrange, leads to

$$\sigma_I^2(x_i, y_i) = \int_0^\infty \int_0^\infty S(\lambda)S(\lambda') \left| \left\langle I_n^{1/2}(\lambda)I_n^{1/2}(\lambda') \exp \{ -i [\phi(\lambda) - \phi(\lambda')] \} \right\rangle \right|^2 d\lambda d\lambda'. \quad (2.95)$$

As U_m and ϕ are independent variables, as long as there are enough scattering events, we can separate the two terms in Equation 2.95

$$\begin{aligned} \sigma_I^2(x_i, y_i) &= \int_0^\infty \int_0^\infty S(\lambda)S(\lambda') \left| \left\langle I_n^{1/2}(\lambda)I_n^{1/2}(\lambda') \right\rangle \right|^2 \\ &\quad \cdot \left| \left\langle \exp \{ -i [\phi(\lambda) - \phi(\lambda')] \} \right\rangle \right|^2 d\lambda d\lambda' \\ &= \int_0^\infty \int_0^\infty S(\lambda)S(\lambda') |\Gamma_U(\lambda, \lambda')|^2 d\lambda d\lambda' \end{aligned} \quad (2.96)$$

and find the normalized auto correlation function of the complex field spectral amplitude given by $\Gamma_U(\lambda, \lambda') = \langle U_n(\lambda)U_n^*(\lambda') \rangle$. For a small bandwidth $S(\lambda)$ the scattering properties are independent of the wavelength λ . Consequently, one can write

$$\langle I_n(\lambda) \rangle = I_0. \quad (2.97)$$

Using this and feeding Equation 2.82 into Equation 2.96 results in

$$\sigma_I^2(x_i, y_i) = I_0^2 \int_0^\infty \int_0^\infty S(\lambda)S(\lambda') \left| \left\langle \exp \left\{ -i2\pi l \left[\frac{1}{\lambda} - \frac{1}{\lambda'} \right] \right\} \right\rangle \right|^2 d\lambda d\lambda'. \quad (2.98)$$

Simplifying the expected value from Equation 2.85 we get the mean intensity as

$$\mu_I = I_0 \int_0^{\infty} S(\lambda) d\lambda. \quad (2.99)$$

Finally, we can calculate the contrast ratio of a speckle pattern:

$$\frac{\sigma_I}{\mu_I}(x_{i0}, y_{i0}) = \frac{\left(\int_0^{\infty} \int_0^{\infty} S(\lambda) S(\lambda') \left| \left\langle \exp \left\{ -i2\pi l \left[\frac{1}{\lambda} - \frac{1}{\lambda'} \right] \right\} \right\rangle \right|^2 d\lambda d\lambda' \right)^{1/2}}{\int_0^{\infty} S(\lambda) d\lambda} \quad (2.100)$$

with the expected value of the exponential phase term given by:

$$\left\langle \exp \left\{ -i2\pi l \left[\frac{1}{\lambda} - \frac{1}{\lambda'} \right] \right\} \right\rangle = \int_0^{\infty} p(l) \exp \left\{ -i2\pi l \left[\frac{1}{\lambda} - \frac{1}{\lambda'} \right] \right\} dl. \quad (2.101)$$

Here, $p(l)$ is the probability density function of the path length. Note, that Equation 2.101 is the Fourier transform of $p(l)$.

With these formulas at hand, we are well equipped to tackle the experimental challenges in Chapter 4 and will be able to check the experimental results by combining simulations (see Section 2.4) and this theory.

2.7 MEASURING COMPLEX FIELDS

In optics usually the intensity of light is the important observable that is measured (see Section 2.1 and Section 2.6). For some applications, a deeper knowledge of the light and its wave nature are desired. For a monochromatic propagating electromagnetic wave, the intensity I is proportional to the square of the absolute value of the complex amplitude of the electric field E :

$$I = \frac{c_0 n \epsilon_0}{2} |E|^2. \quad (2.102)$$

Here, c_0 is the vacuum speed of light, n is the refractive index of the medium and ϵ_0 is the vacuum permittivity. By only taking into account the absolute value of the electric field, all the information of the angular component of the electric field is lost. To recover this complex angular information, which is necessary to predict the interference behavior of coherent light, a special light measurement setup can be used. The basic idea and the principal of operation will be outlined in this section. The measurement setup itself is used in Chapter 5 and will be introduced there in detail related to the actual measurements.

The key idea to obtain the complex field of light is to evoke interference between the “sample”-electric field E_s that has to be examined and another “reference”-electric field E_r that is known. As complex electric fields simply add up, one can write

$$\begin{aligned} I &= \frac{c_0 n \epsilon_0}{2} |E_s + E_r|^2 \\ &= \frac{c_0 n \epsilon_0}{2} \underbrace{\{|E_s|^2 + |E_r|^2\}}_{\text{pure terms}} + \underbrace{2 \{ \Re(E_s) \Re(E_r) + \Im(E_s) \Im(E_r) \}}_{\text{mixed terms}}. \end{aligned} \quad (2.103)$$

If one can separate the mixed term of the two electric fields at the end of Equation 2.103 from the first two terms, one is one step closer to connect the measured intensity to the complex electric field. An extensive mathematical derivation of this procedure can be found in a review article [76]. Here, I will only outline the derivation and focus on the application of this method, as well as its advantages and disadvantages.

By using a tilted plane wave as a reference and applying a Fourier transformation onto Equation 2.103, the centers of the three terms separate in the 2D Fourier plane. The terms $|E_r|^2$ only leads to a sharp peak at $(0, 0)$ in the Fourier plane, as a plane wave has no other contribution. $|E_s|^2$ leads to an intensity spot around $(0, 0)$ with a outer radius that in reality is limited by the numerical aperture (NA) of the detection optics used in an experiment. Only light with angles within the NA can be captured by a microscope objective and hence contribute to the interference. Thus, the maximal angular contribution is two times the NA and only angles

up to the twice the NA can be found in the Fourier plane. The mixed terms in Equation 2.103 lead to a spot around the tilt angle between the reference and the sample wave. This spot is limited by the NA as well. As only interference between the reference and the sample waves contribute to this spot, the maximum angle is just $1\times$ the NA. Real experimental data that graphically show these borders introduced by the NA can be found in Section 5.3 in Figure 5.7.

As this explanation is quite abstract, an artificial sample will be discussed briefly to illustrate the procedure:

Starting with two coherent light beams that interfere with each other on a camera chip with tilt angle of γ depicted in Figure 2.9.

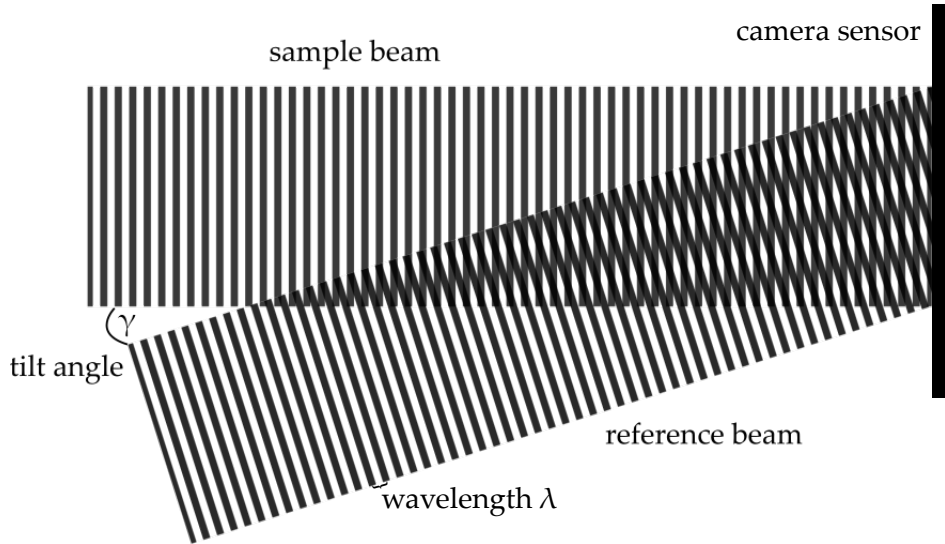


Figure 2.9: Two electromagnetic plane waves interfering on a camera sensor. The reference beam is tilted with respect to the sample beam. Hence there are areas of positive and negative interference on the camera sensor. The tilt angle is connected to the period of the pattern $a = \lambda / \sin \gamma$ with the wavelength λ .

In two dimensions this leads to a striped pattern on the camera chip with the period of the pattern a being connected to the tilt angle γ and the wavelength λ of the light:

$$a = \frac{\lambda}{\sin \gamma}. \quad (2.104)$$

This exemplary striped pattern is depicted in Figure 2.10 in Panel a). By introducing a very simple sample as depicted in Panel b) of the same figure, some light of the sample beam is blocked and hence, this light cannot interfere with the other beam. The resulting “striped A” can be seen in Panel c) of Figure 2.10.

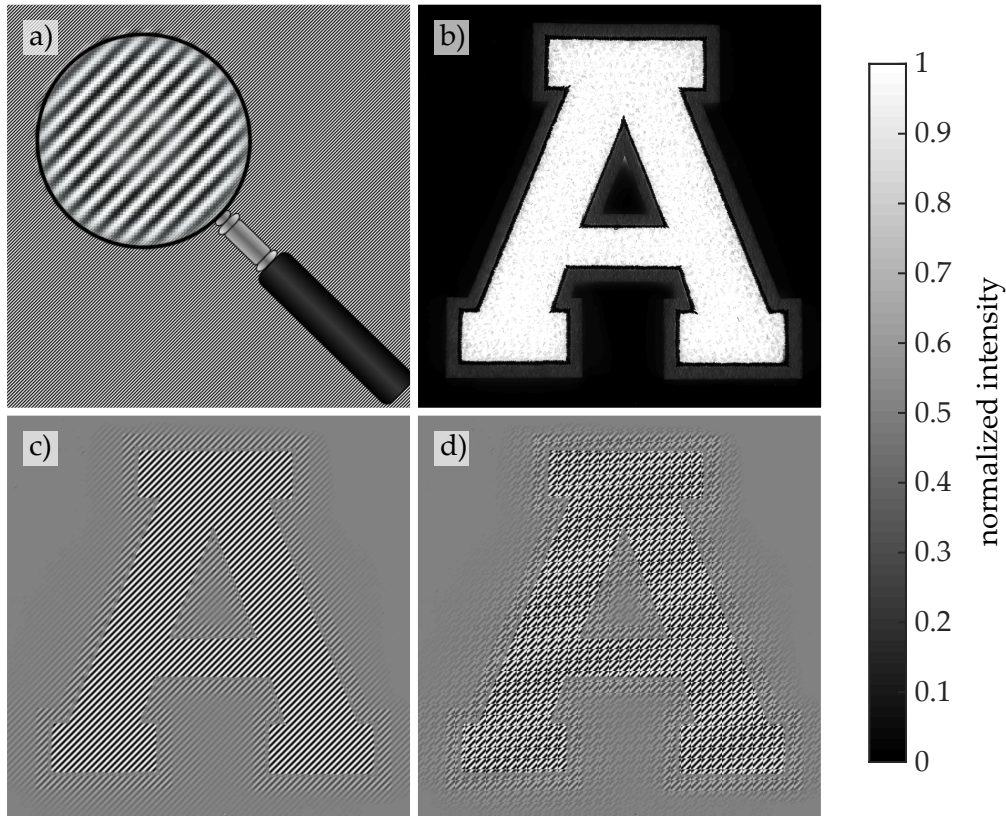


Figure 2.10: Interference pictures. The striped interference pattern of two tilted plane waves emerging under the configuration illustrated in Figure 2.9 is shown in Panel a). Panel b) shows the “A” shaped sample under ambient illumination. The sample is actually an inverted photograph of a felt A in order to have some noise on this picture. Panel c) shows the interference pattern of the reference wave and the sample wave without any phase delay pattern. Diagonal stripes are only visible in the area the sample beam and reference beam contribute to the interference pattern. In Panel d), the phase delay checkerboard pattern (32×32 squares) is added and the diagonal stripes are shifted by $a/2$ for every second area in checkerboard due to the phase delay of π . Note, that for illustration purposes the tilt angle for this figure was lowered by a factor of 4 to increase the visibility of the stripes.

Adding a checkerboard shaped phase delay by half a wavelength in the sample arm would not cause any changes when blocking the reference arm. One would essentially find the pattern illustration in Panel b) again. But with the reference arm the pattern in Panel d) is found, which is easily distinguishable from the one in Panel c). Due to the phase delay in the reference arm, the striped pattern in Panel d) is slightly changed. For the squares that have a delayed phase, the position of bright and dark stripes is shifted. For samples with more random patterns like the speckle patterns that are examined in Chapter 5, the shifting of

the interference stripes does not offer insight into the complex field as easily as this and hence, a more advanced analysis, namely a Fourier transformation gives insight into the phase distribution.

As mentioned in the beginning of this section, the Fourier transformation is an excellent tool to disassemble the intensity pattern into its single contributions. In wave optics, the Fourier transformation can be interpreted as a transformation from position space to angular space. As the interference contributions to the intensity pattern are well separated from the rest of the contributions by the tilt angle, these contributions can be cut out of the Fourier plane.

This is demonstrated in Figure 2.11. The checkerboard-A-sample is illuminated and the picture depicted in Figure 2.10 d) is Fourier transformed by a two dimensional fast Fourier transformation. This results in a complex 2D image in Fourier space. This image is shifted in order to center the $(0,0)$ point in the middle. In Figure 2.11 Panel a), the repetitive checkerboard pattern is clearly visible by evenly spaced dots in the Fourier plane. In addition, the contribution of the “A” to the magnitude of the complex image is clearly visible. Lines emerging from the center of the plane perpendicular to the original corner of the “A” contain the information of the shape of the original letter. In the upper left and the lower right corner this pattern is repeated. Panel b) shows the magnitude of a cutout of the Fourier plane.

This cutout is shifted by exactly the tilt angle from the $(0,0)$ position. Performing an inverse fast Fourier transformation on this complex cutout results in a complex image in position space that has a decreased resolution but contains all complex information. Panel c) of Figure 2.11 shows the magnitude of the recovered image. The shape of the “A” is recovered completely and no diagonal stripes are left. Panel d) shows the angular component of the complex values of the individual pixels. The checkerboard is nicely visible in the area of the “A” and the phase shift between the two areas is π as expected. The algorithm tries to find a complex angle for all areas in the picture and thus, the outer area is filled with noisy angular information.

The measurement procedure outlined in this section is used in Chapter 5 in order to reconstruct the complex electric field of speckle patterns that evolve when scattering samples are illuminated by coherent light.

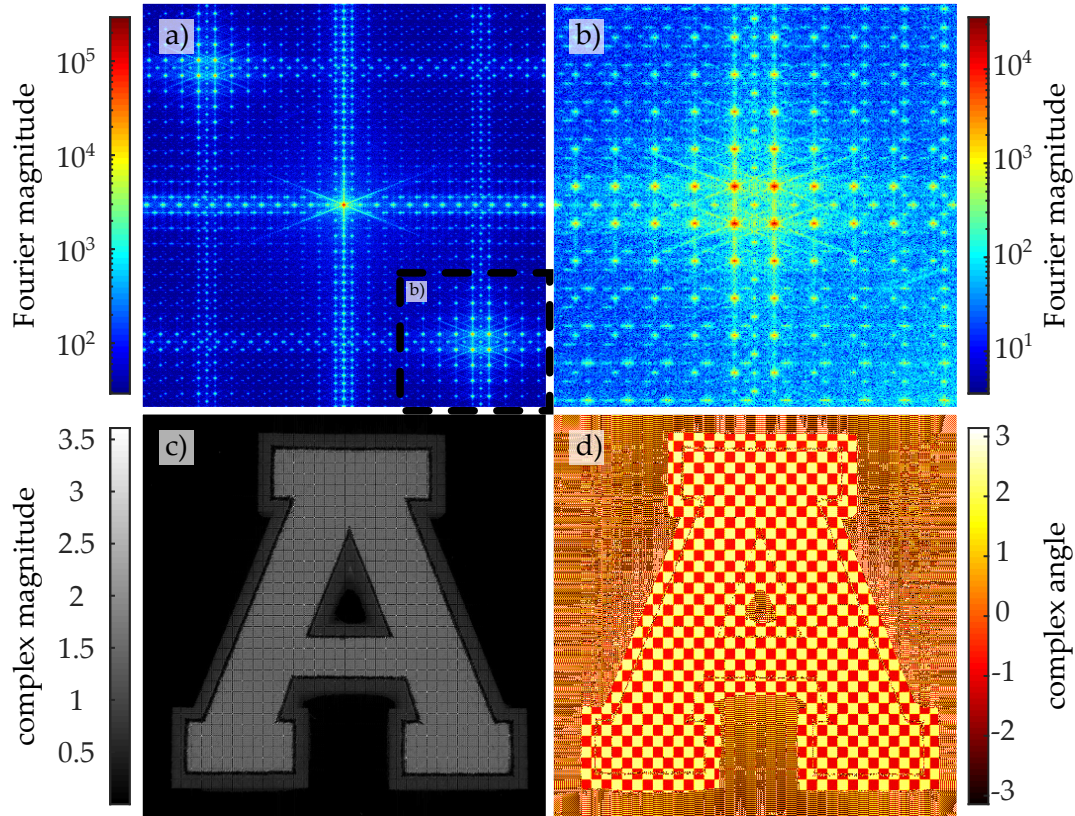


Figure 2.11: Interference evaluation. Panel a) shows the Fourier transformation of the picture shown in Panel d) of Figure 2.10. The Fourier plane is shifted to center the $(0,0)$ point in the middle. The two individual contributions to the pattern shown are quite good distinguishable: the diagonal lines correspond to the contours in the “A” that are perpendicular to said lines. The evenly distributed dots correspond to the borders between the checkerboard squares. Note that as this is only simulated data, no boundary due to the effective NA is visible. Panel b) shows the cutout of the lower right corner of Panel a) indicated by the black dashed lines. In this panel one can clearly see the diagonal lines that correspond to the letter shaped sample. An inverse Fourier transformation of the data shown in Panel b) leads to a complex picture that is shown in the lower panels. Panel c) shows the magnitude of the reconstructed picture. Expect for a couple of artifacts that origin in the infinite NA of this simulation, the original “A” shape is reconstructed. In addition to this, Panel d) reveals the phase shifting checkerboard pattern, that was hidden under normal illumination shown in Figure 2.10 Panel d).

3

Chapter 3

LIMITS OF LAMINATES IN DIFFUSE-LIGHT

Laminates are an intuitive way to manipulate the propagation of light in the context of the diffusion equation. They enable a straightforward way to introduce anisotropic material parameters to an otherwise isotropic medium. Laminates are a well-known concept in other fields of physics as well. In heat conduction, electrical conduction, electrostatics, and magnetostatics laminates are an often-used tool to achieve desired anisotropic properties. In diffuse-light propagation, laminates enable the possibility to realize anisotropic diffusivity tensors (see Section 2.3.3) and thus, they seem to offer the easiest way to guide light around an object. But in contrast to heat conduction [28, 29] or electric conduction [21] the boundary conditions in diffuse optics are different: To design and to present a cloak for diffuse-light, one has to present it in a non-diffusive surrounding. This situation would compare to presenting a cloak for electric conduction embedded in a superconductor. To make the effect of the diffuse-light cloak visible, one has to increase the transmission of the cloaking device as far as possible to obtain respectable results. But by increasing the transmission one runs into problems with the approximation of the diffusion equation.

In this chapter, we will investigate the transition from diffuse to ballistic-light transport and the performance of laminate structures in the respective regime of light transport.

To access the region of light scattering that lies in between the diffusive regime and the ballistic regime, we used a Monte Carlo based ray tracing software (FRODO) (see Section 2.4) that was developed by R. Schittny and F. Mayer in 2015 [40].

In the following sections, the layout of the simulation setup will be explained and the results of these simulations and their significance to the design for past and future invisibility cloaks in the diffuse-light regime will be discussed. This chapter is based on a paper [77] that was published in the context of a master thesis I supervised in 2018. In her thesis [42], S. Mannherz investigated the behavior of laminate structures in the context of an advanced cloaking design by B. Orazbayev

et al. [60].

3.1 INTRODUCTION

Until now, most architectures of invisibility cloaks for diffuse-light have been rather simple with piecewise homogeneous sections in terms of the diffusivity \vec{D} [30, 39, 40]. More advanced designs for diffuse-light devices usually require anisotropic material parameters just as in other fields of physics [26, 60, 78, 79]. To realize an anisotropic tensor \vec{D} for diffuse-light propagation, dual laminate structures are the easiest solution. Stacked layers of alternating material A and B with corresponding diffusivities $D_A \neq D_B$ form a laminate structure. This stack allows for light propagation within the direction of the layers that is dominated by the scattering properties of the constituent material that has the higher diffusivity. Perpendicular to the planes, light propagation is dominated by the material with the lower diffusivity.

To bring this easy concept to perfection, the laminate thickness of laminate A and B should be as small as possible to homogenize the resulting light propagation. Consequently, laminates should be infinitesimal thin. For real life applications, this is not only impractical, but also either leads to vanishing transmission of the sample or the anisotropy effect of the laminate structure vanishes. This depends on the amount of scattering one introduces: Either one increases the amount of scattering in the laminates to stay within the diffusion approximation (see Section 2.1.6.3) but loses transmission or one holds on to a fixed transmission, thus does not increase the amount of scattering particles. This leads to a violation of the approximation of the diffusion equation and in the end (with very fine laminates) leads to the complete loss of the anisotropy effect of the laminates.

To investigate this transition from diffuse-light propagation to ballistic-light propagation, we will use a Monte Carlo ray tracing software (FRODO, see Section 2.4). This software does not assume any of the violated diffuse-light approximations, but simulates the scattering of the photons according to the radiative transfer equation (see Equation 2.1.6.1). Hence the transition from diffuse-light to ballistic-light can be covered within one simulation setup.

Note, that this kind of simulation does not take into account effects that originate from the wave nature of light. Interference or localization cannot be simulated with the software used. Simulating these effects, one would have to do a full wave simulation following Maxwell's equations, but simulations like these for big, complex samples are way out of reach for the computing power that is available to us.

3.2 EXPERIMENTAL SETUP

The basic idea to measure the performance of laminates is to illuminate an AB-laminate structure on the back side (that means parallel to the laminate layers, see Figure 3.1). Following diffusion theory, this point illumination will spread through the laminate and the light that will exit the laminate structure on the front side will form a spot with an elliptical intensity shape. The ellipticity is connected to the ratio of the diffusivities of the constituent laminate layers.

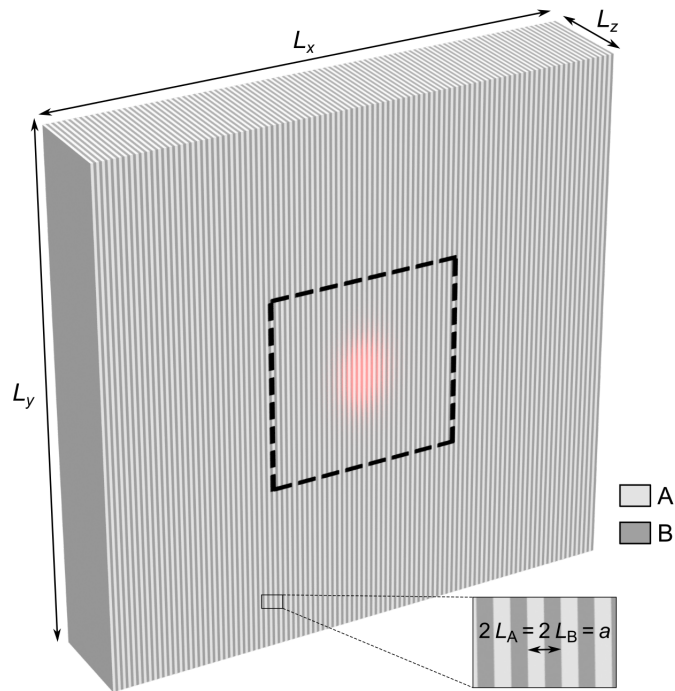


Figure 3.1: Sample to investigate laminate performance. The dimensions are $L_y = L_x = 8L_z$. 100 layers of AB-laminate are stacked in z -direction. Photons are started from the center of the back side. The marked area with black dashed lines is shown in Figure 3.2. Figure adapted from [77].

To achieve a maximal effect, the thickness of laminate A and laminate B are the same: $L_A = L_B = a/2$ with a the laminate period [14, 53]. As explained in more detail in Section 2.2 the diffusivity tensor in laminates is

$$\overleftrightarrow{D} = \begin{pmatrix} D_{xx} & 0 & 0 \\ 0 & D_{yy} & 0 \\ 0 & 0 & D_{zz} \end{pmatrix}. \quad (3.1)$$

For the orientation in Figure 3.1, the effective diffusivities for each direction are

$$D_{yy} = D_{zz} = \frac{D_A + D_B}{2} \quad (3.2)$$

for the two directions in plane with the laminates. The diffusivity in the direction perpendicular to the planes is given by

$$\frac{1}{D_{xx}} = \frac{1}{2} \left(\frac{1}{D_A} + \frac{1}{D_B} \right). \quad (3.3)$$

Defining the ratio of the constituent diffusivities as $D_A/D_B = s$, the ratio of effective diffusivities becomes:

$$\frac{D_{yy}}{D_{xx}} = \frac{(1+s)^2}{4s}. \quad (3.4)$$

During the simulation, we will fix the ratio of D_A and D_B to $s = 10$ (and change it later to $s = 25$ and $s = 5$ in additional simulations). This ratio of constituent material parameters leads to the following ratios of the effective parameters.

s	10	25	5	(3.5)
$\frac{D_{yy}}{D_{xx}}$	3.025	6.76	1.8	

Note that this description does not take into account any finite size individual laminate layers.

In the following several length scales will be discussed. Hence, a short mentioning of the important length scales is suitable. For a more detailed introduction into the individual scattering length scales read Section 2.1.

- l_t : The transport mean free path length is connected directly to the diffusivity via the energy velocity of light in the medium: $D = \frac{1}{3}v_e l_t$.
- l_s : On the one hand, the scattering mean free path length is connected to the transport mean free path length via the anisotropy g of the individual scattering events: $l_t = l_s \frac{1}{1-g}$. On the other hand, it is connected to the density of scatterers n_s and the scattering cross section c_s via $l_s = \frac{1}{c_s n_s}$.
- l_D : The diffusion length is the average path length a photon travels through a scattering medium before it is absorbed. As we do not take into account absorption in our simulation we get: $l_D = \infty$.
- a : The laminate period defined by the layer thicknesses. The thicknesses L_A and L_B of the two individual laminate layers A and B ($L_A = L_B$) add up to the laminate period: $a = L_A + L_B$.

- L_j : The outer dimensions shown in Figure 3.1. These dimensions have to be chosen carefully in order to minimize light leakage to the sides as well as computation time and to maximize the quality of the measured data.

With all these length scales in hand, the restrictions that lead to a “good laminate” and hence to an effective medium, can be discussed. In terms of the diffusion equation there are two restrictions: The laminate layers have to be thin in respect to the spot size of the transmitted light. This leads to a smooth distribution of the transmitted light intensity. Choosing the outer dimensions of the laminate device to contain the complete spot size, we end up with $L/a \gg 1$. The second restriction is that the diffusion length has to be a lot longer than the thickness of the laminates: $l_D/a \gg 1$. In our simulation with $l_D = \infty$ the second restriction is always fulfilled.

In terms of the diffusion equation, there are no more restrictions for a laminate to perform perfectly. But of course, the restrictions for the diffusion approximation have to be met as well. In general, these restrictions were introduced in Section 2.1. Translated to the laminate structure, the remaining restriction reads as: $l_t/a \ll 1$. In diffuse-light propagation, light has to be scattered several times before it exits a medium. As laminate A and B have different scattering properties, they count as different media in this sense. Consequently, the transport mean free path length has to be short enough to allow a couple of scattering events in both, material A and B before the photons have a chance to change the laminate.

So far, there are no contradictions in this line of restrictions: $L \gg a \gg l_t$. This has to hold true for all l_t , hence in laminate A and in laminate B. The only problem is, that fulfilling these restrictions leads to very small laminate layers and to even smaller transport mean free path lengths. These strongly scattering laminates will have a very low transmission, as the transmission of a material decreases with stronger scattering or shorter transport mean free path length. As a consequence, one has to find a compromise between a good laminate with $l_t \ll a$ and a vanishingly low transmission and a violation of the restrictions of the laminate or the diffusion equation to get a decent transmission on the cost of performance of the laminate.

One might ask why there is no such problem in the fields of physics mentioned above like particle diffusion or heat conduction. As the mathematics behind these physics is almost the same, the same problems have to be faced here as well. But in contrast to light diffusion, the transport mean free path length in particle diffusion in the case of molecules diffusing in ambient conditions in air is on the order of some tens of nanometers. The same holds true for electrons diffusing in ordinary metal at room temperature. In contrast to these very short wavelengths, the transport mean free path length in light diffusion, for us, is in the range from several micrometers to some millimeters. Due to this difference in l_t of at least some orders of magnitude, the problem discussed in this chapter is far more

relevant to light diffusion than to other diffusion like processes. Of course, the same problems will arise in other fields of physics for the same ratios of sample size to transport mean free path length L/l_t , hence for laminates with a total size in the micrometer range.

To connect the shape of the transmitted light spot to the effective diffusivities D_{xx} and D_{yy} in the laminate, we will have a short look at an isotropic medium with diffusivity D once again. The mean square displacement $\sigma = \sigma_x = \sigma_y = \sigma_z$ of a random walk in 3D is [46]

$$\sigma^2 = Dt \quad (3.6)$$

with the diffusion time t .

As a reminder, one can try to arrange this equation in the form of $s = v \cdot t$ to find something like a velocity for the spread of photons in a diffusion process. But this leads to $\sigma = \sqrt{D} \cdot \sqrt{t}$ and one sees, that the displacement of light is proportional to the square root of the time and hence the expansion of diffusion processes seems to slow down in time. Using the proportionality of the diffusivity to the square of the mean square displacement will be the main idea to evaluate the performance of laminates in Section 3.4.

Looking at the ratios between two effective diffusivities into different directions (D_{xx} and D_{yy}) in the laminate leads to a form without any time dependence.

$$\frac{\sigma_y^2}{\sigma_x^2} = \frac{D_{yy}}{D_{xx}} \quad (3.7)$$

A alternative way to find this connection without using time dependence is using the diffusion equation (Equation 2.47) and a simple spatial coordinate transformation as shown in Section 2.3.3. For a transformation $(x, y, z) \rightarrow (x', y', z') = (fx, y, z)$ with the stretching factor f , one can apply this for the mean squared displacement like: $(\sigma_x, \sigma_y, \sigma_z) \rightarrow (\sigma'_x, \sigma'_y, \sigma'_z) = (f\sigma_x, \sigma_y, \sigma_z)$. In contrast to this, the diffusivity transforms like: $(D_{xx}, D_{yy}, D_{zz}) \rightarrow (D'_{xx}, D'_{yy}, D'_{zz}) = (f^2D_{xx}, D_{yy}, D_{zz})$. The square in the second transformation originates from the fact, that there is a second-order derivative with respect to space in the diffusion equation. So once again, we find $\frac{\sigma_y^2}{\sigma_x^2} = \frac{D_{yy}}{D_{xx}}$.

3.3 MONTE CARLO SIMULATIONS

After introducing the Monte Carlo method for ray tracing in light-scattering media in Section 2.4, some specific settings that apply to the experimental simulation in this chapter and some features that are important in this context will be discussed here.

A vital feature that will be used in the simulations ahead is the possibility to simulate not only diffuse-light conditions but also to reproduce the behavior of ballistic-light propagation. Due to that, the algorithm can not only handle a wide span of scattering coefficients but also accounts for Fresnel reflections, refraction and other ballistic-light effects. Another feature that is stressed in the following kind of simulation a lot, is the ability to change precalculated path lengths on the fly if the photon hits the interface between laminate A and B. Intersection positions of light paths and edges of light-scattering media are calculated in a fast manner, as only simple geometries are allowed. When hitting the surface of a laminate, the path length that is left will be changed according to the scattering coefficient in the new medium and the direction will be updated according to Fresnel reflections.

On the one hand, an obvious downside of the Monte Carlo method is the fact that photons may not be propagated backwards because the randomness of the individual scattering processes breaks symmetry of light paths. Hence, under diffuse conditions, most of the simulated photons will not exit the medium on the detection side and will be lost. As the transmission goes down to about 0.1%, one has to simulate 1000 times more photons to get the same statistical uncertainty as for ballistic conditions.

On the other hand, one has to emphasize again why a Monte Carlo ray tracer is the best kind of simulation solution for our experiment: By not defining the material with all its scattering particles and their locations, a huge amount of data, that otherwise had to be saved somewhere, does not have to be stored. In a ray tracing simulation with well-defined scattering centers or in a real live experiment, the number of scattering particles would be in the order of 10^{18} (for the lowest l_t/a in Figure 3.7). As the information for every of these randomly distributed scattering particles has to be accessible very fast, this would impose a big problem for data storage. This trouble is circumvented by not defining the position of the scatterers but rather using the Monte Carlo method.

3.4 SIMULATION RESULTS

Choosing the optimal geometry for the laminate device is crucial for efficient simulation times and good statistics for the results. As we want to investigate the impact of coarser and finer laminates on the performance of laminate structures, one might think that a fixed simulation geometry might not do the job. But as mentioned, there are no fixed spatial scales in the simulation.

Hence, tuning the ratio l_t/a does just what we want. One can either read this as: We fix the geometry with the number of laminate layers and its sizes and tune the scattering coefficient from a high amount of scattering (low l_t/a) to a small amount of scattering (high l_t/a) in order to stress the diffusion equation

approximation. Or one can read that as: We fix the mean free path length of the constituent materials and tune the geometry from very coarse laminates (huge a corresponds to low l_t/a) to very fine laminates (small a corresponds to high l_t/a).

To minimize light leakage to the sides of the laminate structure, the device has to be rather big in x and y -direction. We chose a ratio of $L_x = L_y = 8L_z$ in order to lower the losses and still have a reasonable number of bright laminate layers on the front side with a finite overall number of laminate layers. The ratio between L_x and a also has to be discussed: The more laminate layers we simulate, the smaller the errors due to the overlaid laminate structure will be in the analysis afterwards. But the more layers we simulate, the more time it will take to compute these simulations. We found 100 periods to suit our needs and still have reasonable simulation times and thus: $L_A + L_B = a = L_x/100$. To investigate laminate structures that are also possible to fabricate, we chose the ratio of the transport mean free path length to be $l_t^A/l_t^B = 10$ for our first group of measurements and then repeated these simulations for a ratio of 25 and 5. These ratios can also be interpreted as the inverse ratio of the number of scattering particles, as $l_t \propto l_s \propto 1/N_p$.

In the following, we will perform several groups of simulations: In order to investigate one set of fixed l_t^A/l_t^B parameters, we will vary l_t^A/a from 10^3 to about $4 \cdot 10^{-2}$ in a logarithmic manner to grasp a large variety of ratios with 23 individual simulations.

The laminate device is illuminated by a quasi point source located in the middle of the back side of the sample. It has an isotropic emission which results in half the photons to never enter the laminate structure. This loss of 50% is accounted for in the transmission calculated below. It is only a quasi point source because putting the light source exactly in the middle of the laminate would lead to numerical problems, as there is an interface between two laminate layers A and B at the intended position of the point source. To circumvent this problem, we implemented a dual illumination: half of the light is emitted at a position $x = x_0 + 0.01a$ and the other half is emitted at $x = x_0 - 0.01a$. For most of our simulations we chose $n = 1.0$ as the light yield will slightly change for a higher refractive index.

For diffuse-light, the chosen ratio of l_t^A/l_t^B can be translated to a ratio in diffusivities:

$$\frac{l_t^A}{l_t^B} = \frac{D_A}{D_B} = 10. \quad (3.8)$$

Following diffusion theory, the result of a point-like source on the back side of a structure (see Figures 3.2 and 3.3) should be a spot of transmitted light on the front side with an elliptical shape. As the effective diffusivity in y -direction is higher than in x -direction, the spot should be more elongated in the y -direction than in the x -direction.

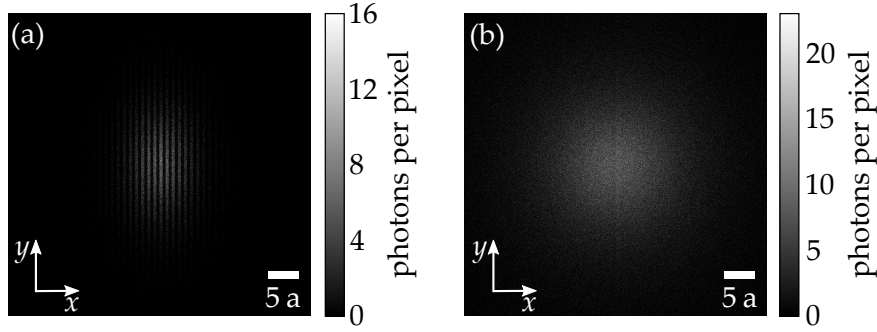


Figure 3.2: Simulated transmission pictures. Intensity plots of the transmission through the sample shown in Figure 3.1 and simulated by Monte Carlo ray tracing are shown. Only the center region of the front side is shown here, indicated by a black dashed line in Figure 3.1. The transport mean free path lengths of the constituent materials have a ratio of $l_t^A/l_t^B = 10$. Diffusion theory predicts an effective ratio of $D_{yy}/D_{xx} = \sigma_y^2/\sigma_x^2 \approx 3$. Panel a) shows the transmission for a ratio $l_t^A/a \approx 0.25$, which leads to the effectively anisotropic behavior that is expected within the regime of diffuse-light propagation. The elongation of the light spot in y -direction is clearly bigger than in x -direction. The individual laminate structure is visible as light tends to exit through the laminates that have a larger mean free path length. For $l_t^A/a = 1000$, the light-diffusion approximation is no longer valid. As a result, due to ballistic-light propagation through the sample, an isotropic intensity pattern is observed on the front side of the sample, depicted in Panel b). Individual laminate layers are not visible. Note, the amount of simulated photons that lead to these results was about ten times higher for the simulation shown in Panel a) than for the simulation shown in Panel b). These simulations are part of a group of simulations that leads to Figure 3.6. There, correspondent data points are indicated by blue circles. Figure adapted from [77].

In Figure 3.2 a region of interest of the light intensity on the front surface of the simulated laminate sample is shown. The laminate sample (shown in Figure 3.1) is illuminated with a point source on the back side. The left Panel a) shows diffusion-like scattering conditions: with $l_t^A/a = 0.25$ the transport mean free path length is a little bit smaller than the thickness of one laminate in the less scattering laminate A. For laminate B with $l_t^B/a = 0.025$, the scattering is well in the diffusive regime.

As expected, the transmitted light spot on the surface has an elliptical shape, more elongated in the y -direction. In addition to the elliptical shape, one can see a vertical striped pattern with the periodicity of a . As the laminate B is more strongly scattering, less photons exit the laminate structure out of the B laminate than out of the A laminate.

Panel b) shows the exit positions for the simulated photon propagation for a laminate structure that is barely scattering. Just like in Panel a) it only depicts a

region of interest of the front side of the laminate structure indicated by a black dashed line shown in Figure 3.1. In contrast to Panel a), the ratio $l_t^A/a = 1000$ is about 4000 times higher. As a consequence, there is barely scattering in laminate A and almost no scattering as well in laminate B. Hence, the laminate orientation has no influence on the light distribution and the light propagation appears to be isotropic.

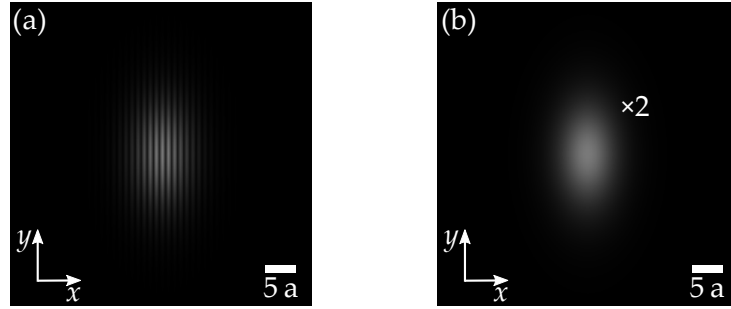


Figure 3.3: Numerical solutions of the diffusion equation for the photon density obtained by Comsol Multiphysics for comparison to Figure 3.2. Panel a) shows the photon density for the transmission through a laminate structure with $D_A/D_B = 10$. Note, that the ratio l_t^A/a is not of interest here, as we assume the diffusion description to be valid in the first place. As a result, the shape of the transmitted light spot is independent from l_t^A/a . Panel b) shows the photon density on the front side of a cuboid with an anisotropic diffusivity Tensor \vec{D} . Anisotropy ratio is just the same as for Panel a): $D_{yy}/D_{xx} \approx 3$. To compare the brightness of Panel a) and b), note that Panel b) is displayed two times brighter. Figure adapted from [77].

To compare the results depicted in Figure 3.2 to the light distribution predicted by the diffusion equation, simulations base in the diffusion equation are presented in Figure 3.3. Herein, the diffusion equation was solved using Comsol Multiphysics. The similarity between Panel a) in Figure 3.2 and Panel a) in Figure 3.3 indicates that the corresponding Monte Carlo simulations in Panel a) of Figure 3.2 were in the diffusive regime as well. In Panel b) of Figure 3.3 instead of a laminate structure a homogeneous material with anisotropic diffusivity is simulated. To compare the shapes of the transmitted spots, the brightness of the image in Panel b) has been increased by a factor of 2.

3.4.1 Measuring the Ellipticity

To quantify the observation done with the bare eye in Figure 3.2, we have a closer look at the intensity $I(x, y)$ of light on the front side of the laminate structure. Its shape is in general continuous and thus, its mean squared displacement in

x -direction is calculated as

$$\sigma_x = \sqrt{\frac{\int I(x, y)(x - \bar{x})^2 dx dy}{\int I(x, y) dx dy}}, \quad (3.9)$$

and the same holds true for the y -direction:

$$\sigma_y = \sqrt{\frac{\int I(x, y)(y - \bar{y})^2 dx dy}{\int I(x, y) dx dy}}. \quad (3.10)$$

But as the Monte Carlo simulation simulates discrete photons and thus discrete exit positions, in our case, the integrals become sums and the mean squared displacements in x and y -direction read:

$$\sigma_x \approx \sqrt{\frac{\sum_{i=1}^{N_t} (x_i - \bar{x})^2}{N_t}} \quad (3.11)$$

and

$$\sigma_y \approx \sqrt{\frac{\sum_{i=1}^{N_t} (y_i - \bar{y})^2}{N_t}}. \quad (3.12)$$

With discrete exit positions, the mean squared displacement will always have an statistical error, as there are N photons and thus N photon positions to sum up to get the mean squared displacement.

To get the mean exit position, we evaluate

$$\bar{x} = \frac{1}{N_t} \sum_{i=1}^{N_t} x_i \quad (3.13)$$

and

$$\bar{y} = \frac{1}{N_t} \sum_{i=1}^{N_t} y_i. \quad (3.14)$$

Using these sums to calculate the ratio σ_y^2/σ_x^2 for small l_t^Λ/a gives us, within statistical accuracy, the expected values for D_{yy}/D_{xx} already calculated in Equation 3.5. This agreement approves our choice of dimensions and measures (see Figures 3.2 and 3.3). Hence, the laminate structure shown in Figure 3.1 is a good choice to investigate laminate performance in the diffusive regime.

Tuning the material parameters from diffuse-light propagation to ballistic-light propagation, we run into a mathematical problem: The shape of the spot on the front side of the sample changes from a Gaussian ellipse to a Lorentzian (also called Cauchy) round spot. Defining a mean squared displacement for this kind of distribution is problematic: The Lorentzian distribution has heavy tails and thus

the standard deviation is only defined for a finite interval. As a result, the standard deviation depends on the chosen interval. As we are inspecting the square front side of our laminate sample, the intervals in x and in y -direction are fixed and they are the same. Therefore, the factor that depends on the chosen interval, should drop out as soon as we look at the ratio σ_y/σ_x . For most of our simulations, we will be looking at a mixture of Gaussian and Lorentzian distributions and the ratio of the influence of these to extreme cases might even be different in x and in y -direction. To stay on the safe side, we look for a measure of the anisotropy of the laminate device that is well-defined in both, the diffusive and the ballistic regime. Using the full width half maximum (FWHM) to quantify the width of the ellipse seems to be an easy way to solve the problem. Unfortunately, without any curve fitting, this method would be very noisy. However, curve fitting is not an option, as the mix of Gaussian and Lorentzian distribution does not give us a model to fit to.

Instead of the mean squared displacement, we introduce an alternative measure w to quantify the anisotropy of the transmitted light spot, the square of the mean square root of the absolute values of x and y .

$$w_x = \left(\frac{\int I(x, y) \sqrt{|x - \bar{x}|} dx dy}{\int I(x, y) dx dy} \right)^2 \quad (3.15)$$

$$w_y = \left(\frac{\int I(x, y) \sqrt{|y - \bar{y}|} dx dy}{\int I(x, y) dx dy} \right)^2 \quad (3.16)$$

This measure can be translated into a form of sums as well and then reads as

$$w_x \approx \left(\frac{\sum_{i=1}^{N_t} \sqrt{x_i - \bar{x}}}{N_t} \right)^2 \quad (3.17)$$

$$w_y \approx \left(\frac{\sum_{i=1}^{N_t} \sqrt{y_i - \bar{y}}}{N_t} \right)^2. \quad (3.18)$$

As shown in the fundamentals Chapter 2.5.6, this measure is well-defined for both, Gaussian and Lorentzian distributions. For Gaussian distributions, the two measures w and σ are proportional: $w_{x,y} = \frac{\sqrt{2}}{\pi} \Gamma(3/4)^2 \sigma_{x,y} \approx 0.676 \sigma_{x,y}$. The proportionality factor drops out as soon as we look at ratios and thus we have:

$$\frac{w_y^2}{w_x^2} = \frac{\sigma_y^2}{\sigma_x^2}. \quad (3.19)$$

For Lorentzian profiles, we get $w = 2\gamma$, where 2γ is the FWHM of the Lorentz distribution. As w takes exit positions that are far away from the middle not as

much into account as σ , statistical errors will be different for these two measures. We noticed a small systematical difference that occurs due to these statistical differences for noisy data and results in $w_y^2/w_x^2 > \sigma_y^2/\sigma_x^2$ for Lorentzian profiles. For Gaussian profiles, $w_y^2/w_x^2 = D_{yy}/D_{xx} = \sigma_y^2/\sigma_x^2$ holds true. With the square of the mean square root w we found a measure that is well-defined and we can faithfully derive the shape of the transmitted light spots on our laminate sample.

To give an overview over the simulations presented within the next pages, all simulations with their key parameters are listed in the table below.

	Section	Laminate Contrast	Anisotropy	Refractive Index	Keyword
#1	3.4.2	$l_t^A/l_t^B = 10$	$g = 0$	$n = 1$	realistical contrast ratio
#2	3.4.3	$l_t^A/l_t^B = 25$	$g = 0$	$n = 1$	high contrast
#3	3.4.4	$l_t^A/l_t^B = 5$	$g = 0$	$n = 1$	low contrast
#4	3.4.5	$l_t^A/l_t^B = 10$	$g = 0.5$	$n = 1$	more forward scattering
#5	3.4.6	$l_t^A/l_t^B = 10$	$g = 0$	$n = 1.4$	realistic refractive index

3.4.2 Results for Realistically Manufacturable Laminate Contrast

Figure 3.4 graphically shows the evaluation of the data contained in Figure 3.2 with some additional information (fit curves) for clarity. The main plot shows two histograms: In red, the x -component of the exit position of every photon is binned in order to get a histogram that shows the distribution of photons in x -direction. In blue, the same is done for the y -coordinate of the exit positions. Both histograms are fitted to a Gaussian distribution that is plotted onto the data in dashed line in the corresponding color. The agreement of the simulated data and the fitted curve is quite good in y -direction. In x -direction the laminates pose a modulation onto the expected Gaussian distribution. The fitted curve seems to be lying just in the middle of the high and low points of the data.

Figure 3.5 gives an insight into the light distribution of Panel b) of Figure 3.2. As in Figure 3.4, the individual x - and y -components of the exit positions of the transmitted photons are analyzed separately in two histograms. The data was simulated using $l_t^A/a = 1000$. That corresponds to a very low probability of scattering.

In contrast to Figure 3.4, there is no anisotropy visible. The only difference between the red curve (x -direction) and the blue curve (y -direction) is a small deviation of the red curve in the center. This can be explained within some short steps: $l_t^A/a = 1000$ is equal to $l_t^B/a = 100$. Having a look at the overall dimensions: $100a = L_x = 8L_z \rightarrow a = L_z/12.5$. Combining these two thoughts

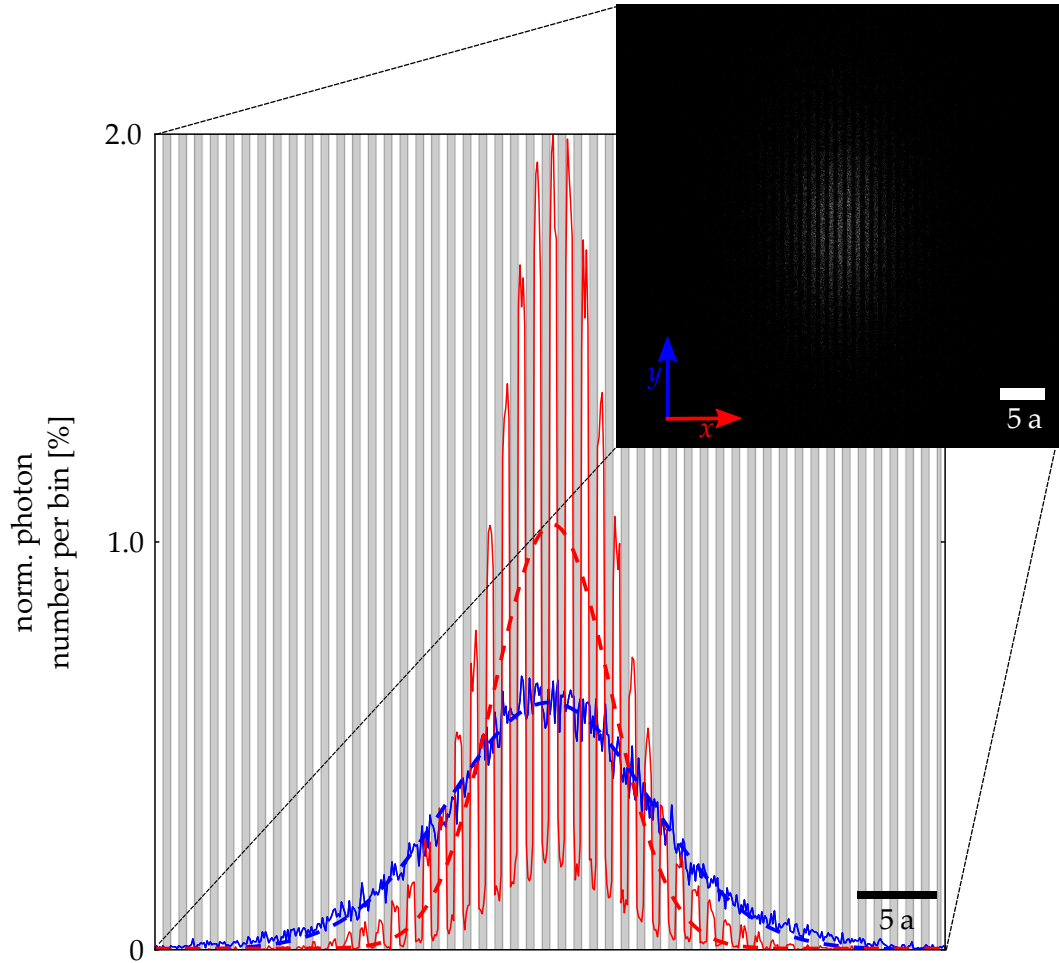


Figure 3.4: Evaluation of the diffuse-light simulation shown in Figure 3.2 Panel a) (once again depicted in the upper right corner). On the vertical axis, the normalized photon number per bin is displayed, and on the horizontal axis, the x -coordinate (red) and the y -coordinate (blue) is displayed. In red, the x -coordinates of the individual exit positions of the photons are displayed in form of a histogram (solid line). The red dashed line shows a Gaussian fit to the data. In the background, the individual laminate layers are displayed (only applicable for the x -direction in red). In blue, the y -coordinates of the exit positions of the simulated photons are displayed as a histogram. The blue dashed line is a Gaussian fitted to the data. Note the different width of the curves, the dashed blue and the dashed red line indicate. Figure adapted from [42].

gives $l_t^B = 8L_z$. This might give an intuitive understanding why there is a dip of about 8% for the B laminate layer in the center. Light that is emitted in parallel the laminate layer has a higher chance to be scattered and most of it is scattered into the neighboring laminate layer A. Except for this little wiggle in the center, both,

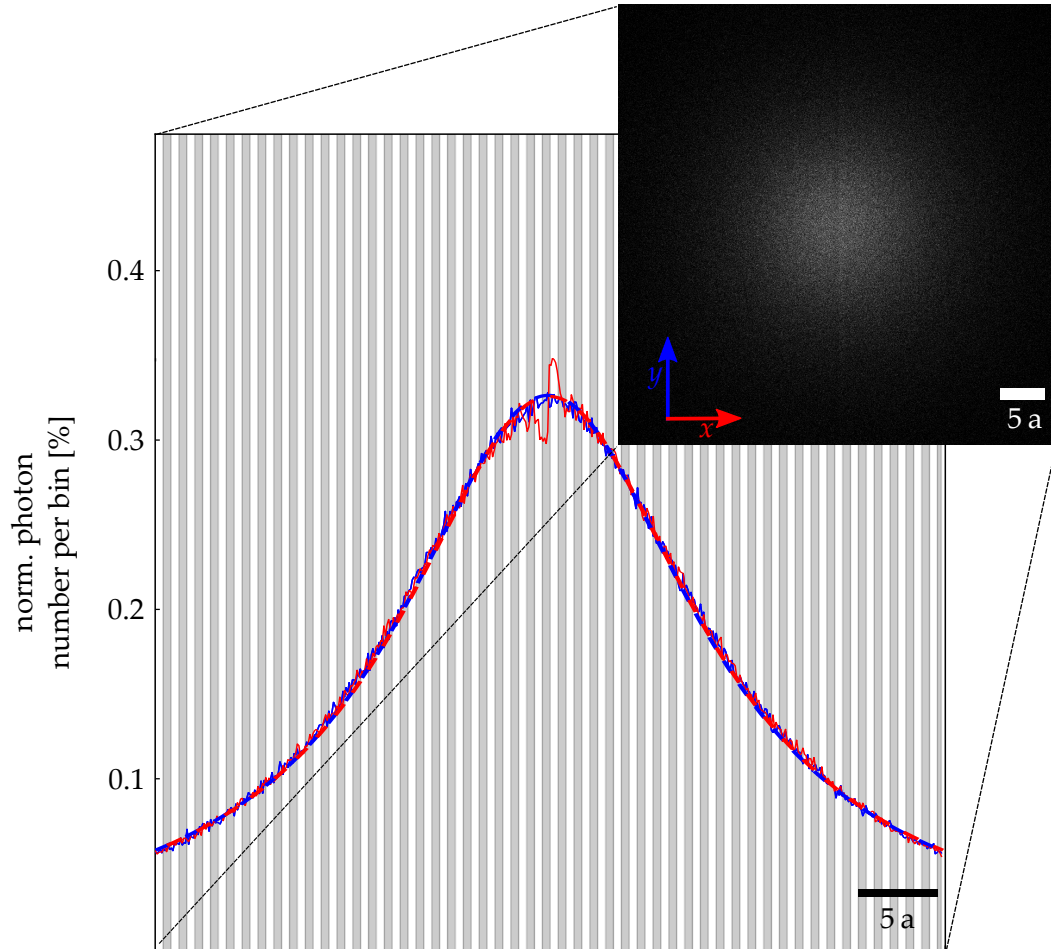


Figure 3.5: Evaluation of the ballistic-light simulation shown in Figure 3.2 Panel b) (once again depicted in the upper right corner). The axis are the same as in Figure 3.4. In red, the x -coordinates of the photons are displayed in form of a histogram (solid line). In blue, the y -coordinates are displayed. The dashed lines are Lorentzian fits to the data. The ratio of $l_t^A/a = 1000$ leads to almost no scattering and thus a perfect Lorentzian shape of the transmission. The only influence of scattering one can see clearly is a small deviation from the Lorentz curve in x -direction in the middle. For high l_t^A/a the Lorentzian model seems to describe the photon distribution quite well. Figure adapted from [42].

x - and y -components of the exit positions form a perfect Lorentzian distribution. That fits are shown in blue and red dashed lines on the sample data in Figure 3.5.

Please note that these models were fitted only for visualization purposes. In the following analysis, the width of these curves are not pure Gaussian or Lorentzian distributions but rather a mixture of these two and thus the calculation of the width in x and y -direction from Equations 3.11, 3.12, 3.17, and 3.18 is a great

advantage over fitting the results to the data.

In Figure 3.6 results of 23 individual simulations are presented. The vertical axis of the upper panel indicates the ratio of the two measures that were introduced before: σ_y^2/σ_x^2 and w_y^2/w_x^2 . They both are a measure for the shape of the transmitted light spot and thus a measure for the performance of the laminate. The full dots relate to the ordinary measure σ_y^2/σ_x^2 and the position of the circles indicates the ratio of the newly defined measure w_y^2/w_x^2 . The dashed line indicates the expected value for σ_y^2/σ_x^2 and w_y^2/w_x^2 following diffusion theory. On the horizontal axis, the simulation parameters $l_t^{A,B}/a$ are indicated. On the lower horizontal axis l_t^A/a gives the ratio between the transport mean free path length in the less scattering laminate material A l_t^A and the laminate period a . Additionally, on the upper horizontal axis one can find the same ratio for the more strongly scattering laminate B. The vertical error bars indicate the $\pm 90\%$ confidence level that was introduced in Section 2.5.

The simulations range from diffusion-like light propagation (low l_t^A/a) to ballistic-light propagation (high l_t^A/a). On the left the Monte Carlo simulations resemble the expectations from the diffusion theory, as the anisotropy ratios are almost three $\sigma_y^2/\sigma_x^2 \approx w_y^2/w_x^2 \approx 3$. By increasing the parameter l_t^A/a , the simulation results start to differ from diffusion theory. The ratio of σ_y^2/σ_x^2 and w_y^2/w_x^2 starts to decrease. This decrease corresponds to a rounder light spot on the front side of the laminate structure. This happens due to a less pronounced anisotropy in the effective scattering parameters of the laminate structures. The performance of the laminate structure is flawed for $l_t^B/a \geq 10^{-2}$ and $l_t^A/a \geq 10^{-1}$. For $l_t^A/a \approx 1$, half of the performance is lost and the simulations show $\sigma_y^2/\sigma_x^2 \approx w_y^2/w_x^2 \approx 2$. In this regime, neither diffusive nor ballistic-light propagation solely dominates the behavior of light propagation in the simulated laminate structure. Further increasing l_t^A/a finally leads to a ballistic transmission through the laminate sample with no anisotropy of the sample hence $\sigma_y^2/\sigma_x^2 \approx w_y^2/w_x^2 \approx 1$. Note that the maximal transmission is $T = 88\%$ because of the geometry. For $L_x = L_y = 8L_z$ the missing 12% of the ballistic-light leave the sample through the sides.

The conclusion of these simulations with this line of reasoning seems to be straight forward: keep l_t^A/a below 0.1 and you get the desired anisotropy. But as mentioned before l_t^A/a can not only be interpreted as a variable l_t^A with a fixed a but also the other way around. If there is a laminate with fixed l_t^A and one would have to decide for a laminate period a , one can have a different look at the problem. In order to get an effective material, usually small laminate periods are desirable to homogenize the light distribution in the direction of the alternating laminates (in our sample the x -direction). But the findings above ask for high laminate periods a in order to get low l_t^A/a and to achieve good laminate performance.

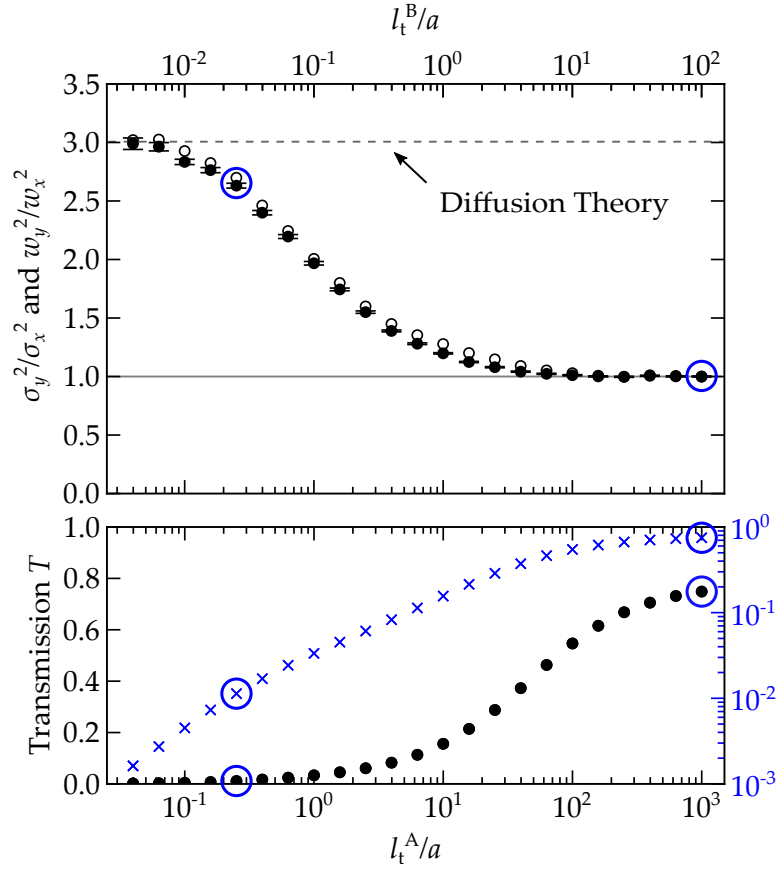


Figure 3.6: Results of 23 Monte Carlo simulations with fixed $l_t^A/l_t^B = 10$ and varying l_t^A/a . The upper panel shows the anisotropy ratio σ_y^2/σ_x^2 with full dots and w_y^2/w_x^2 with open dots on a linear vertical axis and the corresponding ratio of the transport mean free path length of laminate A to the laminate period l_t^A/a on the lower logarithmic horizontal axis. Note that for the clarity, the upper logarithmic axis shows the ratio of the transport mean free path length in laminate B to the laminate period l_t^A/a . The dashed line indicates the expected anisotropy ratio following the diffusion equation. Only small l_t^A/a lead to a diffusion equation like behavior. Large l_t^A/a lead to no anisotropy ($\sigma_y^2/\sigma_x^2 = 1$). Vertical error bars indicate the $\pm 90\%$ confidence level. The lower panel shows the transmission of the laminate structure on the same horizontal axis as the panel above. The black vertical axis on the left with the full black dots indicate the transmission on a linear scale. To improve the visibility of changes despite a very low transmission, the right vertical axis with the cross shaped data points indicates the transmission on a logarithmic scale in blue. Blue circles indicate the simulation results discussed in more detail in Figures 3.2, 3.4 and 3.5. Figure adapted from [77].

The consequence of this would be a strongly inhomogeneous transmission in one

direction. This effect can be seen in Figure 3.2 and in more detail in Figure 3.4 in red. In addition to this effect, the transmission of the sample changes drastically within the range of simulated l_t^A/a .

In the lower panel of Figure 3.6 the transmission is depicted on both, a linear and a logarithmic scale.

In this context, the transmission is defined as the amount of photons that leave the laminate sample on the front side N_t divided by the amount of photons that enter the sample on the back side N (half of the photons started as we have an isotropic light source). It is plotted on the left vertical axis on a linear scale that corresponds to the full black dots. The right vertical axis shows the transmission on a logarithmic scale in blue. On the horizontal axis, the same ratios l_t^A/a and l_t^B/a as in the upper panel are depicted.

For the diffusive regime ($l_t^A/a \leq 10^{-1}$), the transmission is well below 1%. To showcase a device for diffuse-light propagation, one usually aims for a high transmission. For 5% of transmission, a ratio of the transport mean free path length to the laminate period of about $l_t^A/a \approx 1.8$ is required. This set of simulation parameters leads to an anisotropy of about $\sigma_y^2/\sigma_x^2 \approx w_y^2/w_x^2 \approx 1.75$ and thus not at all to the desired anisotropy of about three.

This behavior of laminate structures seems to be unfortunate in the sense of designing devices with high transmission as well as a strong anisotropy that behave like an effective material. The decline in anisotropy for increasing ratios of l_t^A/a is rather fast. To check whether this behavior is due to the fixed simulation parameters we chose, the ratio of $l_t^A/l_t^B = 10$ is varied to 25 and 5 in the next set of simulations.

3.4.3 Results for Increased Laminate Contrast

Figure 3.7 shows the results of 23 simulations with a corresponding ratio of transport mean free path length of $l_t^A/l_t^B = 25$. Note that while the range of l_t^A/a is the same as in the simulations for Figure 3.6, the range of l_t^B/a is different and hence the upper horizontal axis is shifted. In order to compare Figures 3.6 and 3.7 in a meaningful way, it is good to fix the range of l_t^A/a as laminate layer A is the less scattering layer and thus, the ratio of l_t^A/a will determine the decrease of the anisotropy ratio as the diffusion approximation will be violated in layer A more likely than in layer B.

For a ratio of transport mean free path length l_t^A/l_t^B or a ratio of the density of scatterers in the constituent materials of n_s^B/n_s^A , diffusion theory predicts an anisotropy ratio of almost seven: $\sigma_y^2/\sigma_x^2 = w_y^2/w_x^2 = 6.76$ (see Equation 3.5). This prediction is indicated with a dashed line and it is confirmed for very short transport mean free path lengths compared to the laminate period. The difference

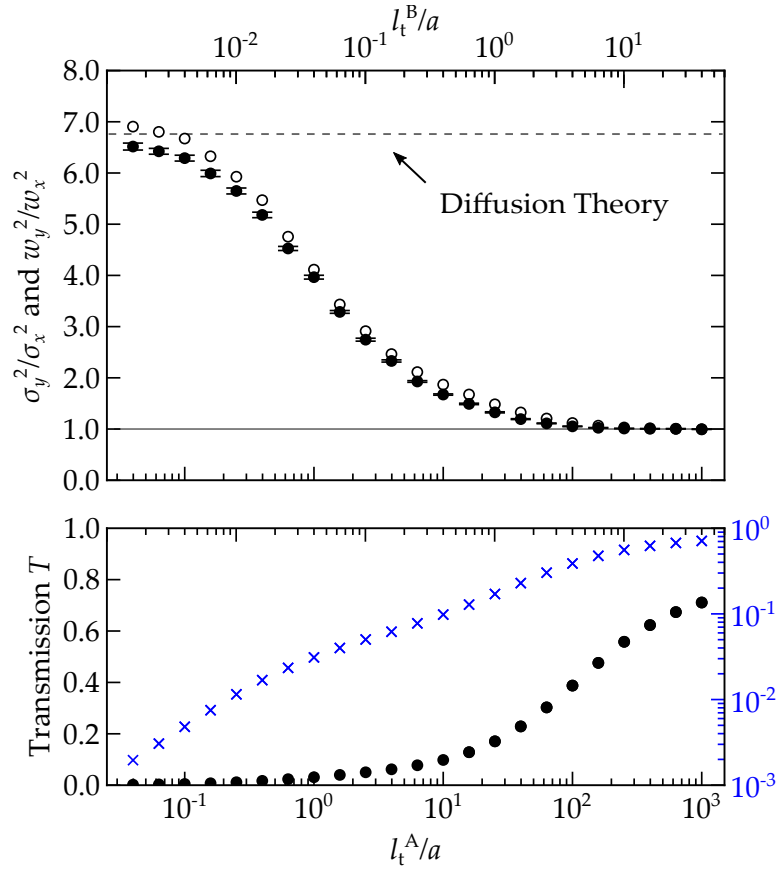


Figure 3.7: Same parameters as in Figure 3.6 but for $l_t^A/l_t^B = 25$. Due to the higher difference in mean free path length a much larger anisotropy can be reached. Diffusion theory predicts an anisotropy ratio of 6.76 and the simulations confirm this value for low l_t^A/a . The higher anisotropy drops down to 1 within the same range of l_t^A/a as in Figure 3.6. The transmission is overall a little bit smaller as laminate B is more strongly (back) scattering. Figure adapted from [77].

between the circles and the full dots can be traced back to the different measure they represent. The size of the transmitted spot on the front surface is rather small compared to the laminate period a for $l_t^A/l_t^B = 25$ and $l_t^A/a \leq 1$. As a consequence, the influence of the imperfection (ups and downs in contrast to the fitted Gaussian in Figure 3.4) of the intensity in x -direction increases. This imperfection is handled differently by the square root of the mean squared displacement σ and the square of the mean square root displacement w . The σ measure is influenced more by exit positions far away from the center of the light spot. The w measure does not weight these exit positions that much and thus is influenced more by exit positions within the first couple of laminate periods. In consequence, the above-mentioned deviation due to the finite spot size is stronger for the w measure than for the σ measure and thus the results differ a little bit for low l_t^A/a .

The overall decline of the anisotropy ratio in Figure 3.7 is similar to the one shown in Figure 3.6. For $l_t^A/a \leq 10^{-1}$ a behavior close to the one predicted by the diffusion equation is shown. This high ratio of $\sigma_y^2/\sigma_x^2 \approx w_y^2/w_x^2 \approx D_{yy}/D_{xx} = 6.76$ decreases to about half of its value for $l_t^A/a \approx 1$. Almost ballistic behavior of light is resembled by $l_t^A/a \geq 10^2$. In this regime almost no anisotropy is visible although the transmission is still below 50%. The overall transmission in these simulations is lower, as laminate layers B are more strongly scattering. To achieve a transmission of about 5%, the transport mean free path length in laminate A l_t^A has to be 2.5 times longer than the laminate period a . This leads to an anisotropy ratio of this laminate device of about $\sigma_y^2/\sigma_x^2 \approx w_y^2/w_x^2 \approx 2.75$ which is below half of the desired $\sigma_y^2/\sigma_x^2 = w_y^2/w_x^2 \approx 6.76$.

In consequence, increasing the ratio of transport mean free path length of the constituent materials does not change the overall behavior of the laminate structure in regard to the loss of anisotropy performance for higher values of l_t^A/a and thus higher transmissions. To check these findings as well for a lower difference in transport mean free path length, these results are compared to simulations with $l_t^A/l_t^B = 5$.

3.4.4 Results for Decreased Laminate Contrast

In analogy to Figure 3.6, Figure 3.8 shows the anisotropy ratios σ_y^2/σ_x^2 and w_y^2/w_x^2 in dependence of l_t^A and l_t^B , but for $l_t^A/l_t^B = 5$. Within the diffusion approximation an anisotropy ratio of $\sigma_y^2/\sigma_x^2 \approx w_y^2/w_x^2 \approx D_{yy}/D_{xx} = 1.8$ is expected following Equation 3.5. This value is marked by a dashed horizontal line and its prediction is almost met within the Monte Carlo simulations for $l_t^A/a \leq 10^{-1}$. In the transition regime $10^{-1} \leq l_t^A/a \leq 10^2$, the relative decrease in anisotropy ratio follows the lines of the simulations before. For transport mean free path lengths l_t^A longer than 100 laminate periods, the anisotropy of the transmitted light spot almost vanishes. The transmission of these simulations is slightly higher than the ones depicted in Figures 3.6 and 3.7. Picking a transmission of $T = 5\%$ again, the transport mean free path length of a photon in laminate A has to be about 1.05 times longer than the width of the laminate period. The corresponding set of simulation parameters leads to an anisotropy ratio of about $\sigma_y^2/\sigma_x^2 = w_y^2/w_x^2 \approx 1.3$ which is once again below the desired anisotropy ratio of 1.8.

In comparison, the three groups of simulations depicted in Figures 3.6, 3.7 and 3.8 show a lot of similarities. There seems to be a limit at about $l_t^A = a/10$ for diffusion like light transport. Hence above this limit, the effective anisotropy of the laminate device is smaller than predicted by the diffusion equation. Within three orders of magnitude ($10^{-1} \leq l_t^A/a \leq 10^2$), the anisotropy effect of the laminate structure is decreasing and for larger ratios of l_t^A/a , there is almost no scattering

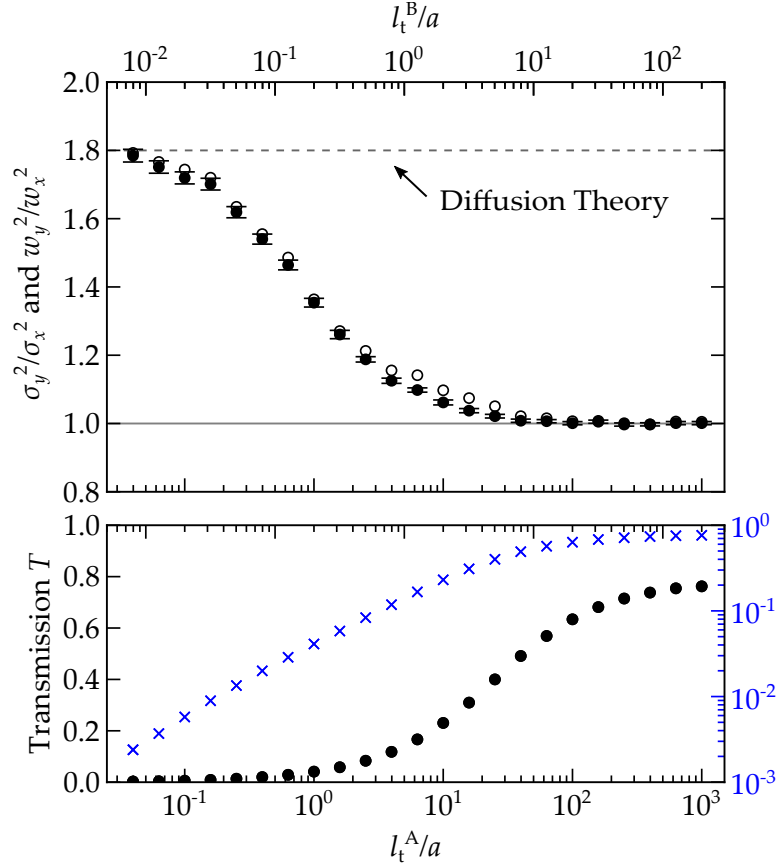


Figure 3.8: Same parameters as in Figure 3.6, but $l_t^A/l_t^B = 5$. According to the diffusion equation, the anisotropy ratio of $\sigma_y^2/\sigma_x^2 = w_y^2/w_x^2 = D_{yy}/D_{xx} = 1.8$ is expected. This is only true for very small l_t^A/a . Larger l_t^A/a lead to a less pronounced anisotropy and finally to isotropic ballistic-light propagation. The transmission is a little bit higher than in Figure 3.6, as laminate layers B are less scattering. Figure adapted from [77].

and hence ballistic-light transport without any anisotropy takes place.

Other than the ratio of the transport mean free path lengths in the constituent materials l_t^A/l_t^B also some other simulation parameters might influence the relation between transport mean free path length in laminate layers A divided by the laminate period l_t^A and the anisotropy ratios of the transmitted light spot σ_y^2/σ_x^2 and w_y^2/w_x^2 .

3.4.5 Results for Anisotropic Scattering

In the beginning of this chapter, the anisotropy factor g of the individual scattering events was mentioned and subsequently set to $g = 0$ (i.e. isotropic scattering).

In Section 2.1.5 this factor is explained in more detail. The transport mean free path length l_t (i.e. the average distance after which the direction of a photon is randomized) is only equal to the scattering mean free path length l_s (average distance traveled between two scattering events) for isotropic scattering ($g = 0$). In general, they are connected by $l_t = \frac{l_s}{1-g}$. In the following simulations, we set $g = 0.5$ and thus $l_t = 2l_s$. As we are looking at the same range of l_t^A/a , the amount of scattering events will go up by a factor of about two.

Comparing Figure 3.9 to Figure 3.6, both have a ratio of ten in their transport mean free path lengths $l_t^A/l_t^B = 10$. The only difference in the set of simulation parameters is the anisotropy of the individual scattering events. The result of these simulations is almost identical to the ones with $g = 0$ for the upper panel. The decrease of anisotropy ratios σ_y^2/σ_x^2 and w_y^2/w_x^2 resembles the behavior in Figure 3.6. Also the transmission in the lower panel does not show any significant difference.

The only difference is the simulation time, that is not shown here. As the Monte Carlo simulation calculates the path of photons step by step, the overall number of scattering events is crucial for the simulation time. With $g = 0.5$, the number of scattering per transport mean free path length l_t doubles and thus, the simulation time increases as well by almost a factor of two as well. By this simulation, the assumption that l_t is the length scale that is crucial for the spread of light is once more confirmed.

3.4.6 Results for Realistic Refractive Index

In order to simulate a laminate structure more close to a real life experiment, we repeat once again the first set of simulations but with a refractive index of $n = 1.4$ (see Figure 3.10). For most of our real life experiments, we use polydimethylsiloxane (PDMS) as a host material for titanium dioxide (TiO_2) scattering particles. As the refractive index for PDMS is about $n \approx 1.4$, this set of simulations is even closer to reality than the ones before.

Once again, the simulation with $n = 1.4$ resembles predicted results for small ratios of transport mean free path in laminate layers A and the laminate period l_t^A/a . Just as in Figure 3.6, the anisotropy ratios decrease within about three orders of magnitude to almost 1 and consequently, the ballistic-light behavior is resembled.

In the lower panel of Figure 3.10 there is a clear difference to Figure 3.6. The transmission does not reach 88% but rather decreases for very low scattering (high l_t^A/a). This effect is due to total internal reflection. For no scattering in the laminate structure, ballistic-light can only escape the structure within an angle

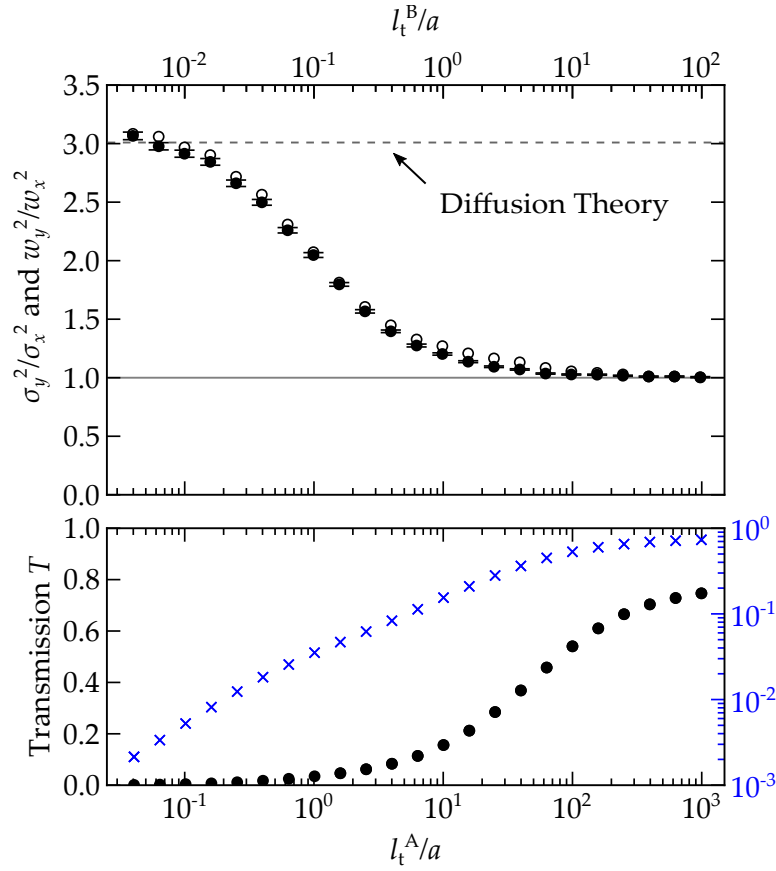


Figure 3.9: Same parameters as in Figure 3.6 but with $g = 0.5$. The change of the anisotropy of the individual scattering events g is taken in account by the choice of fixed simulation parameter: l_t^A/a . Hence, the behavior in this plot is (within the statistical errors) just the same as for $g = 0$. Figure adapted from [77].

that is below the angle for total internal reflection (about 45°). This results in only a small circle of exit positions around the middle of the front surface with radius $r \approx L_z \tan(45^\circ) = L_z = L_x/8$. The rest of the light is reflected back and leaves the laminate device through the side surfaces. This effect only occurs for photons that have not been scattered and the effect vanishes for more diffusion like light transport. Besides the effect of total internal reflection, there is no difference between the simulations shown in Figure 3.6 and in Figure 3.10. Our findings are quite general as they are not bound to a certain ratio transport mean free path lengths of the constituent materials, to the anisotropy factor of the individual scattering events or to the refractive index of the laminate structure.

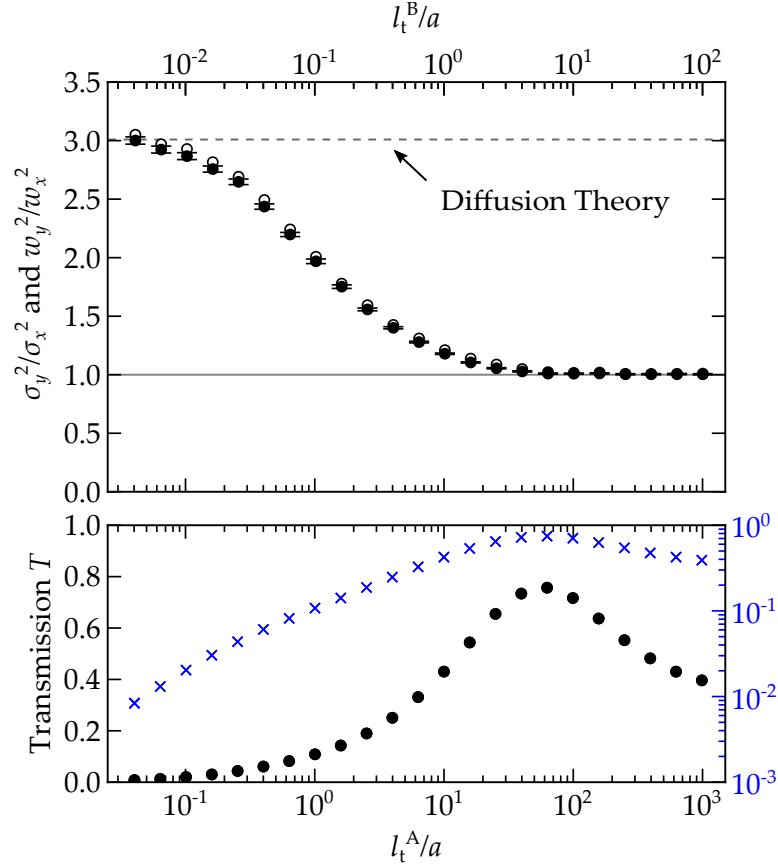


Figure 3.10: Same parameters as in Figure 3.6, but with refractive index $n = 1.4$ instead of $n = 1.0$. There is no change in anisotropy compared to Figure 3.6 (upper panel). However, there is a change in transmission. The maximal transmission is reached for $l_t^A/a \approx 60$. Increasing l_t^A/a further results in lower transmission, as total internal reflection prohibits the photons from exiting through the front surface of the laminate structure. Figure adapted from [42].

3.5 DISCUSSION

For transport mean free path lengths a lot longer than the laminate period, $l_t \gg a$, the influence of the laminate structure vanishes. This effect can be explained by an intuitive explanation: Imagine a scattered photon, that has an average step size l_t for $l_t^A > l_t^B \gg a$ the path length will most likely exceed several laminate layers. As the path length will be calculated by the individual scattering probabilities of the passed layers, the result will be an average of the individual laminates. As the photons tend to average over a lot of laminate layers, the individual orientation of the laminates, that only change the absolute number of passed laminates, does not affect the laminates anymore and the scattering behavior becomes isotropic as seen in Figure 3.2 Panel b) and the lamination is not visible in the intensity.

For very short transport mean free path lengths l_t in relation to the thickness of the laminate period a , the Monte Carlo method resembles the predictions of the diffusion equation. As discussed, $l_t^A/a \ll 1$ does not only lead to a very low transmission but also to a pronounced striped image of the intensity as seen in Panel a) of Figure 3.2 and in Figure 3.4.

It seems like there is no perfect set of parameters but one has to choose a set to its needs: either one gets a high transmission with fine lamination or one gets high anisotropy.

Still, there are some tricks one can learn from the simulations above. To reach an anisotropy of 1.8 one can either try to fulfill the diffusion approximation and go for the very left simulation point in Figure 3.8 with a ratio in transport mean free paths of $l_t^A/l_t^B = 5$ and a transmission of about 0.2% or one can go for a higher ratio of the constituent materials like $l_t^A/l_t^B = 25$ and then harm the diffusion approximation by using less scatterers. As shown in Figure 3.7, with an $l_t^A/a \approx 6.5$ one still gets the desired anisotropy of $\sigma_y^2/\sigma_x^2 = 1.8$ but the transmission will be at about 10.5%. In real world experiments there are limits to the number of scattering particles per unit volume (see Section 2.1.2). Hence, this trick cannot be applied indefinitely. But in fact, this is a way how cloaking devices in our group were optimized. When a laminate like structure (in a core-shell cloak) did not work as diffusion equation predicted, because the diffusion approximation was harmed, the solution was to lower the number of scatterers in the shell and thus increasing the ratio of l_t^A/l_t^B until perfect cloaking was achieved. With the results of this work in hand, it might be a bit easier to estimate the performance of laminate like structures and thus be more efficient in designing devices for diffuse-light.

3.6 CONCLUSION

Within this chapter, we systematically characterized exemplary light-scattering laminate structures within the aim of realizing effective materials with tailored anisotropic diffusivities. Using a Monte Carlo method based simulation algorithm, finite transport mean free path lengths and thus finite density of scatterers were simulated. The scattering conditions simulated range from diffuse-light propagation conditions to ballistic-light propagation conditions.

For small transport mean free path lengths or coarse laminates, the predictions of the diffusion equation were confirmed. In the limit of fine laminates ($a \ll 1 \rightarrow l_t/a \gg 1$) there is no effect of the lamination visible in the shape of the transmitted light spot. The limit of fine lamination will always harm the diffusion approximation and thus fine laminate structures for light diffusion will not work.

The two extremes were well-known before this work but with the results presented here in hand, the transition from diffuse-light propagation to ballistic-light propagation is accessible with the very same simulation tool.

The findings of this work can be relevant to the design of almost all diffuse-light devices, that aim for a high transmission and anisotropic material parameters at the same time.

4 SPECKLE ANALYSIS OF DIFFUSE-LIGHT CLOAKS

Invisibility cloaks are one of the most fascinating devices in optics. Turning something invisible for an observer is not only an impressive achievement but also usable for other issues. With the help of invisibility cloak technology for example, contact wires on OLEDs or on solar cells can be cloaked [40, 80].

One needs different cloaks to hide something depending on the surrounding: Maybe the most prominent invisibility cloaks are free space cloaks. Hiding something in the ballistic light regime is possible but has some fundamental limits. As light in general cannot be accelerated beyond the speed of light in vacuum, the detour around an object will always be connected to a time delay for free space cloaks. There are ways around this problem for small bandwidths of light but then these cloaks will lose their cloaking ability for other wavelengths [2–10]. In general, every cloak is designed for a specific purpose and optimized to perform as good as possible in this context: Even a perfect cloak for diffuse-light will be visible in ballistic light conditions and vice versa. As all cloaks have their advantages and their flaws, finding the limits of cloaks is an important part of improving research on cloaks and in optics in general.

In context of the stationary diffusion equation, it is possible to design almost ideal invisibility cloaks for diffuse-light. These devices can hide an object in a light-scattering environment by convincing the observer that the flow of light in the scattering environment is not changed by its presence. These cloaks work for any polarization, all colors of light, and any illumination direction. But the basis of these cloaks is the validity of the diffusion equation. In the context of coherence, the diffusion equation is only valid in the limit of very short coherence length. As the diffusion approximation does not take into account any coherence effects, one might assume that a cloak for diffuse-light might be uncloaked by coherent light.

In this chapter, the diffuse-light cloak designed by R. Schittny [81] is put to test with coherent laser light. Experiments reveal a good performance of the cloak for perfectly coherent light. Then again tuning the coherence length gives insight into the scattering process and consequently reveals the cloak. These findings are

supported by theoretical work. Large parts of the work in this chapter have already been published in 2017 within the scope of a collaboration between our group at KIT and the research group of Professor Yamilov at Missouri S&T, USA [82].

The samples used in this chapter and their properties were first published in 2015 [81] and a former water based sample was published in 2014 [30]. The improvement of the samples from water based surrounding to a rather solid, rubber like material is crucial for this work. Moving particles in the samples would annihilate any coherence effects visible, as the shutter time of the camera usually is much longer than the time a stable speckle picture is visible.

4.1 EXPERIMENTAL SETUP AND FIRST RESULTS

4.1.1 Reference, Obstacle and Cloak Samples

The set of samples presented in 2015 [81] consist out of three individual samples. There is the reference sample (see Figure 4.1), a plain cuboid with dimensions $L_x = 150$ mm, $L_y = 80$ mm, and $L_z = 30$ mm. This cuboid is made up of the clear rubber like material polydimethylsiloxane (PDMS), doped with Titania nanoparticles (DuPont R700 TiO_2 particles, diameter ≈ 340 nm). The concentration of these scattering particles leads to a transport mean free path length of $l_t^0 = 1.67$ mm. This corresponds to a diffusivity of $D_0 = 11.9 \times 10^8$ cm²/s. For a wavelength of $\lambda = 780$ nm and a refractive index of the PDMS of about $n = 1.42$, the scattering of light at the scattering particles has preferred forward scattering, leading to an anisotropy factor of $g = \langle \cos \theta \rangle = 0.544$ and thus, the scattering mean free path length in this sample is $l_s^0 = 0.76$ [57, 81].

The second sample is the so-called obstacle sample, depicted in Figure 4.2. Additionally to the same surrounding as the reference sample, the obstacle sample contains a high reflective cylinder that is located in the middle of the xz -plane, oriented in the y -direction. This hollow cylinder with an outer diameter of $R_1 = 8$ mm has a near zero diffusivity $D_1 \ll D_0$. The low diffusivity of this core is realized by a special ceramic material (Accuratus Corporation, Accuflect B6).

The cloak sample shown in Figure 4.3 contains an additional PDMS layer around the core of the obstacle sample. The outer radius of this shell around the core is $R_2 = 12$ mm and the concentration of scattering particles is 3.9 times lower than in the surrounding. This corresponds to a diffusivity of $D_2 = 3.9 \times D_0 \approx 46 \times 10^8$ cm²/s. The high diffusivity makes up for the low diffusivity of the core and thus, the overall flow of light is not disturbed by the core and the shell turning them invisible (see Section 2.3). As the core is hollow and the low diffusivity D_1 does not allow any light to enter the core material, small objects can be placed in

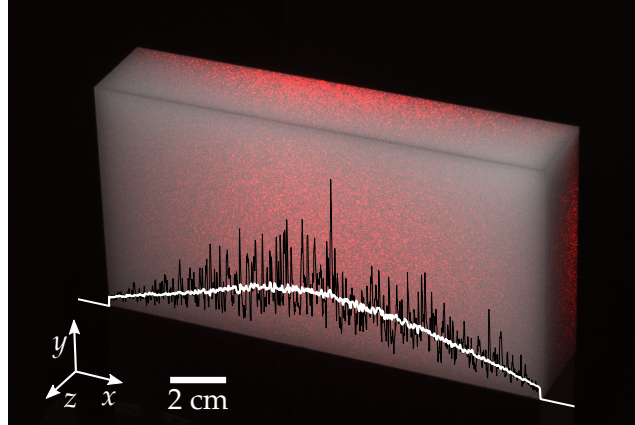


Figure 4.1: Reference sample under coherent illumination. The sample shown is called the reference sample. It is a simple cuboid with size $L_x = 150$ mm, $L_y = 80$ mm, and $L_z = 30$ mm. It consists of a clear host material (polydimethylsiloxane - PDMS) and scattering particles randomly distributed within the volume (DuPont R700 TiO_2 particles, diameter ≈ 340 nm). The picture shown is a combination of two photographs. First, a white light illumination picture is taken to make the contour visible, then the illumination is changed to a coherent illumination centered on the middle of the back side of the sample (Gaussian shape FWHM ≈ 4 cm) and another picture is taken. These two pictures are added up pixel by pixel. The black line shows the intensity variation of pixels with the same height over the width of the sample. The white line shows the same as the black line but it averages the pixels in y -direction for plus minus two centimeters. The black line shows the intensity variation of the speckles and as the white line averages over the speckles and hence, a smooth intensity curve is received. Figure adapted from [82].

the middle of the cloak sample making it not only an invisible device but a real invisibility cloak.

4.1.2 First Experiments

First experiments with coherent light are shown in Figures 4.1, 4.2, and 4.3. A coherent laser beam (Toptica, DL100 $\lambda = 780$ nm) with a coherence length of more than 60 m is slightly diverged and centered onto the back side of the samples. The black lines are intensity cuts at the front side along a horizontal line at half the height of the samples. These lines show the strongly varying intensity due to the speckles emerging (more on the origin of speckles in Section 2.6). The white line shows the average brightness of the transmitted light starting from 25% up to 75% height of the sample. Here, the individual speckle patterns average out.

Comparing the obstacle sample in Figure 4.2 to the reference sample in Figure 4.1, a pronounced shadow in the middle of the sample is visible. This region in

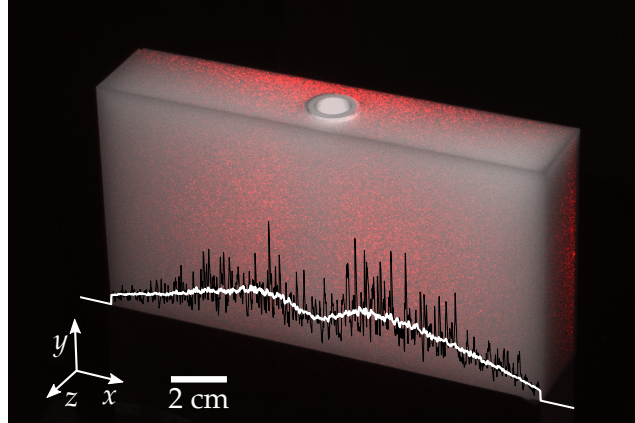


Figure 4.2: Obstacle sample under coherent illumination. Same as Figure 4.1 but the obstacle sample is shown. The obstacle sample has the same surrounding material as the reference sample but with a cylindrical hole in the center of it (oriented in y -direction, radius 8 mm). This hole is partially filled with a white ceramic cylinder (height $L_y = 80$ mm, outer radius $R_1 = 8$ mm, inner radius $R_0 = 4$ mm). This cylinder consists of a high reflective material to act like a diffuse mirror (Accuratus Corporation, Accuflect B6). The ceramic core casts a diffuse shadow onto the front surface of the sample. Hence, the white line has a dent in the middle. Figure adapted from [82].

the middle of the obstacle front surface with less red speckles reveals the presence of an object (the core and whatever is within this core) to an observer.

In contrast to the obstacle sample, the additional shell around the core in the cloak sample (see Figure 4.3) allows the light to circuit the core and to resemble the average light distribution of the reference sample. Hence the average brightness on the front side of the cloak sample is the same as the average brightness of the reference sample on the front side (see white lines in Figures 4.1 and 4.3).

One might think that due to the difference in the individual speckle pattern the cloak might be unmasked, but even a second reference sample with the same material parameters would have a different speckle pattern compared to the original reference sample as the positions of the scattering particles are random and hence the speckle pattern is random as well. Thus, only statistical measures might be consulted to find a way to uncloak the cloak.

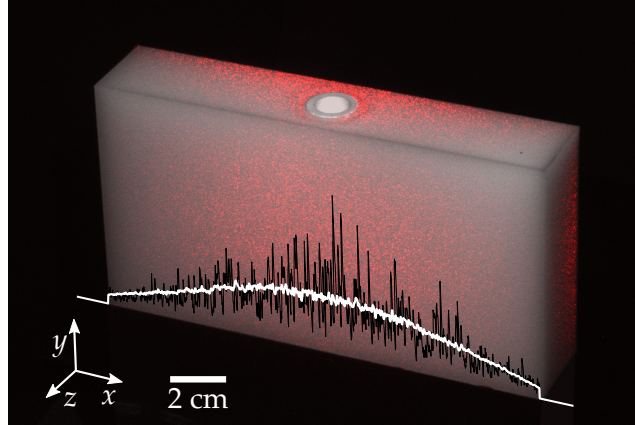


Figure 4.3: Cloak sample under coherent illumination. Same as Figure 4.1 and Figure 4.2 but the cloak sample is depicted. In addition, to the obstacle sample, the cloak sample features not only the hollow core but also a shell around this core (inner radius $R_1 = 8\text{mm}$, outer radius $R_2 = 12\text{mm}$). The material in the shell is the same as in the surrounding of all samples but with a lower concentration of scattering particles (see Section 2.3). The shell guides light around the core and the shadow visible in Figure 4.2 is not visible anymore. The black line that shows the speckle pattern in one row is unique but the white line that averages over the individual speckles resembles the behavior of Figure 4.1. Figure adapted from [82].

4.1.3 Improved Setup and Statistical Analysis

To investigate the statistics of the transmitted light in more detail, the measurement setup is changed. As a first improvement, we use a microscope objective (Olympus, 605339, $10\times$, $\text{NA} = 0.25$) to magnify the studied area for better speckle resolution. The size of speckles mainly depends on the imaging system. Larger magnifications give better insight into the size and the brightness of individual speckles.

If there is a difference in the statistical distribution of the coherent transmission of the cloak sample compared to the reference sample, this effect will be maximal right in the middle behind the core-shell geometry. Therefore the microscope objective is placed in the middle of the xy -plane to image about 1mm^2 of the front surface onto the camera chip (Point Grey, BFLY-PGE-50H5M-C, 12 bits dynamic range). In addition, the illumination is changed to a collimated beam with a FWHM of about 2 mm. To maximize brightness at the observed area on the front side, the laser is set to illuminate the sample at the center of the back side. In addition and there is a linear polarizer directly in front of the camera, as without this polarizer one would capture the incoherent superposition of two individual speckle patterns. To put the degree of development of speckles in a number, we use the speckle contrast C_I that was introduced in Section 2.6

$$C_I = \frac{\sigma_I}{\mu_I} = \frac{\sigma_I}{\langle I \rangle}. \quad (4.1)$$

To calculate the speckle contrast, the mean of the intensity

$$\langle I \rangle = \frac{\sum_{i,j} I_{i,j}}{N} \quad (4.2)$$

and the intensity standard deviation

$$\sigma_I = \frac{\sum_{i,j} (I_{i,j} - \langle I \rangle)^2}{N} \quad (4.3)$$

have to be known. The number of pixels N of the camera chip is 2448×2048 . Saturated pixels pose a problem to these calculations as they would distort the speckle statistics. To avoid saturation, the exposure time of the camera is set quite low to limit the average intensity to about $\langle I \rangle \approx I_{\text{sat}}/15$. To minimize the influence of electric noise on the camera chip, a series of background images without any illumination is recorded before the actual measurement and later, the mean image of these background images is subtracted from every individual picture taken. This can result in an effective negative brightness for some individual pixels, but does improve the overall image quality.

Two pictures obtained like this are depicted in the upper panels of Figure 4.4. The left one shows the reference sample and the right one shows the cloak sample. Note that in this configuration the individual speckles can be resolved. Although the individual speckle patterns look different ($I_{i,j}^{\text{ref}} \neq I_{i,j}^{\text{clk}}$), the histogram analysis in the lower panel shows, that the pictures obtained have the very same behavior within their statistical fluctuation. Most of the pictures is dark and there are only some very bright pixels. The speckle contrast of both pictures is 95% and the reason for the speckle contrast not being 100% is mostly the electrical noise on the camera. Subtraction of the background image reduces this problem but the electric noise still lowers the contrast by about 5%.

This experiment so far shows that diffuse-light cloaks, although only designed for white light, cannot be revealed by perfectly coherent light by simply looking at their transmission. There has been theoretical work on uncloaking the cloak via the long-range contribution of the second-order intensity correlation function C_2 [83]. But in our case, the difference between cloak and reference would be as small as

$$|\Delta C_2^{\text{max}}| \approx \frac{1}{2} \frac{\lambda}{l_t^0} \frac{R_2^2}{L_z^2} \approx 4 \times 10^{-5}. \quad (4.4)$$

This small difference would be very difficult to measure for realistic signal to noise ratios and statistics. Thus, once again we find the presented cloak to be quite robust. Experimentally, the cloak works fine for incoherent white light illumination and for perfectly coherent illumination.

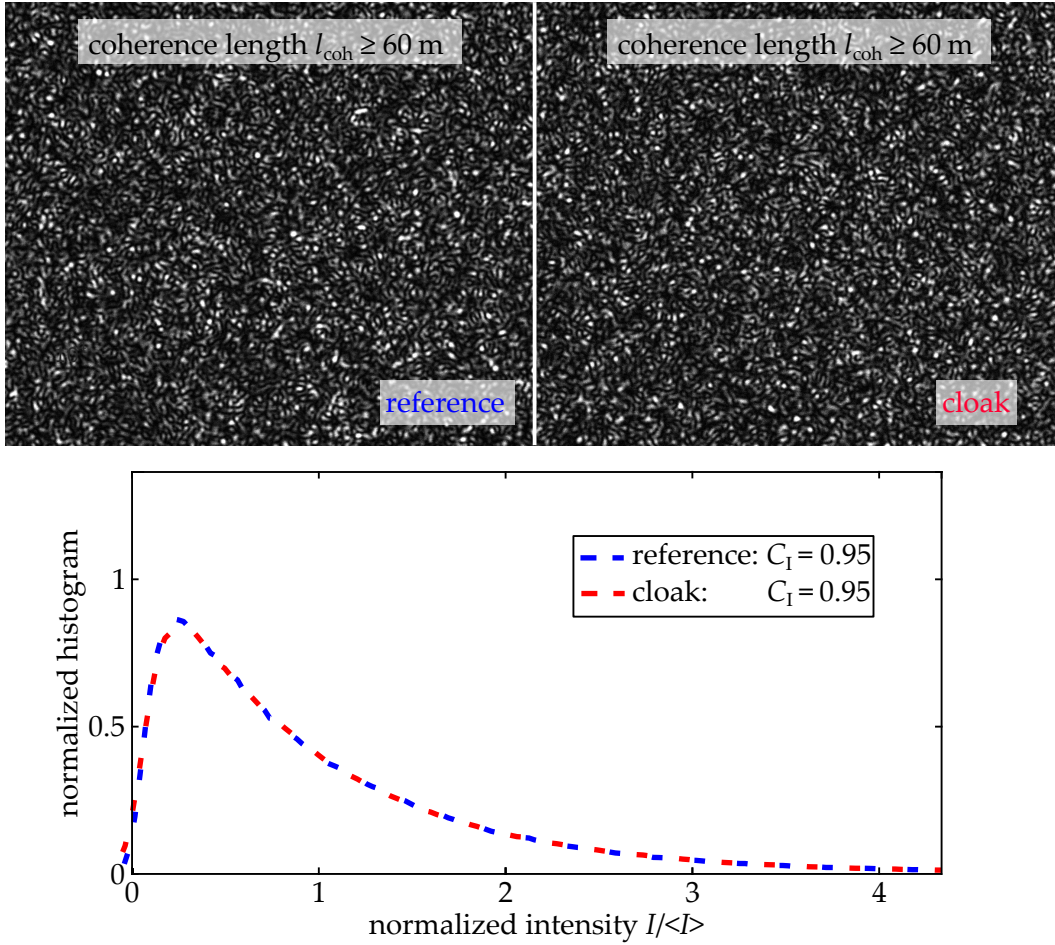


Figure 4.4: Coherent illumination analysis. In the upper panels pictures of the center (1 mm^2) of the front side of the reference sample (left) and the cloak sample (right) are shown. The samples are illuminated via the center of the back side with a collimated beam of perfectly coherent light. A background image (no illumination) is subtracted from these pictures pixel by pixel. The lower panel shows the histogram of the brightness of the pictures. Due to the subtraction negative values are possible as well. Both, the reference and the cloak sample lead to the same result: Most of the pixels are dark, but there are a few very bright pixels as well. The speckle contrast of both pictures is $C_1 = 0.95$ and thus, the cloak cannot be distinguished from any other reference sample with this kind of illumination.

4.2 SPECKLE CONTRAST FOR SEMI-COHERENT LIGHT

A possible way to uncloak the diffuse-light cloak has been discussed in 2015 [39]. Diffuse-light cloaks can always be uncloaked via a time-of-flight measurement. The principal behind this statement is illustrated in Section 2.3.3. The cylindrical core-shell cloak can be revealed by its different transmission time distribution compared

to the reference. This finding about temporal differences can be translated to a difference in length, as all photons have the same speed $v_{\text{ph}} = c_0/n$ in the sample with the refractive index of $n = 1.42$ and the vacuum speed of light c_0 . Knowing that the path lengths $p(l)$ traveled through the cloak are different from the path length traveled through the reference sample is a promising way to reveal the cloak without using a complicated setup with a pulsed laser and a single photon counter with picosecond accuracy. There have been works on the study of scattering media with semi coherent light [72, 73, 84, 85]. These works use the speckle contrast C_1 to get some information about the path length distribution of their samples. This approach was used to reveal the internal structure of a medium, buried objects within the scattering medium and it was even used in biomedical optics [32, 84, 86]. As this is a promising way, we try to go one step further to reveal a cloak that is perfectly hidden in terms of the stationary diffusion equation.

4.2.1 Illumination with Shorter Coherence Lengths

Figure 4.5 shows pictures illuminated with a finite coherence length. To realize a semi coherent illumination, we sweep the frequency of the laser via a sawtooth voltage at the piezo that changes the laser cavity. Integrated over time, this leads to a box-shaped frequency profile of the laser. This has to be repeated much faster than the shutter time of the camera. The sweeping is monitored via a Fabry-Perot interferometer (Toptica, FPI 780).

The left panels in Figure 4.5 show pictures of the reference (upper panel) and the cloak (lower panel) with a coherence length $l_{\text{coh}} = 0.5$ m. With the bare eye, these pictures still look as crisp as the ones for perfectly coherent light in Figure 4.4. The panels on the right side of Figure 4.5 show speckles that emerge at the front side of the reference and the cloak when illuminated by laser light with an effective coherence length $l_{\text{coh}} = 0.05$ m. The ten times shorter coherence length has an obvious influence on the pictures: With shorter coherence length, the pictures start to look blurry. There are no black areas and no bright spots anymore.

It is hard to see a difference between the pictures of the reference and the cloak sample within the same illumination. However, the histogram in Figure 4.6 shows clear differences. The dashed curves correspond to the illumination with a coherence length of half a meter, the solid lines correspond to an illumination with a coherence length of only five centimeters. Comparing the dashed lines the difference in the very left of the histogram is most obvious. The picture of the cloak (red) has more dark black pixels than the reference. For the solid lines we see a clear trend as well: The cloak has more dark pixels once again and even more bright ones as well. In contrast, the reference has more pixels with a brightness close to the mean value of the brightness. These findings

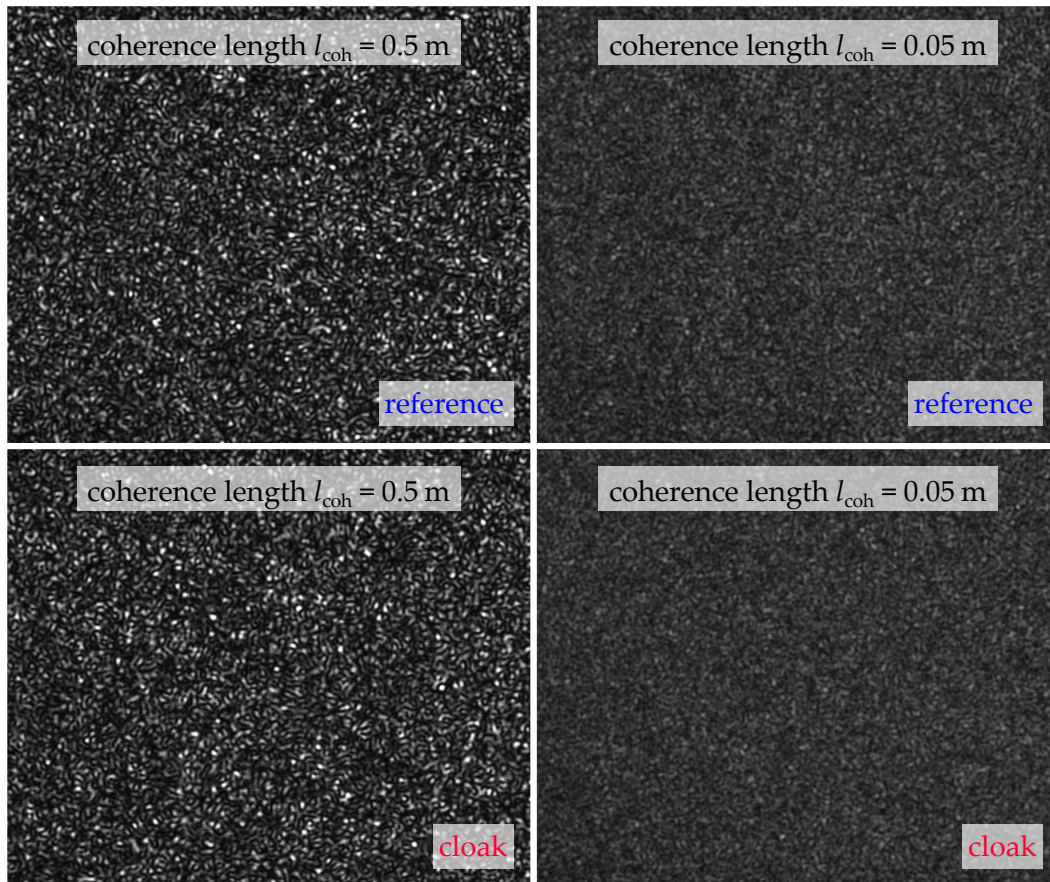


Figure 4.5: Partially coherent illumination analysis. Four pictures taken with the same configuration as the pictures in Figure 4.4 but with different coherent length of the illumination. The left panels show illuminations with $l_{\text{coh}} = 0.5 \text{ m}$. The panels on the right show pictures of an illumination with $l_{\text{coh}} = 0.05 \text{ m}$. The granular structure of the speckle pattern decreases with shorter coherence length, as the pictures on the right look more gray than the black and white pictures on the left. With the bare eye one cannot see a statistical difference between the reference (upper pictures) and the cloak (lower pictures). Figure partially adapted from [82].

are confirmed by the difference in speckle contrast depicted in the legend of Figure 4.6. The cloak sample seems to have a higher contrast than the reference sample when illuminated by semi coherent light. To solidify this finding, a series of measurements are taken with different coherence lengths on different days. This method seems to be inevitable as these measurements are very sensitive to several of disturbances.

Of course, light leakage onto the camera chip within a measurement will alter the speckle contrast, but also small vibrations of the sample changes the outcome of the experiment. If the speckle pattern changes during the shutter time of the

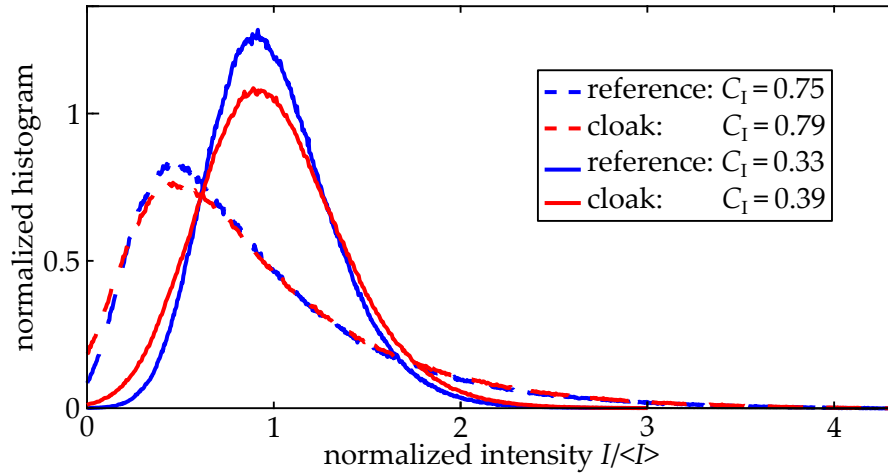


Figure 4.6: Histogram of the pictures shown in Figure 4.5. The dashed lines correspond to an illumination with coherence length of $l_{\text{coh}} = 0.5\text{ m}$, the solid lines correspond to an illumination with coherence length of $l_{\text{coh}} = 0.05\text{ m}$. In contrast to Figure 4.4, the histogram analysis reveals a difference between reference (blue) and cloak (red). In comparison to the reference, the cloak sample has a wider distribution of brightness in both cases of coherence length. The reference sample has more pixels with the same brightness what leads to a higher peak in the histogram. These findings are condensed in the value of the speckle contrast. For the same kind of illumination, the speckle contrast C_I is higher for the cloak than for the reference. Figure partially adapted from [82].

camera, the speckle contrast will be lowered. Getting a stable speckle pattern poses a challenge as there are a couple of reasons that the sample might move and even the slightest movement will lead to a completely different speckle pattern. Placing the samples onto the optical table always leads to tensions in the rubbery material. It takes about half an hour for these tensions to dissolve. Despite the air damped optical table, vibration from construction works anywhere in the building or harsh footsteps on the hallway next to the lab influence the speckle pattern as well. Last but not least, the air flow of the air conditioner shakes the samples a tiny bit and thus, the air conditioner has to be turned off for the time of the measurements. This list of known issues is certainly not complete and thus, we make sure via repetition that our measurements are valid.

4.2.2 Measurements on Multiple Coherence Lengths

In Figure 4.7, four groups of measurements are shown. Between those measurements, the samples have been moved and they were recorded on different days. The vertical axis depicts the speckle contrast C_I and the horizontal axis indicates the corresponding inverse coherence length l_{coh}^{-1} . The first measurements (see

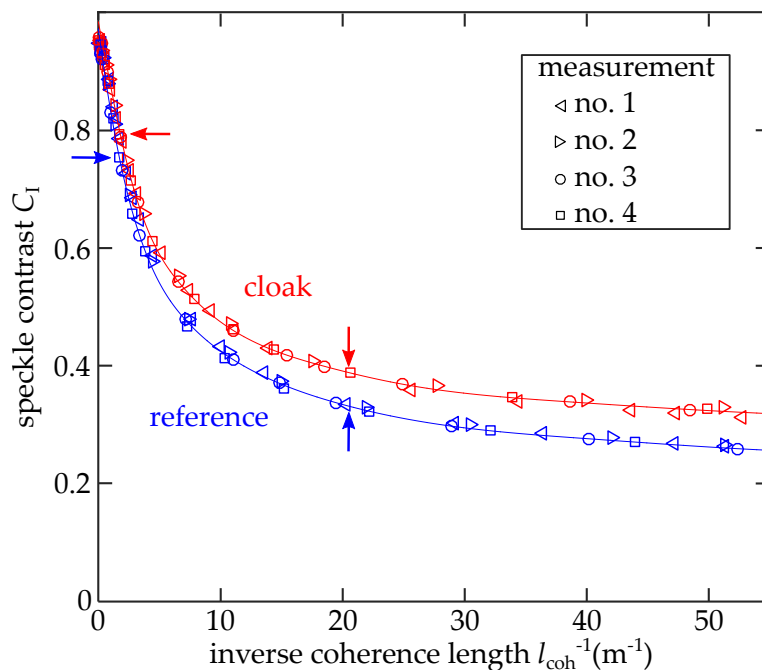


Figure 4.7: Speckle contrast of 150 pictures for reference (blue) and cloak (red) sample versus the inverse coherence length of their illumination. The setup is the same as for Figures 4.4 and 4.5. The pictures were taken in four experiments that took place on different days. The arrows indicate the measurements that were separately shown in Figures 4.5 and 4.6. The blue and red lines are guides to the eye. Figure adapted from [82].

Figure 4.4) with perfectly coherent light ($l_{\text{coh}} \geq 60 \text{ m} \equiv l_{\text{coh}}^{-1} \leq 1/60 \text{ m}^{-1}$) are added to this graph in the upper left corner. The results shown in Figures 4.5 and 4.6 are marked with horizontal arrows for $l_{\text{coh}} = 0.5 \text{ m}$ and with vertical arrows for the illumination with $l_{\text{coh}} = 0.05 \text{ m}$. The trend of the speckle contrast of the two samples is quite similar. With smaller coherence length, the speckle contrast drops down as well. The relative split between the two trends seems to rise with the decrease in coherence length as well.

These measurements support the assumption stated before: The cloak sample can be uncloaked by partially coherent light. The speckle contrast behaves significant and systematically different for illumination with light of different coherence length.

4.2.3 Theoretical Analysis

This finding can be approved by some theoretical calculations. In Section 2.6.2, the mathematical derivation of the speckle contrast is demonstrated. After some

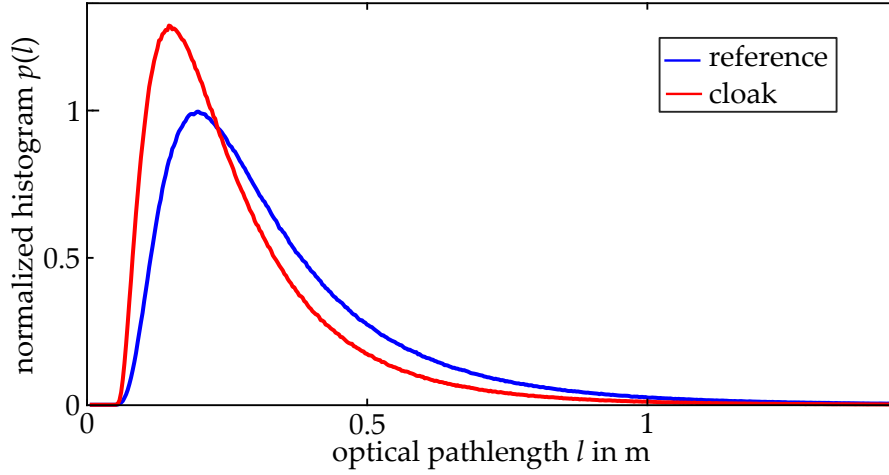


Figure 4.8: Simulated path length distributions for reference and the cloak sample. The dimensions and material parameter of the real samples are fed into the simulation. The illumination is a directional Gaussian source in the middle of the back side. The detection area is $10 \times 10 \text{ mm}^2$ large. The path lengths through the cloak sample (red) are shorter than the path lengths through the reference sample (blue).

calculations, we end up with the speckle contrast C_I :

$$C_I = \frac{\left(\int_0^\infty \int_0^\infty S(\lambda) S(\lambda') \left| \int_0^\infty p(l) \exp \left\{ -i2\pi l \left[\frac{1}{\lambda} - \frac{1}{\lambda'} \right] \right\} dl \right|^2 d\lambda d\lambda' \right)^{1/2}}{\int_0^\infty S(\lambda) d\lambda}. \quad (4.5)$$

Here, the speckle contrast depends on the spectral profile $S(\lambda)$ and the path length distribution $p(l)$. The term in the square of the absolute value is simply the Fourier transform of the path length distribution $p(l)$.

To calculate the speckle contrast according to Equation 4.5, we use the spectral profile that is equivalent to the coherence length we want to examine. The path length distribution is simulated by FRODO, the Monte Carlo ray tracing software introduced in Section 2.4. We use a Gaussian shaped collimated illumination with a FWHM of 2 mm centered in the middle of the backside of the samples. Next, we only collect the photons that exit the sample in an area of the center of the front side. The detection area is set to be $10 \times 10 \text{ mm}^2$. This is larger than the real experiment, but still reasonably small and like this, the simulation times were bearable. In contrast to simulations for Chapter 2.2, not the exit position but the path length of the individual photons is stored. Next, a histogram of the distribution of path lengths is created and depicted in Figure 4.8. Figure 4.8 shows that there are no photons arriving at the detector with a optical path length below approximately four centimeter. This is due to the ballistic path length: The

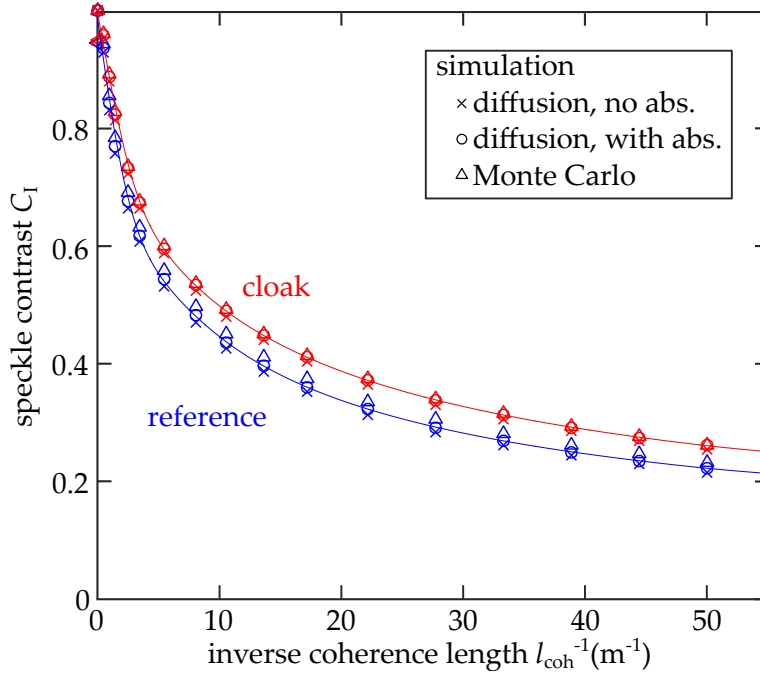


Figure 4.9: Simulated speckle contrast for both reference (blue) and cloak (red) with a batch of discrete coherence lengths. The path length distributions were obtained from diffusion equation simulations and from Monte Carlo simulations. The trend and the split of the curves confirm the experimental findings presented in Figure 4.7. The speckles on the front side of the cloak sample have a higher contrast than the speckles on the reference sample when illuminated with partially coherent light. Figure adapted from [82].

photons have to travel through three centimeters of PDMS that as a refractive index of 1.42. The big difference of the cloak sample in comparison to the reference sample is the bigger amount of shorter light paths. Thereby, the FWHM of the path length distribution is smaller for the cloak than for the reference sample.

Using the path length distribution $p(l)$ simulated by the Monte Carlo method for ray tracing, we can calculate the speckle contrast via Equation 4.5 with discrete coherence lengths within the same span of inverse coherence length that was examined experimentally. In addition, we also show the data obtained by the path length distribution simulated from diffusion equation, with and without absorption. The results of all simulations are presented in Figure 4.9.

In contrast to Figure 4.7, the speckle contrast reaches 100% for perfectly coherent light, whereas for finite coherence lengths, the trend of the simulations looks very similar to the trend of the experimental data. The speckle contrast of the cloak is consistently higher than the speckle contrast of the reference sample. The three different methods of path length simulation lead to almost the same speckle

contrast C_I .

Using again Formula 4.5, we can have a look at the extremes of the speckle contrast: For an infinite small variation of the frequency or in other words infinitely long coherence lengths, we find

$$l_{\text{coh}} \rightarrow \infty \quad C_I \rightarrow 1. \quad (4.6)$$

For very small coherence length, one can show that the width of the path length distribution Δs influences the speckle contrast like:

$$l_{\text{coh}} \rightarrow 0 \quad C_I \propto \sqrt{l_{\text{coh}}/\Delta s} \quad (4.7)$$

Not only does the limit in Equation 4.7 confirm the limit for incoherent light illumination with no difference in speckle contrast ($C_I^{\text{ref}} = C_I^{\text{clk}} = 0$) but it also confirms a difference in speckle contrast over a wide range of coherence length for samples with different widths Δs of their path length distributions.

4.3 CONCLUSION

With a simple experimental setup consisting out of a tunable laser, a microscope objective, a linear polarizer and a camera, we are able to scan over a wide range of coherence lengths and the connected statistics of the speckle patterns. We find no difference in speckle contrast for perfectly coherent light and thus no possibility to reveal the cloak with this approach. In good agreement to the theoretical simulations, we find a significant difference in speckle contrast between the reference sample and the cloak sample for partially coherent light. Even without knowing the complete path length distribution, we can reveal the diffuse-light cloak using partially coherent light and the contrast of the emerging speckles. This cannot be done solely for this specific cloaking device but, as carried out in Section 2.3, it is possible to uncloak all diffuse-light cloaks as they all have the same limit when it comes to transient cloaking or path length distributions respectively.

5 Chapter 5

EIGENCHANNEL ANALYSIS

In order to collect as many information of a scattering medium as possible, measuring the transmission matrix has become an established approach within the last years [87–91]. In principle, a perfect transmission matrix contains all scattering information about a scattering medium. It connects all possible vectors (position and angle) of input light to all possible vectors of complex transmitted light. By detecting the complex transmitted fields of light rather than the intensity of light, coherent interference effects can be predicted by a transmission matrix.

The goal in this chapter is to measure a transmission matrix for both the cloak and the reference sample and use the vast amount of information stored within these matrices to reveal the presence of the cloak. By successfully unclocking the cloak sample in this manner, the constrain discovered in Chapter 4, that the cloak cannot be reviled by perfectly coherent light (there with a static illumination), might be overcome by using several different illumination vectors and processing the data.

There are a couple of challenges along the way to realize this goal. First, in contrast to former measurements, the complex transmission of samples has to be recorded. To do so, an interferometric setup is built and the complex transmission can be reconstructed by a Fourier analysis of the interference of said transmission with a tilted reference beam. This basic idea is explained in more detail in Section 2.7.

Second, a perfect transmission matrix would require an almost infinite amount of individual illumination vectors to be recorded one after the other. To limit the amount of data and to make the setup as sturdy and simple as possible, we restrict the validity of the transmission matrix to a single position and vary only the angle of the input vector of light. This configuration can still be optimized to about 8000 independent illuminations that have to be recorded in order to construct a transmission matrix.

An additional challenge is to have a robust sample. The transmission matrix at one illumination point differs from the transmission matrix a little bit to the side. If the sample moves a little bit to the side after half of the measurement, the transmission matrix recorded would be a mix of the two original transmission

matrices. In order to prevent this kind of movement, the samples used in Chapter 4 are revised, as these soft PDMS samples tend to creep during the measurement as discussed in Section 4.1. The new samples are not only smaller by a factor of ten but also out of a hard resin in order to avoid any movement in the sample itself.

The last challenge is to find a significant difference between the respective transmission matrices. This is done by rewriting the transmission matrix into a diagonal form by performing a singular value decomposition (SVD) and subsequently analyzing the singular values of the resulting matrix [87].

The findings in this chapter are the result of a collaboration with the research group of professor W. Choi. As they are experts in the field of measuring transmission matrices [89, 92, 93], we got together with them to realize the ambitious project of measuring the transmission matrix of a diffuse-light cloak.

5.1 SAMPLE PREPARATION

Preparing new and improved samples to measure the transmission matrix is crucial as the PDMS-samples [81] used in Chapter 4 were already on the edge of being stable for a single illumination that takes less than a second. Ideally the new samples should be stable for hours. Hence, a less viscous host material instead of polydimethylsiloxane (PDMS) is desirable. But still, the material has to be transparent for the visible light, scattering particles should be easily dispersed in it, hence it should be castable.

All these requirements are met by the clear polyester resin “SKresin 2420 (TS)” by the company “S u. K Hock GmbH”. In addition to the increased temporal stability, the size of the samples is changed. It is a lot easier to handle smaller samples in an interferometric setup. For one thing the path length distribution $p(l)$, see Figure 4.8, is more narrow and thus small, unwanted deviations from perfect coherence do not affect the experiment. For another thing, the complex fields necessary to reconstruct the transmission matrix are measured in an interferometer. In the interferometric setup used, the samples need to fit in-between the illumination and collection microscope objective, which are separated by twice the working distance of the objectives. This imposes a further limitation on the sample thickness.

All in all, the sample host material is changed from PDMS to a resin and all dimensions of the samples are lowered to a tenth of the original size. In order to emphasize the quality of the new samples and to document the modified fabrication of these samples in contrast to the PDMS samples in [81], the individual manufacturing steps are pointed out in this section.

All three samples, the reference, the obstacle and the cloak sample consist of the same reference material in the surrounding. In order to stay in the same ballpark of about 5% transmission and to have the same l_t/a ratio (where a is the

thickness of the shell $R_2 - R_1$, see Chapter 3 and Section 2.3), the diffusivities and the corresponding transport mean free path lengths have to be lowered by a factor of ten. Hence the concentration of scatterers has to be increased by a factor of ten. In order to minimize imperfections in the concentration of the scatterers and to circumvent problems due to shrinkage during the curing process, first, 20 reference samples are cast in one manufacturing step. 100 ml of resin is mixed with 390 mg of Titania dioxide (TiO_2). This mixture is cast into a $15 \text{ mm} \times 80 \text{ mm} \times 80 \text{ mm}$ mold (see Figure 5.1). Out of the inner center of this big block, $5 \times 4 = 20$ small samples are milled out. These samples have a size of $L_x = 15 \text{ mm}$, $L_y = 8 \text{ mm}$ and $L_z = 3 \text{ mm}$. The samples were taken out of the middle of the big block in order to avoid possible inhomogeneities on the walls of the mold due to air bubbles or other imperfections. As a smooth surface is inevitable for meaningful measurements of the scattering properties of the insight of the samples, the surfaces have been polished by a diamond polishing mill. Otherwise, surface roughness effects would have led to scattering on its own and this effect would have disturbed further measurements.



Figure 5.1: Picture of the sample preparation. Left, one can see the aluminum cast to mold the big resin blocks. The resin (not depicted) is mixed with titanium dioxide (TiO_2). A pile of the powder is shown in the middle left of the picture. The big blocks are milled down to 20 reference samples. One of these is placed in the middle right. Right, a retainer is shown that is used to clamp and center the samples in order to drill vertical holes into them to process them to obstacle and cloak samples.

19 out of the 20 reference samples are further processed in order to fabricate the samples for cloak and obstacle. The remaining sample is the reference sample depicted in Figures 5.1 and 5.2. One of these 19 samples is processed in order



Figure 5.2: Picture of the three samples. Left, the reference sample out of a clear resin mixed with titanium dioxide (TiO_2). In the middle, the obstacle sample is shown that has the same surrounding as the reference but in addition a hole is drilled in the center of the xy plane. This hole is filled by a mixture of two parts of Titania and one part of resin. On the right, the cloak sample is shown. In addition to the obstacle, this sample has a shell around the inner cylindrical core. This shell is lower in TiO_2 concentration and thus guides the light around the strongly reflecting core of the sample. The dimensions are: $L_x = 15$ mm, $L_y = 8$ mm and $L_z = 3$ mm.

to become the obstacle sample. Therefore, it is clamped into the retainer shown in Figure 5.1 and a hole is drilled exactly in the middle of the xy -plane with a radius of $R_1 = 0.8$ mm. As the diffusivity of the core has to be lowered by a factor of ten as well, the ceramic material used as an obstacle in the samples of Chapter 4 cannot be used anymore. Here, the very same resin mixed with a very high amount of TiO_2 is used as a diffuse reflector in the samples. The core material is fabricated by mixing one part of resin with two parts of TiO_2 . After a lot of stirring this results in a very thick and viscous dough like material. This dough like material is formed to long cylindrical threads with a diameter of about 1 mm. One of these strings is threaded into the cylindrical hole of the obstacle sample. Next, as much of the core material as possible is pushed into the hole of the sample to fill it completely. After 12 hours of curing time, the obstacle sample is finished and it is depicted in Figure 5.2.

The remaining 18 unprocessed reference samples are destined to become cloak samples. As the correct ratio of concentration of scatterers in the surrounding in contrast to the shell is crucial, the remaining 18 samples are used to optimize the ratio between the two concentrations. Just as the obstacle sample, the cloak samples are clamped into a retainer in order to drill a centered hole into the sample. The hole for the cloak samples has a radius $R_2 = 1.2$ mm. Hence the remaining thickness of the surrounding is only 0.3 mm and thus, the center points

of the samples have to be met very precisely. This hole is then filled with the shell material. As already discussed in Chapter 3, the theoretically calculated ratio of concentrations (see Equation 2.10) of $D_0/D_2 = N_{p,2}/N_{p,0} = 2.7$ does not lead to perfect cloaking. Instead, an increased ratio of about 3.9 leads to the desired light propagation and hence perfect cloaking [81]. With this knowledge in mind, an optimal ratio of 4.1 in the concentration of the two areas is found for the cloak sample (optimized for homogeneous illumination). Optimization for point like illumination leads to an even higher contrast of 4.6.

The resin for the shell material is mixed with the corresponding amount of TiO_2 and poured into the drilled hole in the middle of the sample. After 12 hours of curing time, the hole for the core is drilled into the cloak sample. Next, the procedure is the same as for the obstacle sample described above. After a final curing step, the cloak sample is finished and can be seen in Figure 5.2.

5.1.1 Sample Characterization and Optimization

The performance of the samples under homogeneous illumination and under point like illumination is displayed in Figure 5.3. Homogeneous white light illumination from the back side is shown in the upper row of pictures. The pictures show a part of the front side of the sample. The dashed lines indicate the area from 25% to 75% of height and width of the samples. In this area edge effects play only a minor role. The average transmission of the samples in dependence on the x -axis is displayed by a solid white line. For the reference the transmission is almost unity in this area indicating that light leaking to the sides, as well as to the bottom and top plays only a minor role. The newly designed core of the obstacle sample casts a pronounced shadow onto the front side of the sample and the transmission drops down to about 50% in the middle of the sample. The cloak 1 sample almost perfectly resembles the behavior of the reference sample. There is only a minor asymmetry that might occur due to a small misalignment in x -direction when the two holes were drilled into the sample. The second cloak sample transmits to much light under homogeneous illumination, as it is optimized to the point like illumination.

In the second row of Figure 5.3, under point like illumination, the reference transmits a Gaussian shaped spot onto the front side of the sample [46]. The shadow on the front side of the obstacle sample is even more pronounced compared to the homogeneous illumination. The local minimum in the middle of the solid white line, that averages in y -direction over the area limited by the dashed lines, is at about 35% of the corresponding transmission of the reference sample. As expected, the performance of the core-shell cloaks is not perfect under point like illumination [41]. For cloak 1, the amount of light that is transmitted is

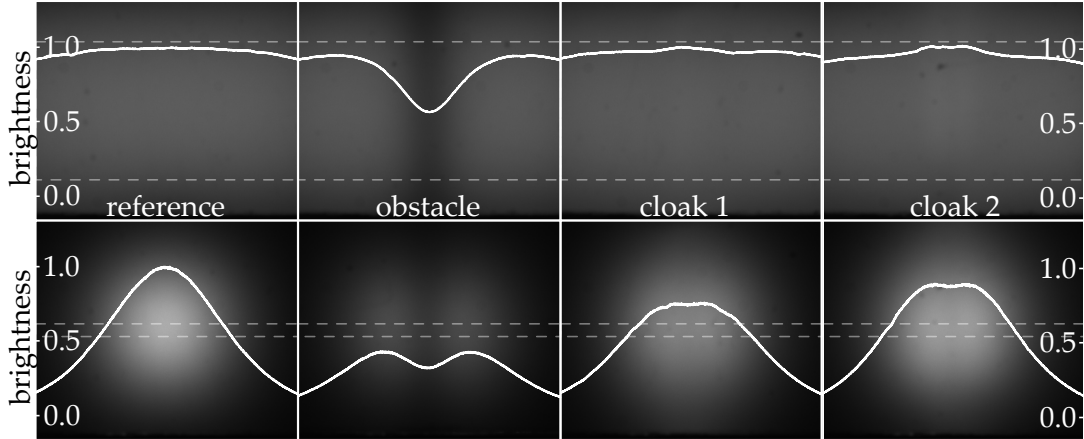


Figure 5.3: White light characterization of the samples under homogeneous illumination (top) and point-like illumination (bottom) from the rear side of the samples. In the background, photographs of the samples are shown. The regions of interest (marked by dashed white lines) are centered on the front side of the samples and cover 50% of the width and 50% of height for homogeneous illumination and 5% of height in the case of point like illumination. The solid white lines correspond to the average brightness of the region of interest over the height of the region of interest. For homogeneous illumination, the reference sample has an almost homogeneous transmittance. The strongly scattering core of the obstacle leads to a shadow on the front side with only about 50% brightness. Cloak 1 performs quite good for homogeneous illumination, as the white line is almost flat and reaches the same brightness level as the reference. The shell of cloak 2 transmits too much light and hence, under homogeneous illumination, there is a small peak in the white curve. Point like illumination leads to a Gaussian-like shape of brightness on the front surface of the sample for the reference. The impact of the core is even bigger under this illumination, as the obstacle sample transmits only about 35% of light in contrast to the reference. Cloak 1 transmits the same amount of light as the reference, but the distribution is different. While cloak 1 transmits more light at side of the center, the middle of the cloak 1 sample is too dark. The overall transmission of cloak 2 is too large but only looking at the middle of the cloak sample, the performance of cloak 2 is much better than the performance of cloak 1.

the very same as for the reference sample but the distribution is different to the reference. The peak intensity is at only about 75%. In the following experiments this flaw would not play a role as the transmission of the samples is normalized and hence the absolute transmission is not taken into account. In addition, the observed area on the front side will be very small, hence the shape of the light distribution is negligible as well.

With the set of samples costing out of the reference sample, the obstacle sample and the cloak 1 sample, the samples used in Chapter 4 [81] are recreated and optimized. To further optimize the cloak sample to the point like illumination and

detection in this chapter (see Figure 5.5), cloak 2 has a lower concentration of TiO_2 in its shell. As cloak 2 is optimized for point like illumination and detection only at the middle of the sample, the peak of the light distribution at the front side of this sample is almost one. In the following experiments, only cloak 2 will be used and called cloak.

5.2 INTERFEROMETRIC SETUP

To measure the complex transmission field of the samples in order to construct a transmission matrix, an interferometric setup has to be built. This setup, depicted in Figure 5.4, has to fulfill a couple of requirements.

First of all, the setup has to provide two light paths of a coherent light source and a detection camera in order to measure the tilted interference described in Section 2.7. The two light paths have to be about the same length in order to maximize the interference potential. This requirement was met by a Laser (Toptica, DL 100, $\lambda = 780 \text{ nm}$, $l_{\text{coh}} \geq 60 \text{ m}$), a CCD camera (Point Grey, BFLY-PGE-50H5M-C, 2448×2048 pixels) and two beam splitter cubes that first divide the illumination in two separate arms and later join these arms again. Note that both beam splitters have a ratio of 10% transmission to 90% reflection. Thereby, the light loss due to the scattering samples in the sample arm is accounted for and both arms of this interferometric setup will have the same intensity on the camera chip. For fine adjustments, a rotational ND filter in the reference arm can be used. To induce a tilt angle between the two light paths, the components in the reference arm are elevated (out of the plane in Figure 5.4) about 1 cm in order to hit the camera with an incline. This corresponds to a tilt angle in y -direction. The tilt angle in x -direction can be changed by rotating the second beam splitter cube. Furthermore, the collimated reference beam passes through a telescope in order to increase the beam diameter to illuminate the entire camera chip. In theory, the light passing through the reference arm should be a plane wave. By adjusting the distance of the telescope lenses, the wavefront is optimized and monitored by measurements using a wavefront sensor. To increase the beam quality, a pinhole is mounted between two lenses in order to clean the mode and beam profile of the laser. Just as in Chapter 4, a linear polarizer is mounted right in front of the camera to increase the speckle contrast.

The second requisite is the possibility to change the illumination of the sample in a fast and convenient way. As carried out in the beginning of this chapter, we decided to change the illumination by varying the angle of the illumination. Using a 2D mems mirror (Mirrorcle Technologies Inc., A5M24.2-2400AL-TINY20.4) is a very convenient way to tilt the illumination in both x and y -direction. The diameter of the mirror is limited to 2.4 mm as we are using an integrated mirror,

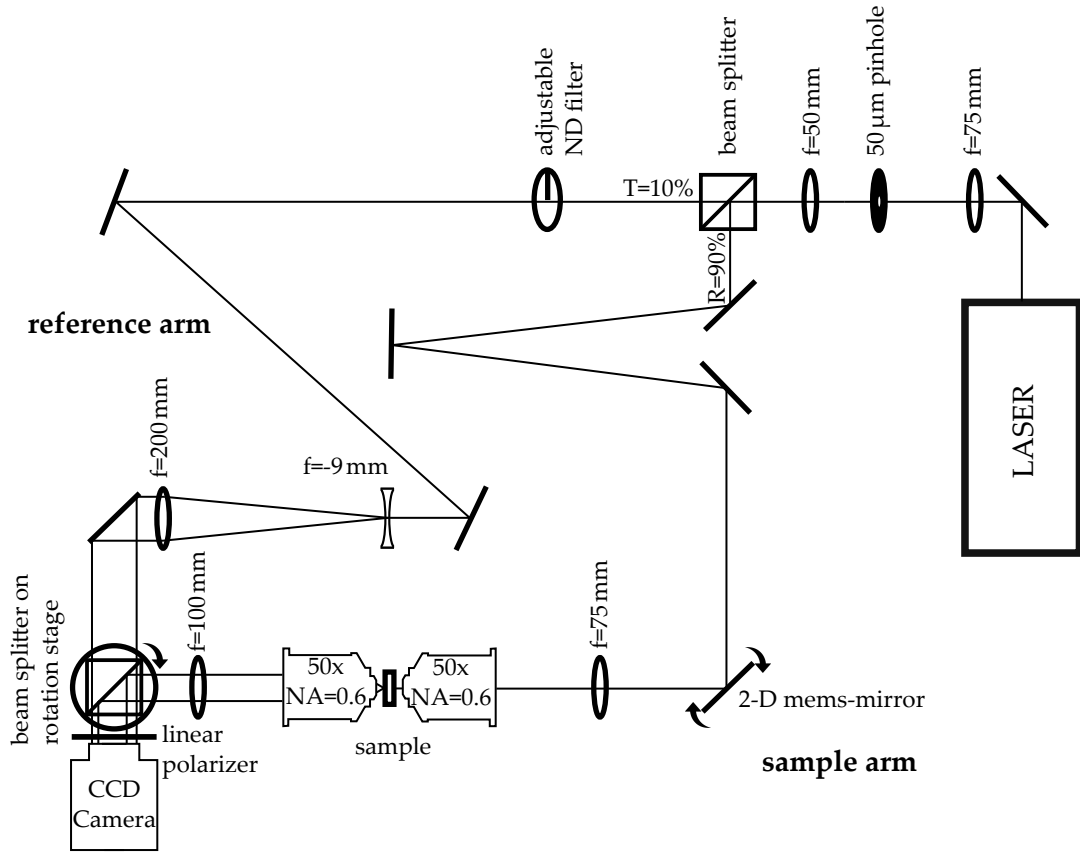


Figure 5.4: Sketch of the experimental setup. The laser beam (Toptica, DL 100, $\lambda = 780\text{ nm}$, $l_{\text{coh}} \geq 60\text{ m}$) is cleaned by a $50\ \mu\text{m}$ pinhole and then split into the two arms of the interferometer by a beam splitter ($R = 90\%$, $T = 10\%$). In the reference arm (upper left), the beam intensity can be regulated by an adjustable ND filter. Via two mirrors, the height of the reference beam is risen by 1 cm . Next, the beam is widened in order to illuminate the hole camera chip. By another mirror, the slope of the beam is changed to hit the camera at an angle on the original beam height. After a detour introduced by three mirrors to match the path length of sample arm and reference arm, the light going through the sample arm hits the 2D mems mirror. After passing through a lens and the illumination objective (Leitz Wetzlar, $\infty/0$, $50\times/0.6$), the sample beam hits the sample. The transmitted light is collected by a second objective (same type as illumination objective) and after passing through a second lens, a beam splitter ($R = 90\%$, $T = 10\%$) on a rotation stage reflects most of the light onto the camera.

because its pivot point is just underneath the reflecting surface. This is quite crucial as this prevents the setup from defocusing for bigger angular changes. This mirror is able to scan in very small and fast steps, in other words, the precision of the mirror is not the limiting factor for angular resolution. The illumination setup of the sample arm is covered in more detail in Section 5.2.1.

As a last requirement, the measurement setup has to be as stable as possible in time and as sturdy as possible in terms of environmental influences. To achieve this, the setup itself is built on a breadboard on an air damped optical table and all components are mounted on thick posts as close as possible to this breadboard resulting in a beam height of 52 mm. In addition to this, an enclosure is built around the entire setup to block light and air flow that might influence the measurement. To further decrease environmental influences, most measurements were performed over night. Just as the measurements in Chapter 4, the results were confirmed by repeating all measurements several times.

5.2.1 Sample Illumination

The big challenge of this setup is to realize as many independent illuminations as possible, as with more illuminations, the transmission matrix contains more and more information. Figure 5.5 shows the lower part of the setup once again in more detail. Two exemplary beam paths are illustrated in blue and red, each corresponding to a different tilt angle of the mems mirror. The arrangement of the lenses and objectives leads to two $4f$ systems. To explain the path of light in detail, first a single angle of the mems mirror and the resulting foci are reviewed, then the behavior of light for different tilt angles is discussed.

Considering only one tilt angle of the mems mirror (e.g. the beam depicted in red), on the right side of Figure 5.6 the pivot point of the movable mems mirror is at the same time the focal point of the $f = 75$ mm lens next to it. This lens focuses the previously collimated beam onto the back focal plan (BFP) of the illumination objective. The right objective, that illuminates the sample diffracts the focused beam from its BFP to a collimated beam, that points towards the sample front side. Together, the lens and the objective act as a telescope that decreases the beam width by a factor of 15. Hence the illuminated area in the sample plane is about $100\ \mu\text{m}$ in diameter. Without any sample, the focal planes of the two objectives are the same and hence, the detection objective focuses the collimated beam onto its back focal plane. The second lens ($f = 100$ mm) completes the second $4f$ system with its front focal plane lying within the back focal plane of the second objective and its rear focal plane lying on the camera chip.

Considering the sheaf of beams emerging by different tilt angles of the mems mirror, they are all well collimated and at the same center position at the mirror. The increasing lateral displacement induced by different tilt angles is converted to a constant lateral displacement by the $f = 75$ mm lens. For different tilt angles, the sample beam hits the back focal plane of the first objective at different positions, that correspond to different illumination angles at the sample surface. This tilt is once again converted to a constant lateral displacement by the second objective

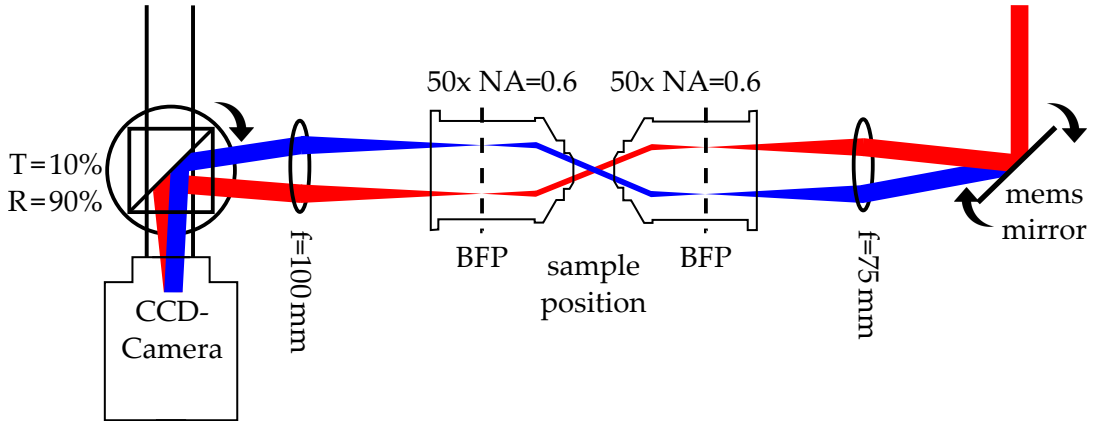


Figure 5.5: Sketch of the sample illumination. This sketch illustrates the sample illumination already shown in Figure 5.4 in more detail. There is a $4f$ imaging system between the mirror and the sample plane and another $4f$ imaging system between the sample plane and the camera. At the mems mirror, the beam is collimated and centered in the optical axis. By tilting the mems mirror to another angle, the following beam paths change. Two of these beam paths are illustrated in red and blue. At the $f = 75$ mm lens, both beams are still collimated but they are off center. At the back focal plane (BFP) of the first objective, both beams are focused and parallel to the optical axis. At the sample plane, both beams are collimated and centered at the middle of the optical axis. In the case of no sample, the two beams are collected by the second objective and once more individually focused in its BFP. Another lens refracts the beams onto the camera chip where they hit the same spot but under a different angle. By rotating the beam splitter in front of the camera, the tilt between the sample arm light and the reference arm light can be adjusted.

and furthermore converted back to a (smaller) tilt by the $f = 100$ mm lens. All illumination angles (without any sample) hit the camera at the same position but with different incident angles.

Recording a transmission matrix demands as many independent illuminations as possible [87]. As in this experiment, we restricted ourselves to varying the angle of the illumination, we have to make sure, that the illumination angles are well separated. This angle separation can be checked intuitively in the BFP of the illumination objective. Well separated foci in the BFP correspond to well separated illumination angles on the sample front surface.

To confirm the independence of each illumination angle, an additional pre-experiment is performed. Without any sample, $N = 7845$ different illumination angles are recorded. In order to minimize the influence of the tilt angle to the transmission, not the complete aperture and hence not the complete NA of the objective $NA = 0.6$ but rather only $NA \approx 0.4$ is used. This illumination setup leads to a angular range from -23.5° to $+23.5^\circ$ in both x and y -direction. Within this span of 47° , 100 individual illumination angles are driven by the mems mirror.

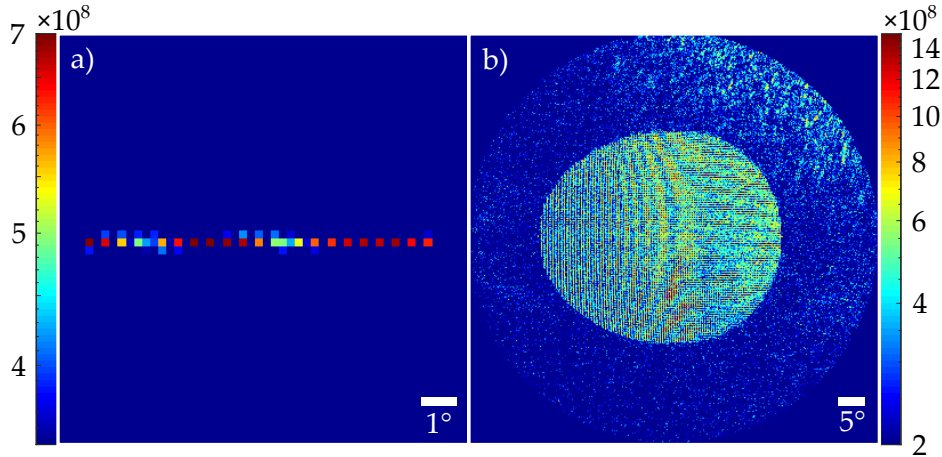


Figure 5.6: Summed up magnitude of the Fourier transform to check angle separation. As explained in Section 2.7, a region of interest in the Fourier plane is shown. To check whether the individual illumination angles overlap, Panel a) shows 21 subsequent illumination angles with an angular spacing of 0.47° . As the peaks (only individual pixels) are separated, the angles at the sample plane are clearly distinguishable. Panel b) shows all 7845 angles in an add-up picture of the Fourier plane with the same angular spacing of 0.47° in both x and y -direction between neighboring angles. The brighter area in the upper right corner arises due to the fact, that in this direction the $(0,0)$ peak of the Fourier plane is located. By adding up constant stray light artifacts, these areas sum up to magnitudes of nearly the same order as a single measurement peak.

Combining these angles in x and y -direction leads to a total of 7845 angles.

Recording the back focal plane directly is impossible without moving the objectives, hence the separation of the focal points and the angles respectively is checked via the field in the camera plane. Performing a Fourier transformation onto a picture taken with no sample in the setup leads to a small peak in the Fourier plane that resembles the tilt angle between the reference beam and the sample beam. This procedure is outlined in more detail in Section 2.7. For two perfect plane waves, the peak in the Fourier plane will be infinitesimal small.

Adding up the experimentally measured and Fourier transformed pictures of 21 illumination angles with varying x -angle leads to the picture depicted in Figure 5.6, Panel a). Note, that only the magnitude of the complex numbers is shown. The difference in illumination angle is $47^\circ / 100 = 0.47^\circ$.

The individual illumination angles are well separated from each other, hence the angular spacing of about 0.47° is sufficient to create independent illuminations. Recording images for all $N = 7845$ angles and adding up the magnitude of the resulting Fourier transformed pictures results in the picture depicted in Panel b) of Figure 5.6. Panel b) shows a cutout of the lower left Fourier plane

(compare Figures 2.11 and 5.7). The outer circle corresponds to the full NA of the detection objective. The reduced illumination NA is clearly visible as the circle of illumination does not reach the outer borders of this cutout. In addition, a deviation of the expected circular shape of the illumination angles is visible. Most likely this occurs due to a minor alignment flaw of the two objectives. Here, not using the full NA ensures that all light is picked up, even with small flaws like this. The brighter region on the upper right of the Panel b) in Figure 5.6 is connected to some constant coherent light that is part of a tail of the center maximum of the Fourier plane and adds up over the measurement series.

The result in Figure 5.6 confirms that we succeeded in installing a setup that is capable of illuminating a sample with about 7845 independent illumination angles. This is the starting point for measurements on the reference and the cloak sample.

5.3 COHERENT ANALYSIS

With the experimental setup ready, the samples developed can be placed in the designated position between the two objectives. As the calibration of the setup is very sensitive, the 4f system on the detection side is not moved to image the back side of the sample. Like this, the calibration that is checked by a measurement without any sample is still intact. Although imaging the rear side of the samples would be the intuitive way to collect light, the fact that the speckle statistics do not change by imaging another plane of the sample enables us to keep the original setup as it is. The goal for the following experiments is to find possible differences between the cloak and the reference, hence only these two samples are measured in the setup.

In the following, a short explanation of the processing of the pictures taken is shown. For a more general introduction with less complex samples, read Section 2.7.

Placing the reference sample into the setup with its front surface (xy -plane) at the working distance of the illumination objective leads to an illumination spot on its front surface that does not move for different angles. An exemplary image that is recorded by the CCD camera is shown in Figure 5.7, Panel a). The recorded image shows the speckles emerging from the reference sample. In the magnified area, one can see that the speckles are resolved, as they have a size of about 10 pixels in x and in y -direction. In addition, one can see the diagonal stripes, originating from the tilt angle between the reference beam and the sample beam, from the upper left to the lower right. As mentioned in Section 2.7, for samples as complex as this, it is hard to see a deviation in the striped pattern that would indicate a change in phase of the sample light.

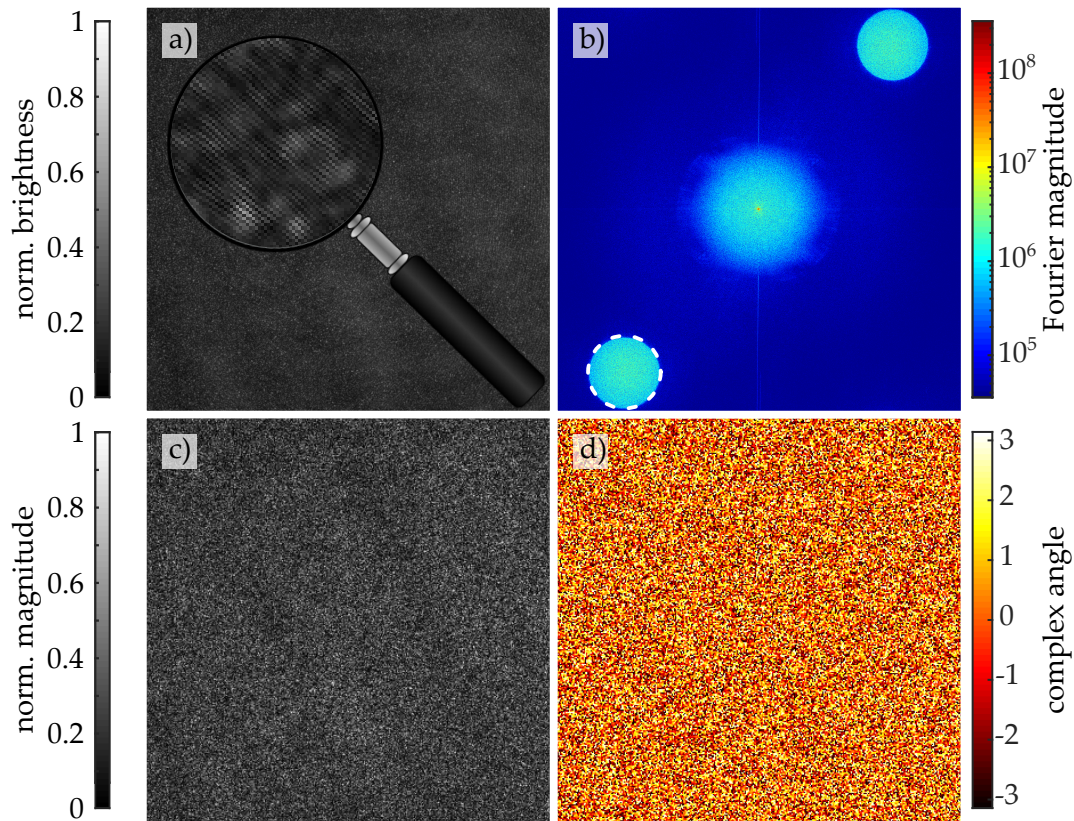


Figure 5.7: Exemplary picture analysis. Panel a) shows the raw camera picture with a magnified area. The coherent interference forms speckles on the camera chip. These speckles are superimposed by a striped pattern that originates from the tilt between reference arm and sample arm. The random phase of the speckles bends the otherwise straight lines. Performing a fast Fourier transformation (FFT) on this image leads to a complex Fourier image. The magnitude of this image is displayed in Panel b). Interference of the reference arm with itself leads to a bright spot in the middle at $(0,0)$, the interference of the sample arm with itself leads to the round spot in the middle of the plane. Due to the tilt angle between the two light arms, the interference of the reference beam with the sample beam is found in the lower left and upper right corner of the Fourier plane. The region of interest (marked by a dashed white line) is limited by the NA of the second objective. Cutting out the marked region of interest and performing an inverse fast Fourier transformation (IFFT) yields to a complex speckle image. The magnitude of this image is shown in Panel c) and the complex angle of this image is shown in Panel d).

Panel b) shows the shifted fast Fourier transform (FFT) of the picture recorded and shown in Panel a). The $(0,0)$ position is shifted to the center of the picture. Here, the superposition of the interferences of the two light paths with themselves is found. The plane wave of the reference beam by itself leads to a bright red peak

in the very center of the FFT, as there is no tilt at all. The light passing through the sample arm by itself causes the big round spot in the middle of the FFT. As all angles of light that pass through the detection microscope might interfere with each other, a maximal tilt angle of $2 \times \text{NA}$ between the interfering waves is possible. Hence the spot in the middle has quite a large radius compared to the outer circular spots. These spots emerge from the interference between the reference beam and the sample beam. The angle between the reference beam and light traveling through the sample arm is always the tilt angle plus the angular variation of the transmitted light through the sample (limited by the NA of the objective). This limitation leads to a rather sharp border of the circular areas in the upper right and the lower left with their radius corresponding to the NA of the objective.

To only process the information that emerged from the interference of the reference beam with the sample beam, the circle marked by a dashed white line in the lower left of Panel b) of Figure 5.7 is cut out and shifted to the center of the Fourier plane. An inverse fast Fourier transformation of the cut out and shifted region results in a speckle picture with a decreased resolution (originally $n_x^{\text{orig.}} \times n_y^{\text{orig.}} = 2448 \times 2048$ pixels to $n_x^{\text{comp.}} \times n_y^{\text{comp.}} = 361 \times 361 = 130321 = M$ pixels). Although the resolution is decreased by a factor of about six in both dimensions, the speckles are still resolved, as their average original size was larger than six pixels.

The resulting complex image is displayed in Panels c) and d) of Figure 5.7. The magnitude of the complex numbers is plotted in Panel c), the angle of the complex numbers is displayed in Panel d). This resulting complex picture is a measure for the complex field transmitted through the sample.

5.4 TRANSMISSION MATRIX AND EIGENCHANNELS

5.4.1 Singular Value Decomposition

In order to construct a transmission matrix, a series of pictures had to be recorded and processed. To decrease the amount of memory used by this procedure, the processing described in Section 5.3 is done on the fly while the mirror is moving to the next position. The process of taking a picture, evaluating the steps described above in order to acquire the complex picture and moving the mirror to the next position takes about 0.9 seconds. This leads to a total measurement time of about two hours.

For reasons of clarity and comprehensibility, each 361×361 pixel complex picture is stored in a single column vector T^i (1×130321) with the length of the number of pixels $M = n_x \times n_y$. To built up the transmission matrix these complex

“vector-pictures” are stored side by side to form the transmission matrix \vec{T} .

$$\vec{T} = \begin{pmatrix} T_1^1 & T_1^2 & T_1^3 & \dots & T_1^N \\ T_2^1 & T_2^2 & T_2^3 & \dots & T_2^N \\ T_3^1 & T_3^2 & T_3^3 & \dots & T_3^N \\ \vdots & \vdots & \vdots & \ddots & \vdots \\ T_M^1 & T_M^2 & T_M^3 & \dots & T_M^N \end{pmatrix} \quad (5.1)$$

$\xleftarrow{N=7845 \text{ columns}}$
 $\xrightarrow{M=130321 \text{ rows}}$

The marked column correspond to the first complex picture calculated. There are $N = 7845$ columns and $M = 130321$ lines in this matrix. The huge matrix \vec{T} contains all the information that is collected. As it stores the complex field information, this matrix might be used to predict the transmission of the superposition of two illumination angles that were measured in this experiment. But as the information is not sorted yet, it is hard to extract information about the scattering properties of the samples.

To sort the information gathered, we perform a singular value decomposition (SVD) [94, 95]. A SVD splits a matrix into a unitary rotation matrix \vec{U} , a rectangular diagonal matrix $\vec{\sigma}$ and the conjugate transpose of another unitary rotation matrix \vec{V} :

$$\vec{T} = \vec{U} \vec{\sigma} \vec{V}^* \quad (5.2)$$

Just as a the eigendecomposition of a matrix finds the eigenvalues and the eigenvectors, in the singular value decomposition, one finds the singular values and the singular vectors. A set of a singular value and a singular vector is called eigenchannel. The singular vectors are located in the rotation matrices \vec{U} and \vec{V}^* and the singular values are located on the diagonal of the matrix $\vec{\sigma}$. To give reason for the next steps of the evaluation, the individual matrices are annotated

in more detail:

$$\vec{U} = \begin{pmatrix} U_1^1 & U_1^2 & U_1^3 & \dots & U_1^N & \dots & U_1^M \\ U_2^1 & U_2^2 & U_2^3 & \dots & U_2^N & \dots & U_2^M \\ U_3^1 & U_3^2 & U_3^3 & \dots & U_3^N & \dots & U_3^M \\ \vdots & \vdots & \vdots & \ddots & \vdots & \ddots & \vdots \\ U_M^1 & U_M^2 & U_M^3 & \dots & U_M^N & \dots & U_M^M \end{pmatrix} \quad (5.3)$$

130321 columns

130321 rows

The unitary matrix \vec{U} is the matrix connected to detection and it has a size of $M \times M \approx 17 \cdot 10^9$ entries. The physical meaning of the individual columns with a length of $M = 130321 = 361 \times 361$ is revealed when these singular values are reshaped. The marked vector in Equation 5.3 of the reference sample is shown in Panel a) of Figure 5.8 and corresponds to the expected transmission pattern of the first eigenchannel. Any j -th column is normalized by $\sum_{i=1}^M |U_i^j|^2 = 1$. Starting from the left, only N vectors have said physical meaning, all entries $U^{j>N}$ contain only numerical artifacts.

$$\vec{\sigma} = \begin{pmatrix} SV_1 & 0 & 0 & \dots & 0 \\ 0 & SV_2 & 0 & \dots & 0 \\ 0 & 0 & SV_3 & \dots & 0 \\ \vdots & \vdots & \vdots & \ddots & \vdots \\ 0 & \dots & 0 & SV_N & 0 \\ 0 & \dots & 0 & 0 & 0 \\ \vdots & \vdots & \vdots & \vdots & \vdots \\ 0 & \dots & 0 & 0 & 0 \end{pmatrix} \quad (5.4)$$

7845 columns

130321 rows

The diagonal matrix $\vec{\sigma}$ contains the singular values SV_i . It has $N = 5845$ columns and $M = 130321$ rows. But only the diagonal elements contain nonzero numbers. Hence all rows below the N -th row are only filled with zeros. The rest of the matrix is filled with zeros as well. $\vec{\sigma}$ is connected to \vec{T} via the normalization

$$\sum_{i=1}^N |SV_i|^2 = \sum_{i=1}^N \sum_{j=1}^M |T_j^i|^2. \quad (5.5)$$

The singular values are all real positive numbers and they are sorted by their value. The largest singular value SV_1 is marked and corresponds to the other marked singular vectors in \vec{U} and \vec{V}^* . The singular values of several measurements are depicted in Figure 5.9.

$$\vec{V}^* = \begin{matrix} & \xrightarrow{7845 \text{ columns}} \\ \begin{matrix} \uparrow \\ 7845 \text{ rows} \\ \downarrow \end{matrix} & \left(\begin{array}{cccc} V_1^1 & V_1^2 & V_1^3 & \dots & V_1^N \\ V_2^1 & V_2^2 & V_2^3 & \dots & V_2^N \\ V_3^1 & V_3^2 & V_3^3 & \dots & V_3^N \\ \vdots & \vdots & \vdots & \ddots & \vdots \\ V_N^1 & V_N^2 & V_N^3 & \dots & V_N^N \end{array} \right) \end{matrix} \quad (5.6)$$

\vec{V}^* is the illumination matrix. Just as \vec{U} , it is a square unitary matrix that consists of singular vectors. The individual rows with a length of $N = 7845$ correspond to the number of illumination angles. The \vec{V}^* matrix is a kind of recipe as the singular vectors in this matrix describe the illumination. This illumination is connected to the transmission that is stored in the $\vec{\sigma}$ matrix and the transmitted pattern stored in \vec{U} . The normalization of every j -th row reads as $\sum_{i=1}^N |V_i^j|^2 = 1$.

5.4.2 Singular Vectors

Figure 5.8 shows the marked complex, reshaped vectors of \vec{U} and \vec{V} . As these vectors are connected to the first singular value SV_1 , which is the largest singular value in $\vec{\sigma}$. These pictures show the situation for one would get the highest transmission, if one would seek a way to increase the transmission of the sample.

Rearranging the singular vectors into a 2D form facilitates the understanding of the physical meaning of the vectors. The rows in matrix \vec{V}^* can be rearranged to a circular shape just as the illumination angles on the sample surface or at the mems-mirror were driven. The complex vector then can be split into its magnitude (see Figure 5.8 upper left) and its complex angle (see Figure 5.8 lower left). Reading this vector as a recipe, the magnitude fixes the partial intensity per illumination angle and the complex angle fixed the additional phase every illumination angle has to have while illuminating the sample.

The column vectors of the \vec{U} matrix can be reshaped into complex square 361×361 images. These images predict the complex field at the camera when the sample is illuminated by the corresponding illumination given by \vec{V}^* . As the goal of this work is to find out whether there is a difference in the statistics of the eigenchannels of the reference and the cloak sample, this route of controlling the light via the eigenchannels [93, 96, 97] is not perused any further.

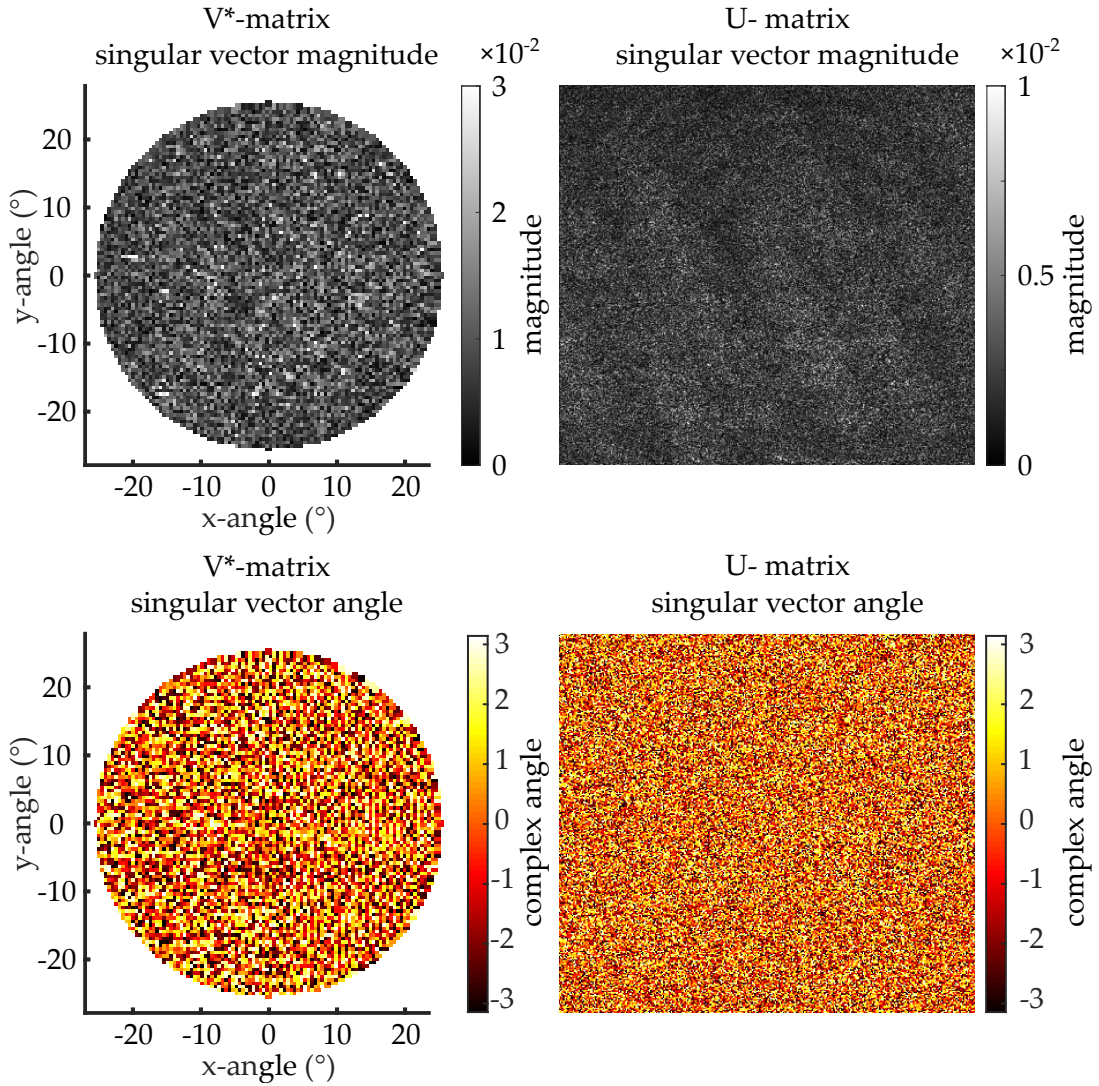


Figure 5.8: 2D notation exemplary complex singular vectors. The left row shows the first row of the \vec{V}^* matrix of the reference sample, rearranged into the shape the illumination angles were driven by the mems-mirror. The upper picture shows the magnitude of the picture, the lower panel indicates the angular phase for each of the illumination angles. On the right side, the first row of the \vec{U} matrix is displayed. The 130321 entries are reshaped into a 361×361 square picture. The upper panel shows the magnitude, the lower panel shows the complex angle.

5.4.3 Singular Value Distributions

As the square of the singular values corresponds to the transmission of the expected illumination situation given by its singular vectors found in \vec{U} and \vec{V}^* , one can deduct expectations for the distribution of singular values in the case of

no sample: Without any sample and with independent illumination situations, the normalized singular values should all be unity. If they differ from one, that means, that a certain configuration of angles transmits more light than another configuration. Due to real life imperfections, there will always be a deviation from this constant transmission. Hitting the objective lens off-center will always decrease the transmission a little bit. As mentioned in Section 5.2.1, the individual illumination settings are clearly distinguishable but they still have a small overlap. Last but not least, small variations in the laser intensity will directly be visible in the distribution of the singular values as well. If the laser intensity drops down to 95% for one second, the algorithm will connect this to the currently illuminated angle. The prediction within the transmission matrix would say, that if one illuminates the same angle again, 5% of the light will be lost.

Figure 5.9 shows the distribution of singular values normalized to the mean of their square. Hence the overall average transmission does not enter this analysis at all. On the vertical axis the diagonal elements of matrix $\vec{\sigma}$, the singular values are plotted. On the horizontal axis the corresponding number of the row and column is plotted, hence the number of the eigenchannel. As the singular values in $\vec{\sigma}$ are sorted by size, the curve shown in Figure 5.9 is decreasing. The measurement with no sample between the objective lenses is depicted in blue and the measurements for reference and cloak sample are shown in red and yellow.

As expected, the singular values without sample differ from a theoretical flat 1. The reasons discussed above lead to values that are between 1.2 and 1.1 for the first 1000 eigenchannels and between 1.1 and 0.9 for the next 5500 eigenchannels. The last 1500 eigenchannels lead to singular values below 0.9. In comparison to the distribution of singular values of the reference and cloak sample, the singular values without sample are closer to a flat 1 and the curves are clearly distinguishable. The curves for reference and cloak sample are almost indistinguishable.

But in fact, the presented results are very reliable, since repeating the measurements yielded qualitatively and quantitatively similar results. This is illustrated nicely by standard deviations of the individual singular values that are on the order of the line thickness in Figure 5.9.

As the individual measurements are not visible and the confidence intervals are thinner than the line thickness in Figure 5.9, this intuitive way of presenting the singular values is not suitable for the purpose of distinguishing the cloak sample from the reference sample.

To not only demonstrate the repeatability of our results, but also the reproducibility, additional measurements at several nominally identical samples positions have been performed. The confidence intervals already mentioned are only a statistical method for the reliability to measure the same singular value again for the same sample. Samples that should behave nominally the same might still

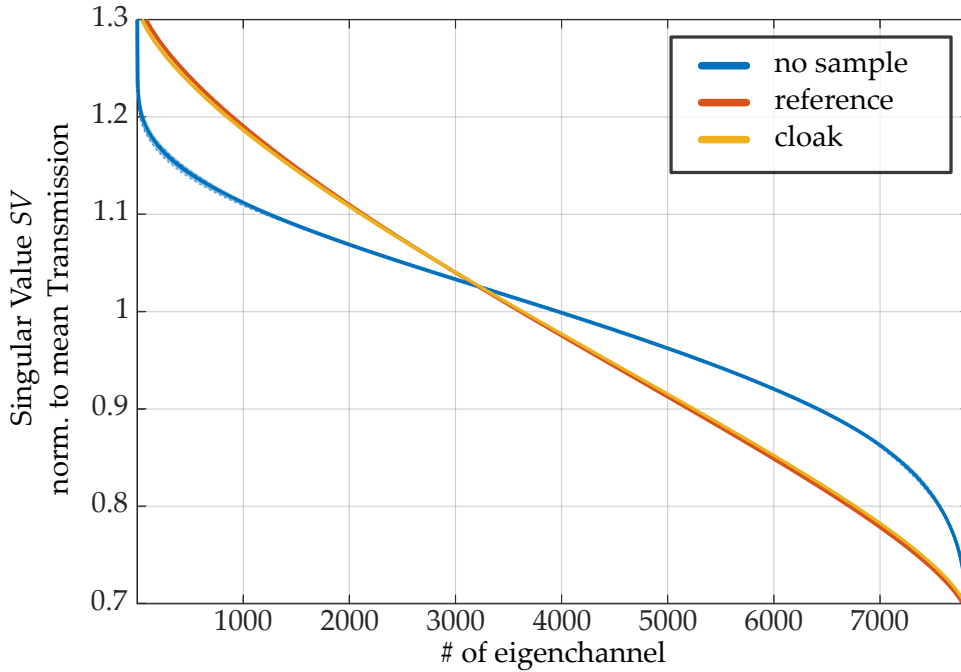


Figure 5.9: Normalized singular values measured and calculated for no sample, reference sample and cloak sample. The graph shows the 7845 singular values decomposed of the corresponding transmission matrices. The mean of the squares of the singular values is set to 1. Like this, all singular values above one indicate increased transmission and all singular values below one indicate lower transmission than average. The blue line indicating the “no sample” case is clearly distinguishable from the other two lines. The red (reference sample) and the blue (cloak sample) lines are almost indistinguishable. Every visible line is composed out of five to ten individual lines each representing a complete measurement. The average of the individual SVs is taken and the 90% confidence interval is shown as well.

differ more from each other due to fabrication imperfections. To get a measure for the difference in singular values for nominally the same but actually slightly different samples, the reference sample is moved by 3 mm to the side. More precisely, moving the sample to the side leads to an off-center illumination and, at the same time, an off-center detection. As the surrounding material of the cloak is the same as the material of the reference, also the shifted cloak sample is measured and expected to reproduce the behavior of the reference.

To better resolve possible differences between cloak and reference sample in the context of this eigenchannel analysis, the normalization of the singular values is changed. In Figure 5.11, all singular values are divided by the mean value of the reference singular values for every eigenchannel. This leads to a flat 1 for the

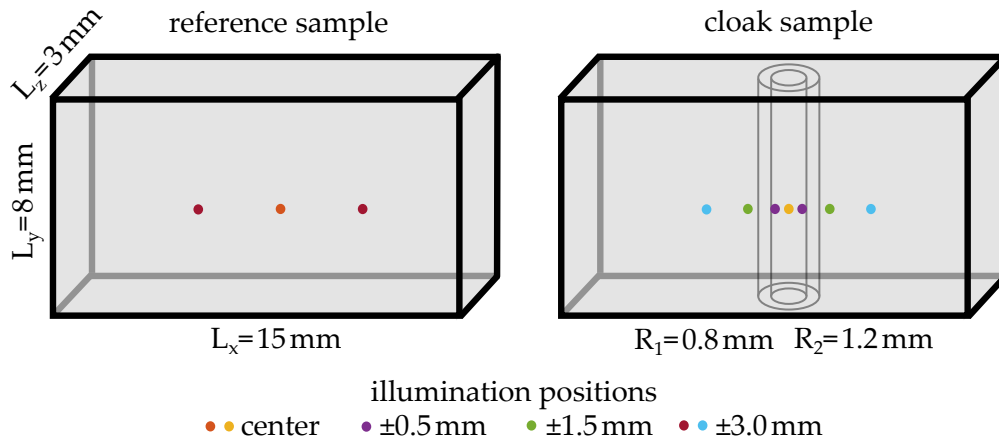


Figure 5.10: Sketch of the reference sample and the cloak sample with color coded illumination spots. The colors match the correspondent singular value lines in Figures 5.9 and 5.11.

mean of the reference sample itself and therefore, the small deviations between measurements at nominally identical become visible, but more importantly, also the differences between cloak and reference.

The information presented is the same as in Figure 5.9 with the additional measurements at the positions depicted in Figure 5.10. In Figure 5.11, only a small fraction of the singular values without a sample are shown, as the difference of these singular values is much larger than the difference between the cloak sample and the reference sample.

The measurements performed at the side of the reference sample (± 3 mm, depicted in dark red) and at the side of the cloak (± 3 mm depicted in light blue and ± 1.5 mm depicted in green) lead to almost the same singular values as the original centered measurement of the reference. Hence the difference between these four groups of measurements is a good measure of the uncertainty of measuring different references one after the other.

The yellow line indicating the singular values of the cloak is clearly distinguishable from the reference line and the singular values recorded at the side of the cloak sample. In addition to the centered illumination, the singular values measured at ± 0.5 mm of the cloak, depicted in purple, lead to an intermediate slope with respect to the two center measurements.

By changing the normalization of the singular values, it is possible to resolve deviations in the slope of the singular values in the order of 0.1%. Measuring singular values of the reference in the center and at the ± 3 mm position as well as measuring the singular values of the cloak at ± 1.5 mm and ± 3 mm all results in almost the same singular values. The experimental deviation of these measurements can be observed in the different slope of the curves. The difference

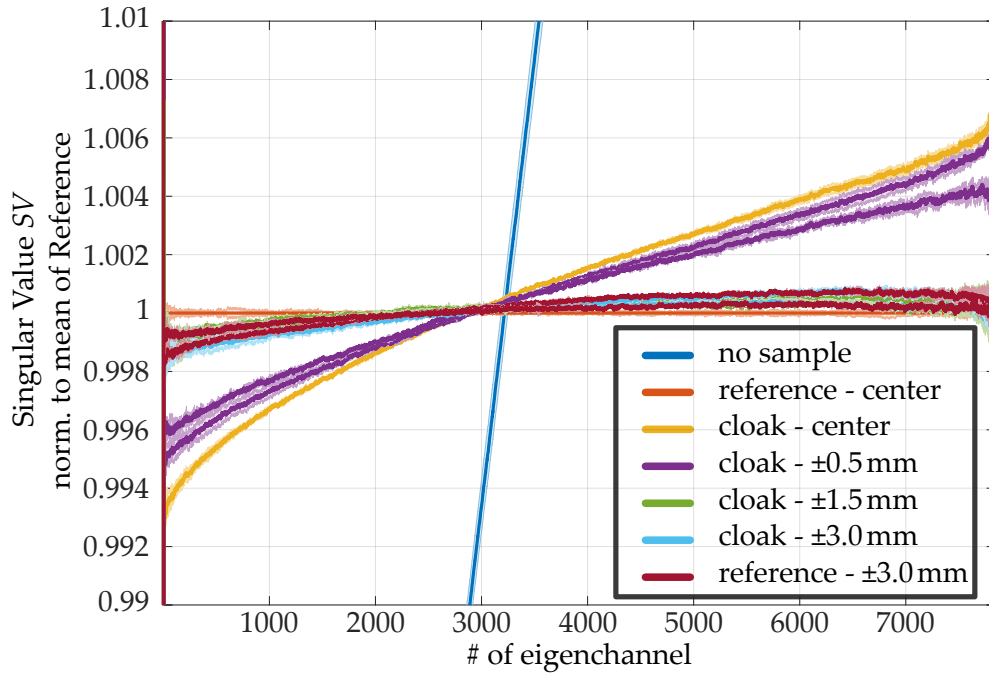


Figure 5.11: Representation of singular values normalized to the mean of the singular values of the reference measurement. To resolve the small difference between the singular values of the reference sample and the singular values of the cloak sample, all singular values are divided by the mean of the reference singular values. The blue “no sample” line is only visible in the middle of the graph, as its slope is far different from the two samples. All three measurements on the reference sample as well as the measurements on the cloak sample with ± 1.5 mm and ± 3.0 mm lead to almost the same distribution of singular values. All these results are found in the middle of the graph with almost no incline. The measurements on the center of the cloak within ± 0.5 mm lead to a higher slope in this representation.

in slope of the singular values for nominally identical references is only about 0.2%. This seems to be the maximal experimental accuracy of our method. Samples showing smaller slope deviations cannot be distinguished unambiguously.

To our surprise shifting the cloak to the side by 1.5 mm is enough to resemble the behavior of the reference although this illumination is centered only 0.3 mm next to the border of the shell (see Figure 5.10). Measuring the singular values at the center of the cloak sample yields to a different slope in singular values. The slope of the singular values measured at the center of the cloak is about 1% higher and hence clearly distinguishable from the measurements discussed before. Measuring the singular values at ± 0.5 mm at the cloak still leads to almost the same slope in the singular values as illumination at the center of the cloak does.

The first 50 and the last 100 singular values tend to deviate more from the average behavior than the rest of the singular values. Even within two series of

measurements on the same sample without moving it, the trend of these singular values deviates from each other. Reasons for this might be intensity fluctuations of the laser or even dust particles that float through the collimated laser beam. The singular vectors that correspond to the low singular values contain more of these low transmitting illumination angles. As position and the numbers of these angles changes from measurement to measurement, the trend of the singular value curves in this area changes as well.

Comparing the slope of the curves in Figure 5.11 one can differentiate three groups of measurements. First, the measurement without any sample. Second, the measurements of the cloak with an (almost) centered illumination. And third, the reference-like measurements performed on the reference sample itself and on the shifted cloak sample. As theoretical work on the behavior of these curves is still at an early stage and most of the publications are one- or two-dimensional samples [98, 99], we cannot tell for sure why the singular values of the centered cloak and the reference behave differently. Light passing through the middle of the cloak sample does not only travel on shorter paths than the light transmitting through the reference [39] but also undergoes fewer scattering events. Following these arguments, the trends depicted in Figure 5.11 are at least plausible.

Monte Carlo simulations (not depicted) revealed the fact, that light passing through the reference sample and exiting at the center position on the other side was scattered about 150 times. In contrast to that, light passing through the cloak sample is only scattered about 85 times.

The slope of the singular values seems to be connected to the amount of scattering taking place in the sample. No scattering leads to the blue line, indicating the no sample case. A high amount of scattering leads to the behavior of red line indicating the measurement on the reference and an intermediate amount of scattering events leads to an intermediate slope of the curve of singular values, the yellow line depicting the singular values of the cloak measurement.

In analogy to a game of pool one can relate to this behavior. The more intermediate bumps or reflections a billiard ball undergoes, the more small deviations in the incident angle change the outcome of the hit. As there are fewer scattering events happening in the cloak sample, the possible angle variation of an incoming beam for getting the same transmission should be a little bit bigger than for the reference as in the reference, more scattering events take place. This increased possible acceptance angle of the cloak leads to a slightly lower number of possible combinations of independent angles to build a very high or low transmission eigenchannel. Hence the singular values of the cloak have a flatter curve in Figure 5.9 that translates to a steeper curve in Figure 5.11.

This line of reasoning is only a preliminary explanation that would need more experimental and theoretical investigation.

5.5 CONCLUSION

Within this project, a new sample generation was developed and its features were fitted to fulfill the needs of this sensitive interferometric setup. Ten times smaller samples compared to Chapter 4 and [81] made it possible to perform interferometric measurements. A big benefit was the possibility to place the samples into the setup without realigning it. This was only possible thanks to the decreased thickness by a factor of ten. Using a hard resin made the samples more stable in time and simplified the overall handling of the samples.

Setting up a simple, rigid interferometric setup enabled us to measure the complex transmitted field of scattering media. Changing the illumination angle via a MEMS-mirror generated several thousand independent illumination scenarios on the scattering samples. Recording the transmission of these different illuminations leads to the complex transmission Matrix \vec{T} .

The singular value decomposition $\vec{T} = \vec{U}\vec{\sigma}\vec{V}^*$ arranged the information contained in the transmission in a more accessible way. Hence, a closer look at $\vec{\sigma}$ revealed the distribution of singular values associated to the transmission of the sample examined.

Comparing the distribution of singular values of the cloak sample with the distribution of singular values of the reference sample revealed a small but significant and reproducible difference between the two samples. In contrast to the findings under static illumination in Chapter 4, we found a possibility to uncloak the cloak sample by perfectly coherent light. Note, that this is only possible by changing the static illumination of Chapter 4 to a variable illumination in this chapter.

Chapter 6

6 CONCLUSIONS AND OUTLOOK

The goal of this thesis was to investigate the limits of cloaking in diffuse-light. With respect to this question, three major findings have been made within this work.

The basic concept of laminates in diffuse-light devices, that is used only in a minimal way by a core-shell cloak was examined in Chapter 3 in detail. Here, a 100 fold AB-laminate illuminated by an isotropic point source was simulated using the Monte Carlo method for photon transport in order to sweep over the complete transition regime between ballistic and diffusive light transport. The transmission and the laminate performance were measured while the amount of scattering per laminate layer was changed. Extensive simulation concluded in the finding, that there always has to be made a compromise between fine lamination, good laminate performance and high transmission through the device. On one hand, the core-shell cloak neglects fine lamination at all and hence only works for homogeneous illumination. Therefore, on the other hand, it benefits from decent laminate performance and high transmission. While it might have been intuitive in the start that with more complex laminate designs, one can push the cloaking performance further and further, my thorough study via Monte Carlo simulations clearly shows that increasing the number of layers around the core of the cloak would come at the cost of lower laminate performance or lower overall transmission. Additionally, the findings can serve as a basis for future designs for devices in light-scattering media. Using the information obtained by this study, guidelines for increased laminate contrast in order to meet the wanted effective properties can be deduced.

Putting the core-shell cloak to test with coherent illumination in Chapter 4 revealed an additional feature of the cloak, as perfectly coherent light does not reveal the cloak under static illumination. The evaluated speckle contrast was unchanged when comparing the reference sample to the cloak sample. While intuitively this might be obvious, the original theoretical design does not take the wave properties into account, thus making this a very important analysis. In the same way, however, the finite coherence length properties have not been considered when designing these cloaks. Experimentally I demonstrated, that by

decreasing the coherence length of the illumination the presence of the cloak was revealed, as the length of average photon paths through the cloak differ compared to the ones through the reference sample. This experiment was supported by numerical calculations of the path length distributions and theoretical derivations of the speckle contrast. Altogether, this is an important finding as it shows that information hidden for the bare eye in light-scattering media can be revealed in a relatively easy and cheap way via finite coherence length. This might have everyday applications like encoded bar-codes in credit cards as a security feature, since the readout is feasible with only a laser pointer and a camera.

As described in Chapter 5, an interferometric setup was built to measure the complex transmitted field under coherent illumination. This yields a complex transmission matrix for a certain design which then allows to also calculate the expected speckle pattern for arbitrary illumination patterns. In principle, this would allow to enhance the transmission through the sample via eigenchannel analysis and a corresponding wavefront shaping. These more complex measurements, however, also set up challenges for the sample preparation as cloak and reference needed to be miniaturized and more stable – this was obtained by a new set of samples out of a clear resin doped with titanium dioxide.

Obtaining a transmission matrix was realized by illuminating the samples from different angles and recording the corresponding complex transmission. Even though each measurement itself with coherent illumination would not reveal the cloak, a sweep over different illumination angles followed by a singular value decomposition of the obtained transmission matrix and comparing the trend of the singular values revealed the cloak in its surrounding. This is no contradiction to the previous experiments where the cloak had not been revealed under coherent illumination, but demonstrates the power of the complex field measurement and the eigenchannel analysis.

Overall, the findings in this thesis demonstrate limitations of cloaking designs in light-scattering media. While with the obtained results I do not see easy steps forward in circumventing these limitations, building on these properties to optimize light guiding or detection of hidden structures in light-scattering media still is a field with a lot of research potential.

Beyond cloaking, it is already evident that a better understanding of light propagation in scattering media has many applications. Diffuse-light mammography, for example, is an active field of research. The findings in this thesis show, that other methods in illumination, detection, or post-processing also reveal hidden objects and could therefore be used in future medical applications. Furthermore, the intense study on laminates in diffuse-light simplifies the design process of future devices that require anisotropic material parameters.

BIBLIOGRAPHY

- [1] J. B. Pendry, D. Schurig, and D. R. Smith, "Controlling Electromagnetic Fields", *Science* **312**, 1780–1782 (2006) (cited on pages 3, 20).
- [2] D. Schurig, J. J. Mock, B. J. Justice, S. A. Cummer, J. B. Pendry, A. F. Starr, and D. R. Smith, "Metamaterial Electromagnetic Cloak at Microwave Frequencies", *Science* **314**, 977–980 (2006) (cited on pages 3, 21, 25, 73).
- [3] V. M. Shalaev, "Transforming Light", *Science* **322**, 384–386 (2008) (cited on pages 3, 25, 73).
- [4] L. H. Gabrielli, J. Cardenas, C. B. Poitras, and M. Lipson, "Silicon nanostructure cloak operating at optical frequencies", *Nature Photonics* **3**, 461–463 (2009) (cited on pages 3, 25, 73).
- [5] M. Wegener and S. Linden, "Shaping optical space with metamaterials", *Physics Today* **63**, 32–36 (2010) (cited on pages 3, 25, 73).
- [6] X. Chen, Y. Luo, J. Zhang, K. Jiang, J. B. Pendry, and S. Zhang, "Macroscopic invisibility cloaking of visible light", *Nature Communications* **2**, 176 (2011) (cited on pages 3, 25, 73).
- [7] N. Landy and D. R. Smith, "A full-parameter unidirectional metamaterial cloak for microwaves", *Nature Materials*, 10.1038/nmat3476 (2012) (cited on pages 3, 25, 73).
- [8] J. Li and J. B. Pendry, "Hiding under the Carpet: A New Strategy for Cloaking", *Physical Review Letters* **101**, 203901 (2008) (cited on pages 3, 25, 73).
- [9] J. Valentine, J. Li, T. Zentgraf, G. Bartal, and X. Zhang, "An optical cloak made of dielectrics", *Nature Materials* **8**, 568–571 (2009) (cited on pages 3, 25, 73).
- [10] T. Ergin, N. Stenger, P. Brenner, J. B. Pendry, and M. Wegener, "Three-Dimensional Invisibility Cloak at Optical Wavelengths", *Science* **328**, 337–339 (2010) (cited on pages 3, 25, 73).
- [11] H. Chen and C. T. Chan, "Acoustic cloaking in three dimensions using acoustic metamaterials", *Applied Physics Letters* **91**, 183518–183518–3 (2007) (cited on pages 3, 25).

- [12] A. N. Norris, "Acoustic cloaking theory", [Proceedings of the Royal Society A: Mathematical, Physical and Engineering Science](#) **464**, 2411–2434 (2008) (cited on pages 3, 25).
- [13] B.-I. Popa, L. Zigoneanu, and S. A. Cummer, "Experimental Acoustic Ground Cloak in Air", [Physical Review Letters](#) **106**, 253901 (2011) (cited on pages 3, 25).
- [14] G. W. Milton, M. Briane, and J. R. Willis, "On cloaking for elasticity and physical equations with a transformation invariant form", [New Journal of Physics](#) **8**, 248 (2006) (cited on pages 3, 25, 49).
- [15] M. Brun, S. Guenneau, and A. B. Movchan, "Achieving control of in-plane elastic waves", [Applied Physics Letters](#) **94**, 061903 (2009) (cited on pages 3, 25).
- [16] M. Farhat, S. Guenneau, and S. Enoch, "Ultrabroadband Elastic Cloaking in Thin Plates", [Physical Review Letters](#) **103**, 024301 (2009) (cited on pages 3, 25).
- [17] N. Stenger, M. Wilhelm, and M. Wegener, "Experiments on Elastic Cloaking in Thin Plates", [Physical Review Letters](#) **108**, 014301 (2012) (cited on pages 3, 25).
- [18] A. V. Amirkhizi, A. Tehranian, and S. Nemat-Nasser, "Stress-wave energy management through material anisotropy", [Wave Motion](#) **47**, 519–536 (2010) (cited on pages 3, 25).
- [19] A. Norris and A. Shuvalov, "Elastic cloaking theory", [Wave Motion](#) **48**, 525–538 (2011) (cited on pages 3, 25).
- [20] W. J. Parnell and T. Shearer, "Antiplane elastic wave cloaking using metamaterials, homogenization and hyperelasticity", [Wave Motion](#) **50**, 1140–1152 (2013) (cited on pages 3, 25).
- [21] F. Yang, Z. L. Mei, T. Y. Jin, and T. J. Cui, "dc Electric Invisibility Cloak", [Physical Review Letters](#) **109**, 053902 (2012) (cited on pages 3, 25, 47).
- [22] W. X. Jiang, C. Y. Luo, Z. L. Mei, and T. J. Cui, "An ultrathin but nearly perfect direct current electric cloak", [Applied Physics Letters](#) **102**, 014102 (2013) (cited on pages 3, 25).
- [23] T. Han, H. Ye, Y. Luo, S. P. Yeo, J. Teng, S. Zhang, and C.-W. Qiu, "Manipulating DC Currents with Bilayer Bulk Natural Materials", [Advanced Materials](#) **26**, 3478–3483 (2014) (cited on pages 3, 25).
- [24] F. Gömöry, M. Solovyov, J. Šouc, C. Navau, J. Prat-Camps, and A. Sanchez, "Experimental Realization of a Magnetic Cloak", [Science](#) **335**, 1466–1468 (2012) (cited on pages 3, 25).

-
- [25] M. Solovyov, J. Šouc, and F. Gömöry, “Magnetic Cloak for Low Frequency AC Magnetic Field”, *IEEE Transactions on Applied Superconductivity* **25**, 1–5 (2015) (cited on pages 3, 25).
- [26] J. Prat-Camps, C. Navau, and A. Sanchez, “A Magnetic Wormhole”, *Scientific Reports* **5**, 12488 (2015) (cited on pages 3, 25, 48).
- [27] S. Guenneau, C. Amra, and D. Veynante, “Transformation thermodynamics: cloaking and concentrating heat flux”, *Optics Express* **20**, 8207–8218 (2012) (cited on page 4).
- [28] R. Schittny, M. Kadic, S. Guenneau, and M. Wegener, “Experiments on Transformation Thermodynamics: Molding the Flow of Heat”, *Physical Review Letters* **110**, 195901 (2013) (cited on pages 4, 21, 47).
- [29] Z. Chang, X. Liu, and G. Hu, “Heat flow control by transformation method with grid generation method”, *Acta Mechanica Solida Sinica* **27**, 454–460 (2014) (cited on pages 4, 47).
- [30] R. Schittny, M. Kadic, T. Bückmann, and M. Wegener, “Invisibility cloaking in a diffusive light scattering medium”, *Science* **345**, 427–429 (2014) (cited on pages 4, 48, 74).
- [31] D. R. Leff, O. J. Warren, L. C. Enfield, A. Gibson, T. Athanasiou, D. K. Patten, J. Hebden, G. Z. Yang, and A. Darzi, “Diffuse optical imaging of the healthy and diseased breast: A systematic review”, *Breast Cancer Research and Treatment* **108**, 9–22 (2008) (cited on page 4).
- [32] D. A. Boas, D. H. Brooks, E. L. Miller, C. A. DiMarzio, M. Kilmer, R. J. Gaudette, and Quan Zhang, “Imaging the body with diffuse optical tomography”, *IEEE Signal Processing Magazine* **18**, 57–75 (2001) (cited on pages 4, 80).
- [33] T. Durduran, R. Choe, W. B. Baker, and A. G. Yodh, “Diffuse optics for tissue monitoring and tomography”, *Reports on Progress in Physics* **73**, 076701 (2010) (cited on page 4).
- [34] H. Hashemi, B. Zhang, J. D. Joannopoulos, and S. G. Johnson, “Delay-Bandwidth and Delay-Loss Limitations for Cloaking of Large Objects”, *Physical Review Letters* **104**, 253903 (2010) (cited on pages 4, 21).
- [35] E. H. Kerner, “The Electrical Conductivity of Composite Media”, *Proceedings of the Physical Society. Section B* **69**, 802 (1956) (cited on pages 4, 20, 21).
- [36] E. H. Kerner, “The Elastic and Thermo-elastic Properties of Composite Media”, *Proceedings of the Physical Society. Section B* **69**, 808 (1956) (cited on pages 4, 20, 21).

- [37] Z. Hashin and S. Shtrikman, “A variational approach to the theory of the elastic behaviour of multiphase materials”, *Journal of the Mechanics and Physics of Solids* **11**, 127–140 (1963) (cited on pages 4, 22).
- [38] A. Alù and N. Engheta, “Achieving transparency with plasmonic and meta-material coatings”, *Physical Review E* **72**, 016623 (2005) (cited on page 4).
- [39] R. Schittny, A. Niemeyer, M. Kadic, T. Bückmann, A. Naber, and M. Wegener, “Transient behavior of invisibility cloaks for diffusive light propagation”, *Optica* **2**, 84–87 (2015) (cited on pages 4, 21, 26, 48, 79, 109).
- [40] F. Mayer, R. Schittny, A. Egel, A. Niemeyer, J. Preinfalk, U. Lemmer, and M. Wegener, “Cloaking Contacts on Large-Area Organic Light-Emitting Diodes”, *Advanced Optical Materials* **4**, 740–745 (2016) (cited on pages 5, 27, 29, 47, 48, 73).
- [41] R. J. Schittny, “Cloaking in Heat Conduction and Light Diffusion”, PhD thesis (Karlsruhe Institute of Technology (KIT), Karlsruhe, 2015) (cited on pages 7, 91).
- [42] S. Mannherz, *On the Limits of Laminates in Diffuse Light Cloaking*, Unpublished Master’s Thesis, 2018 (cited on pages 7, 19, 47, 60, 61, 70).
- [43] F. Scheffold, R. Lenke, R. Tweert, and G. Maret, “Localization or classical diffusion of light?”, *Nature* **398**, 206–207 (1999) (cited on page 8).
- [44] C. M. Soukoulis, *Photonic Crystals and Light Localization in the 21st Century* (Springer Science & Business Media, May 31, 2001), 632 pp. (cited on page 8).
- [45] D. S. Wiersma, P. Bartolini, A. Lagendijk, and R. Righini, “Localization of light in a disordered medium”, *Nature* **390**, 671–673 (1997) (cited on page 8).
- [46] F. Martelli, S. D. Bianco, A. Ismaelli, and G. Zaccanti, *Light Propagation Through Biological Tissue and Other Diffusive Media: Theory, Solutions, and Software*, Auflage: Pap/Cdr (SPIE Press, Bellingham, Wash, Jan. 15, 2010), 274 pp. (cited on pages 8, 9, 15, 52, 91).
- [47] L. C. Henyey and J. L. Greenstein, “Diffuse radiation in the galaxy”, *Astrophysical Journal* **93**, 70–83 (1941) (cited on page 9).
- [48] G. Mie, “Beiträge zur Optik trüber Medien, speziell kolloidaler Metallösungen”, *Annalen der Physik* **330**, 377–445 (1908) (cited on pages 9, 10).
- [49] G. Zaccanti, E. Battistelli, P. Brusaglioni, and Q. Wei, “Analytic relationships for the statistical moments of scattering point coordinates for photon migration in a scattering medium”, *Pure and Applied Optics: Journal of the European Optical Society Part A* **3**, 897–905 (1994) (cited on page 10).
- [50] E. Hecht, *Optics* (Pearson Education, 2016) (cited on pages 10, 35).

-
- [51] A. Ishimaru, *Wave propagation and scattering in random media*, Vol. 2 (Academic press New York, 1978) (cited on page 10).
- [52] T. Durduran, A. G. Yodh, B. Chance, and D. A. Boas, “Does the photon-diffusion coefficient depend on absorption?”, *JOSA A* **14**, 3358–3365 (1997) (cited on page 14).
- [53] A. Fick, “Ueber Diffusion”, *Annalen der Physik* **170**, 59–86 (1855) (cited on pages 15, 49).
- [54] T. K. M. Wong, “Method of heat lamination and laminated product”, U.S. pat. 4167431A (M. A. Co, Sept. 11, 1979) (cited on page 18).
- [55] T. Sinmazçelik, E. Avcu, M. Ö. Bora, and O. Çoban, “A review: Fibre metal laminates, background, bonding types and applied test methods”, *Materials & Design* **32**, 3671–3685 (2011) (cited on page 18).
- [56] G. W. Milton, *The Theory of Composites* (Cambridge University Press, Cambridge, 2002) (cited on pages 18, 22).
- [57] R. Schittny, A. Niemeyer, F. Mayer, A. Naber, M. Kadic, and M. Wegener, “Invisibility cloaking in light-scattering media”, *Laser & Photonics Reviews* **10**, 382–408 (2016) (cited on pages 18, 74).
- [58] U. Leonhardt, “Optical Conformal Mapping”, *Science* **312**, 1777–1780 (2006) (cited on page 20).
- [59] M. Kadic, T. Bückmann, R. Schittny, and M. Wegener, “Experiments on cloaking in optics, thermodynamics and mechanics”, *Philosophical Transactions of the Royal Society A: Mathematical, Physical and Engineering Sciences* **373**, 20140357 (2015) (cited on page 21).
- [60] B. Orazbayev, M. Beruete, A. Martínez, and C. García-Meca, “Diffusive-light invisibility cloak for transient illumination”, *Physical Review A* **94**, 063850 (2016) (cited on pages 26, 48).
- [61] Q. Fang and D. R. Kaeli, “Accelerating mesh-based Monte Carlo method on modern CPU architectures”, *Biomedical Optics Express* **3**, 3223–3230 (2012) (cited on page 29).
- [62] M. Dekking, *A modern introduction to probability and statistics : understanding why and how*, in collab. with Library Genesis (London : Springer, 2005), 485 pp. (cited on page 30).
- [63] I. N. Bronshtein and K. A. Semendyayev, *Handbook of Mathematics* (Springer Science & Business Media, June 29, 2013), 989 pp. (cited on page 30).
- [64] A. Klenke, *Grundlagen der Maßtheorie*, edited by A. Klenke, Springer-Lehrbuch Masterclass (Springer, Berlin, Heidelberg, 2013), 48 pp. (cited on page 30).

- [65] L. N. Bol'shev, "On Estimates of probabilities", [Theory of Probability & Its Applications](#) **5**, 411–415 (1960) (cited on page 31).
- [66] V. S. Pugachev, *Probability Theory and Mathematical Statistics for Engineers* (Elsevier, June 28, 2014), 469 pp. (cited on page 31).
- [67] S. So, "Why is the sample variance a biased estimator?", Griffith University, Tech. Rep. **9** (2008) (cited on page 31).
- [68] R. K. Burdick, *Confidence intervals on variance components*, 04; QA276. 74, B8. (1992) (cited on page 33).
- [69] S. Foss, D. Korshunov, and S. Zachary, *An introduction to heavy-tailed and subexponential distributions*, Vol. 6 (Springer, 2011) (cited on page 33).
- [70] J. W. Goodman, *Speckle Phenomena in Optics: Theory and Applications* (Roberts and Company Publishers, 2007), 426 pp. (cited on page 35).
- [71] G. Parry, "Some Effects of Temporal Coherence on the First Order Statistics of Speckle", [Optica Acta: International Journal of Optics](#) **21**, 763–772 (1974) (cited on page 36).
- [72] C. A. Thompson, K. J. Webb, and A. M. Weiner, "Diffusive media characterization with laser speckle", [Applied Optics](#) **36**, 3726–3734 (1997) (cited on pages 36, 80).
- [73] C. A. Thompson, K. J. Webb, and A. M. Weiner, "Imaging in scattering media by use of laser speckle", [JOSA A](#) **14**, 2269–2277 (1997) (cited on pages 36, 80).
- [74] M. Born and E. Wolf, *Principles of Optics: Electromagnetic Theory of Propagation, Interference and Diffraction of Light* (Elsevier, June 1, 2013), 871 pp. (cited on page 37).
- [75] I. Reed, "On a moment theorem for complex Gaussian processes", [IRE Transactions on Information Theory](#) **8**, 194–195 (1962) (cited on page 38).
- [76] E. Sánchez-Ortiga, A. Doblás, G. Saavedra, M. Martínez-Corral, and J. Garcia-Sucerquia, "Off-axis digital holographic microscopy: practical design parameters for operating at diffraction limit", [Applied Optics](#) **53**, 2058–2066 (2014) (cited on page 41).
- [77] S. Mannherz, A. Niemeyer, F. Mayer, C. Kern, and M. Wegener, "On the limits of laminates in diffusive optics", [Optics Express](#) **26**, 34274–34287 (2018) (cited on pages 47, 49, 55, 56, 63, 65, 67, 69).
- [78] K. P. Vemuri and P. R. Bandaru, "Anomalous refraction of heat flux in thermal metamaterials", [Applied Physics Letters](#) **104**, 083901 (2014) (cited on page 48).
- [79] C. Navau, J. Prat-Camps, O. Romero-Isart, J. I. Cirac, and A. Sanchez, "Long-Distance Transfer and Routing of Static Magnetic Fields", [Physical Review Letters](#) **112**, 253901 (2014) (cited on page 48).

-
- [80] M. F. Schumann, M. Langenhorst, M. Smeets, K. Ding, U. W. Paetzold, and M. Wegener, "All-Angle Invisibility Cloaking of Contact Fingers on Solar Cells by Refractive Free-Form Surfaces", *Advanced Optical Materials* **5**, 1700164 (2017) (cited on page 73).
- [81] R. Schittny, A. Niemeyer, M. Kadic, T. Bückmann, A. Naber, and M. Wegener, "Diffuse-light all-solid-state invisibility cloak", *Optics Letters* **40**, 4202–4205 (2015) (cited on pages 73, 74, 88, 91, 92, 110).
- [82] A. Niemeyer, F. Mayer, A. Naber, M. Koirala, A. Yamilov, and M. Wegener, "Uncloaking diffusive-light invisibility cloaks by speckle analysis", *Optics Letters* **42**, 1998–2001 (2017) (cited on pages 74–77, 81–83, 85).
- [83] M. Koirala and A. Yamilov, "Detection of a diffusive cloak via second-order statistics", *Optics Letters* **41**, 3860–3863 (2016) (cited on page 78).
- [84] J. D. McKinney, M. A. Webster, K. J. Webb, and A. M. Weiner, "Characterization and imaging in optically scattering media by use of laser speckle and a variable-coherence source", *Optics Letters* **25**, 4–6 (2000) (cited on page 80).
- [85] N. Curry, P. Bondareff, M. Leclercq, N. F. v. Hulst, R. Sapienza, S. Gigan, and S. Grésillon, "Direct determination of diffusion properties of random media from speckle contrast", *Optics Letters* **36**, 3332–3334 (2011) (cited on page 80).
- [86] A. Dogariu and R. Carminati, "Electromagnetic field correlations in three-dimensional speckles", *Physics Reports, Electromagnetic field correlations in three-dimensional speckles* **559**, 1–29 (2015) (cited on page 80).
- [87] S. M. Popoff, G. Lerosey, R. Carminati, M. Fink, A. C. Boccara, and S. Gigan, "Measuring the Transmission Matrix in Optics: An Approach to the Study and Control of Light Propagation in Disordered Media", *Physical Review Letters* **104**, 100601 (2010) (cited on pages 87, 88, 96).
- [88] S. M. Popoff, G. Lerosey, M. Fink, A. C. Boccara, and S. Gigan, "Controlling light through optical disordered media: transmission matrix approach", *New Journal of Physics* **13**, 123021 (2011) (cited on page 87).
- [89] H. Yu, T. R. Hillman, W. Choi, J. O. Lee, M. S. Feld, R. R. Dasari, and Y. Park, "Measuring Large Optical Transmission Matrices of Disordered Media", *Physical Review Letters* **111**, 153902 (2013) (cited on pages 87, 88).
- [90] I. M. Vellekoop and A. P. Mosk, "Focusing coherent light through opaque strongly scattering media", *Optics Letters* **32**, 2309–2311 (2007) (cited on page 87).
- [91] W. Choi, A. P. Mosk, Q.-H. Park, and W. Choi, "Transmission eigenchannels in a disordered medium", *Physical Review B* **83**, 134207 (2011) (cited on page 87).

- [92] M. Kim, W. Choi, Y. Choi, C. Yoon, and W. Choi, "Transmission matrix of a scattering medium and its applications in biophotonics", *Optics Express* **23**, Publisher: Optical Society of America, 12648–12668 (2015) (cited on page 88).
- [93] M. Kim, Y. Choi, C. Yoon, W. Choi, J. Kim, Q.-H. Park, and W. Choi, "Maximal energy transport through disordered media with the implementation of transmission eigenchannels", *Nature Photonics* **6**, 581–585 (2012) (cited on pages 88, 103).
- [94] K. Baker, "Singular value decomposition tutorial", The Ohio State University **24** (2005) (cited on page 101).
- [95] G. W. Stewart, "On the Early History of the Singular Value Decomposition", *SIAM Review* **35**, 551–566 (1993) (cited on page 101).
- [96] J. Xu, H. Ruan, Y. Liu, H. Zhou, and C. Yang, "Focusing light through scattering media by transmission matrix inversion", *Optics Express* **25**, 27234–27246 (2017) (cited on page 103).
- [97] A. P. Mosk, A. Lagendijk, G. Lerosey, and M. Fink, "Controlling waves in space and time for imaging and focusing in complex media", *Nature Photonics* **6**, 283–292 (2012) (cited on page 103).
- [98] A. G. Yamilov, R. Sarma, V. V. Yakovlev, and H. Cao, "Coherent injection of light into an absorbing scattering medium with a microscopic pore", *Optics Letters* **43**, 2189–2192 (2018) (cited on page 109).
- [99] A. M. S. Macêdo and J. T. Chalker, "Exact results for the level density and two-point correlation function of the transmission-matrix eigenvalues in quasi-one-dimensional conductors", *Physical Review B* **49**, 4695–4702 (1994) (cited on page 109).

ACKNOWLEDGMENTS

At this point, I would like to express my gratitude to everyone who supported and motivated me during this thesis.

First, I want to thank my advisor, Prof. Dr. Martin Wegener, who gave me the opportunity to work on the versatile topic of diffusive light propagation and who provided an ideal experimental infrastructure. His professional advice during our fruitful discussions and his commitment supporting me in hard times was crucial for the success of this thesis. Likewise, I would like to express my gratitude to Prof. Dr. Carsten Rockstuhl, who kindly agreed to co-referee this thesis.

Within the first project of my PhD, I had the pleasure to collaborate with Prof. Dr. Alexey Yamilov and Dr. Milan Koirala from Missouri University of Science and Technology. I am happy to have the opportunity to thank them for this here.

The project on transmission eigenchannels would not have been a success without my stay at Korea University, the help of Prof. Dr. Wonshik Choi and all the group members of his research group. I am very grateful for the insights I learned and the warm welcome I got in Korea.

Within the last years, through all ups and downs, the vivid research group I belonged to was not only a group that made working a pleasant experience but also supported me with huge expertise in many fields of physics.

A special thanks goes to the colleagues I worked closely with. Robert Schittny who not only supervised my master's thesis but also paved the way for this thesis by his work on core-shell cloaks was a big help in my first years. Furthermore, I want to thank Frederik Mayer who was my go-to discussion partner when it came to fundamental thoughts about scattering light, Sabine Mannherz for our joint work on laminates which led to a much deeper understanding of light diffusion and Vincent Hahn who helped me a lot with the interferometric setup within the last year.

I also want to thank all the critical proof readers of this thesis namely Tobias Frenzel, Marc Hippler, Frederik Mayer, Tobias Messer, and Andreas Wickberg who improved this thesis by their comments a lot.

We scientists could never perform our work were it not for all the people who provide us with technical and administrative assistance. In this sense I want to thank our technician Johann Westhauser, the secretariat namely Claudia Alaya, Petra Bauer, Monika Brenkmann, and Ursula Mösle, the electronics workshop consisting of Werner Gilde, Michael Hippe, and Helmuth Lay, and the whole mechanical workshop headed by Frank Landhäußer.

ACKNOWLEDGMENTS

Finally, I want to express my gratitude to my girlfriend Bianca and my family for their incessant support during my PhD especially within the last months.

